IS-T-1784

Optically Detected Magnetic Resonance Studies on {pi}-conjugate Polymers and Novel Carbon Allotropes

by

Partee, Jonathan

PHD Thesis submitted to Iowa State University

Ames Laboratory, U.S. DOE
Iowa State University
Ames, Iowa 50011

Date Transmitted: February 12, 1999

PREPARED FOR THE U.S. DEPARTMENT OF ENERGY
UNDER CONTRACT NO. W-7405-Eng-82.

DISCLAIMER

DISCLAIMER

DISCLAIMER

Portions of this document may be illegible in electronic image products. Images are produced from the best available original document.

Dedicated to

Sara, Charles, and Margaret

"I have fought the good fight, I have finished the race, I have kept the faith."

2 Timothy 4:7

TABLE OF CONTENTS

ACKNOWLEDGEMENTS

I am deeply indebted to the College of Wooster Department of Physics faculty, especially Dr. Donald Jacobs, for their support and guidance early in my physics career. I am also grateful to Dr. Jack Fanselow, Jean Patterson, Dr. Thomas Cwik and Diglio Simoni at the Jet Propulsion Laboratory in Pasadena for their parts in one of the most important experiences I've had thus far.

My thanks also to my peers at Iowa State University: Mike Debye, Thomas Pe and the rest of the entering class of 1991. I never would have made it through the first two years without them. In addition, the members of Dr. Shinar's research group who had a great deal of influence on me: Leland Swanson, Paul Lane, Andy Smith, Ornit Amir, and Tea Cerkvenik. A special thanks to Dr. Wilhelm Graupner for the large amount of work he did on the data presented in Chapter 3.

Most importantly, though, my everlasting gratitude to Dr. Joseph Shinar who provided the right mix of support and *laissez faire*. Without his support, this degree would not have been possible.

I would like to thank my parents and my brother for much encouragement and support through the long years of graduate school.

A special thanks to the former Miss Sara Lyn Gunderson, now Mrs. Sara Lyn Partee, for filling my days with much love and joy.

This work was performed at Ames Laboratory under Contract No. W-7405-Eng-82 with the U.S. Department of Energy. The United States government has assigned the DOE Report number IS-T 1784 to this thesis.

CHAPTER 1. INTRODUCTION TO PHOTOLUMINESCENCE DETECTED MAGNETIC RESONANCE (PLDMR)

The origins of the Photoluminescence Detected Magnetic Resonance (PLDMR) measurements lie in the primitive microwave spectrometer constructed in 1934 by Cleeton and William and used on an ammonia molecule.[1] Because of the limitations of the technology, very little progress in this area occured for almost a decade. The technological demands of World War II, however, led to a bonanza of developments in a number of areas important to magnetic resonance research including: introduction of magnetrons, the development of crystal detectors, and the advent of lock-in detection and other noise-reducing circuitry.[1] While these developments were primarily motivated by the wartime effort, they advanced microwave and electronic technology to the point where electron spin resonance (ESR) and microwave spectroscopes could be constructed with the required sensitivity.

1.1 Description of PLDMR

Photoluminescence (PL) Detected Magnetic Resonance (PLDMR), a logical extension of ESR, was introduced in 1967-68 by M. Sharnoff working on napthalene.[2] In the typical PLDMR experiment one monitors the PL of a sample placed in a microwave cavity located in a magnetic field. When the magnet scans through resonance, a microwave-induced change in the PL is observed. These experiments can be undertaken to investigate spin-½ species as well as spin-1 species.

Magnetic resonance (MR) experiments investigate paramagnetic excited states with a sensitivity of 1 part in 10^6. The dynamics of the spin-carrying species are first investigated, then that knowledge is extended to piece together a description of the dynamics in the material. Some of the specific information that can be gained by MR experiments are: g-value, lifetime, types of recombination pathways and spin Hamiltonian parameters of the excited electronic state.

1.2 Spin-½ Resonances

The bulk excitation in inorganic and small organic molecular semiconductors is a bound electron-hole pair, called an exciton, which is responsible for the PL. Excitons can exist in singlet (spin S=0) or in triplet states (S=1) and may be loosely bound (Mott-Wannier) or tightly bound (Frenkel).[3] The Mott-Wannier exciton (Figure 1.1 (a)) is usually free to move through the crystal and maintains an electron-hole distance which is large compared to the lattice constant. A Frenkel exciton (Figure 1.1 (b)) is localized on one atom in a crystal.[3] Frenkel excitons have a lifetime of ~8μs.

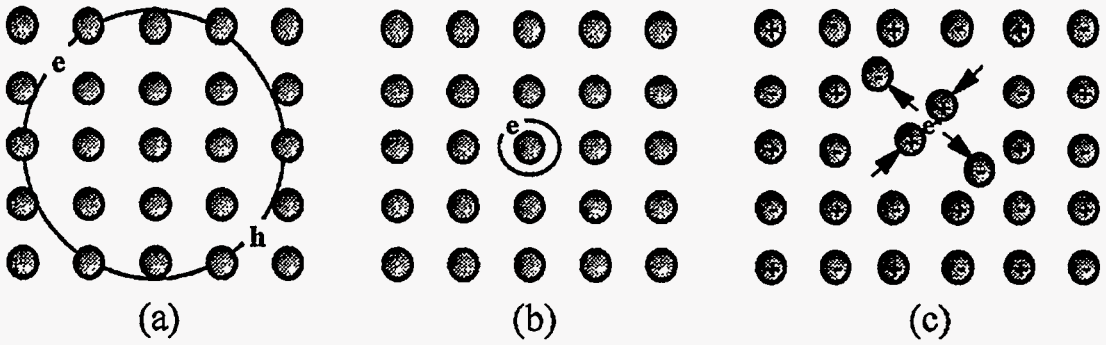

Figure 1.1 Molecular view of (a) a Mott-Wannier exciton, (b) a Frenkel exciton, and (c) a negative polaron.

A polaron is an electron (or a hole) "dressed" with the associated strain field (Figure 1.1(c)). This electron-phonon interaction lowers the electron's energy and produces a state in the gap. Many researchers have described the polaron as an excitonic quenching center, meaning that the polarons open a fast nonradiative decay channel for the excitons.[4]

For a particle with non-zero spin placed in a magnetic field, the interaction can be described by the well-known spin Hamiltonian:

$$H = \vec{S} \bullet \overleftrightarrow{g} \beta \bullet \vec{H} \qquad (1.1)$$

where:

$\overrightarrow{S}$ is the spin of the particle

$\overleftrightarrow{g}$ is a tensor describing the interaction of the particle with the field

$\overrightarrow{H}$ is the applied magnetic field

β is the Bohr magneton

When g is isotropic[5] the equation is simplified to:

$$H = g\beta \overrightarrow{S} \bullet \overrightarrow{H} \tag{1.2}$$

A weakly interacting system like a Mott-Wannier exciton or a polaron pair will have a negligible spin-spin coupling energy, so the Zeeman splitting will dominate. Since each spin-½ can align itself with or against the magnetic field, four energy levels are possible (Figure 1.2). These energy levels are:

$$E = \frac{1}{2}(\pm g_e \pm g_h)\beta H_o \tag{1.3}$$

where:

g_e and g_h are the electron and hole g values, respectively

H_o is the magnitude of the applied magnetic field

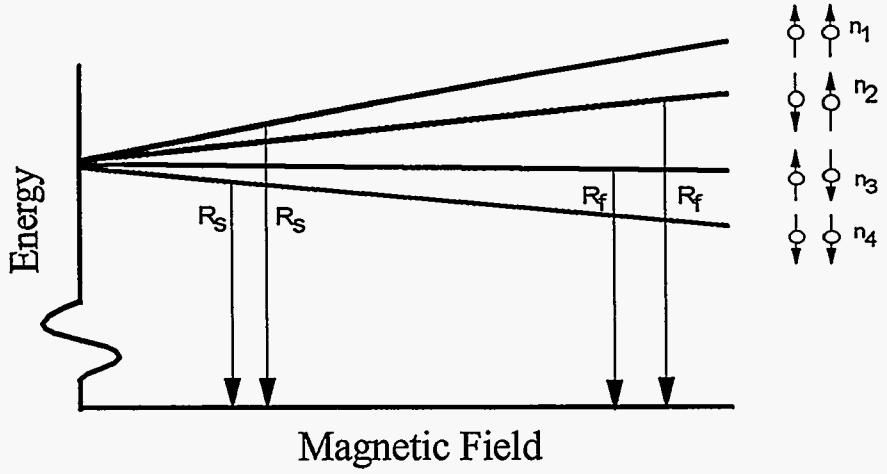

Figure 1.2 Energy levels for weakly bound electron-hole pairs in a magnetic field. R_F and R_S correspond to the fast and slow recombination pathways, respectively.

Classically, antiparallel electron-hole states can radiatively decay to the ground state whereas parallel states cannot. Therefore, the populations n_2 and n_3 (Figure 1.2) will be rapidly depleted relative to n_1 and n_4. If microwave photons, with the appropriate energy, are incident on the sample, the spin populations are mixed. For example, if the polaron pairs quench singlet excitons nonradiatively, then the build-up of parallel spin polaron pairs off resonance will be reduced at resonance, removing polarons from the system. Then the nonradiative quenching of the excitons is weakened, resulting in a PL-enhancing signal. Alternatively, an enhancing resonance may be observed if the resonance conditions lead to a repopulation of the ground state. The repopulated ground state leads to greater absorption and consequently a higher population in the excited states. This is the so-called "ground state recovery" mechanism.[4] These mechanisms, among others described later, can lead to a spin-½ PLDMR spectrum similar to Figure 1.3. In most cases, the observed lineshape can be fit to two Gaussians,[6] although a single Lorenzian has been used in some systems.[7] In π-conjugated polymers these spin-½ resonances are believed to be due to the recombination of polaron pairs.

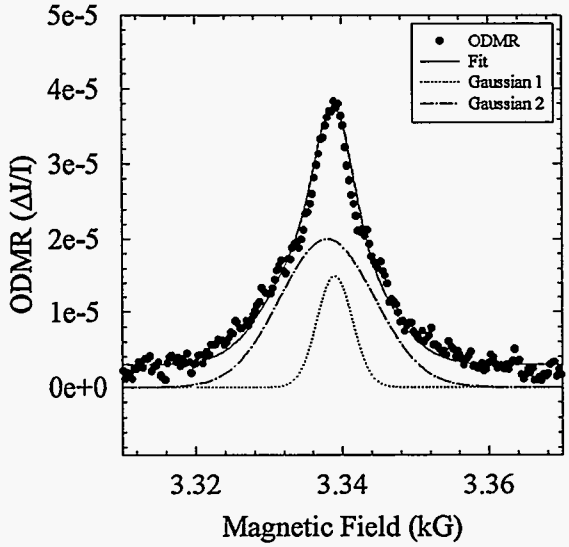

Figure 1.3 Typical spin-½ enhancing PLDMR spectra. This particular spectum comes from poly(*p*-phenylene)-type ladder (LPPP) polymers (described below).

Note that the PL increases in response to the application of microwaves. Thus, this is called an "enhancing resonance". It is also possible to see a "quenching resonance" where the PL decreases at the resonant field in response to the microwaves. This situation might occur if a population of geminate electron-hole pairs are prevented from recombining due to microwave-induced spin-flips.

1.3 Spin-1 Resonances

The triplet state is probably among the most prolific of excited states in π-conjugated polymers. However, it is also poorly understood. PLDMR can serve as a tool to investigate triplets which live anywhere from ~ 10μs up to 10ms. Triplets whose lifetimes are outside of this range cannot be detected by the apparatus. Comprehensive treatment of triplet detection can be found in references 1,5,8 and 9, but a brief overview follows below.

In the molecular picture, the triplet state is an exited state of the molecule with spin S=1. Alternatively, it can be viewed as a spin-parallel electron-hole pair on the same molecule. The spin Hamiltonian for a pair of interacting, spin-½ particles in a magnetic field is:

$$H=H_Z+H_{S\text{-}S}+H_{hfs} \tag{1.4}$$

where:

H_Z is the paramagnetic Zeeman interaction of the spins in a magnetic field

$H_{S\text{-}S}$ is the spin-spin dipole interaction

H_{hfs} is the hyperfine interaction between the electronic and nuclear dipole moments

The hyperfine structure term is neglected in this study for two reasons: (i) the samples are disordered and the rapid diffusion of excitons implies that all hyperfine environments are rapidly sampled[10] and (ii) the primary contribution of the H_{hfs} term leads to a slight broadening of already large (>200G) triplet resonances.

The dipole interaction for an ensemble of magnetic moments is:[11]

$$H_{D-D} = \sum_{i \neq j} \frac{\mu_i \bullet \mu_j}{r_{ij}^3} - 3\frac{(\vec{r_{ij}} \bullet \vec{\mu_i})(\vec{r_{ij}} \bullet \vec{\mu_j})}{r_{ij}^5} \tag{1.5}$$

where:

$\vec{r_{ij}}$ is the displacement vector between any pair (i,j) of magnetic moments
$\vec{\mu_i}$ is the magnetic moment

Since the magnetic moment of a particle is $\vec{\mu_i} = g\beta\vec{S_i}$ (where $\vec{S_i}$ is the spin vector of the i-th particle) the spin-spin Hamiltonian can be written:

$$H_{S_1-S_2} = (g\beta)^2\left[\frac{\vec{S_1} \bullet \vec{S_2}}{r^3} - 3\frac{\left(\vec{r} \bullet \vec{S_1}\right)\left(\vec{r} \bullet \vec{S_2}\right)}{r^5}\right] \tag{1.6}$$

This can be expanded in terms of the components of $\vec{S}$:

$$H_{S_1-S_2} = \frac{(g\beta)^2}{r^5}\left[\begin{array}{l}(r^2-3x^2)S_x^2 + (r^2-3y^2)S_y^2 + (r^2-3z^2)S_z^2 \\ \quad -3xy(S_xS_y + S_yS_x) - 3xy(S_yS_z + S_zS_y) - 3zx(S_zS_x + S_xS_z)\end{array}\right] \tag{1.7}$$

Equation 1.7 is conveniently written in matrix notation as:

$$H = \vec{S} \bullet \overleftrightarrow{D} \bullet \vec{S} \qquad \text{where } \overleftrightarrow{D} = \frac{(g\beta)^2}{2r^5}\begin{bmatrix} r^2-3x^2 & -3xy & -3zx \\ -3xy & r^2-3y^2 & -3yz \\ -3zx & -3yz & r^2-3z^2 \end{bmatrix} \tag{1.8}$$

or $\overleftrightarrow{D}$ can be written more elegantly (where $x,y,z = \mu\nu$):

$$D_{\nu\mu} = \frac{(g\beta)^2}{2}\left\langle\frac{r^2\delta_{\mu\nu} - 3r_\mu r_\nu}{r^5}\right\rangle \tag{1.9}$$

with the angular brackets indicating the average over the spatial part of the wavefunction. $\overleftrightarrow{D}$ is the spin-spin coupling tensor which can be diagonalized.[5] The diagonalized basis in a

new coordinate system (x',y',z') determines the principal axes of the triplet. In this system, the Hamiltonian reduces to:

$$H_{S_1-S_2} = -\frac{(g\beta)^2}{2}\left[\left\langle\frac{r^2-3x'^2}{r^5}\right\rangle S_X^2 + \left\langle\frac{r^2-3y'^2}{r^5}\right\rangle S_Y^2 + \left\langle\frac{r^2-3z'^2}{r^5}\right\rangle S_Z^2\right] \tag{1.10}$$

by a judicious choice of X, Y and Z (following the common notation):

$$H_{S_1-S_2} = -XS_X^2 - YS_Y^2 - ZS_Z^2 \tag{1.11}$$

Since $X+Y+Z = 0$ ($\overleftrightarrow{D}$ is traceless) the triplet can be characterized by only two independent parameters. We choose the letters D (not to be confused with $\overleftrightarrow{D}$ the spin-spin coupling tensor) and E to designate these two parameters. Then (S=1):

$$H_{S_1-S_2} = D[S_Z^2 - \tfrac{1}{3}S(S+1)] + E(S_X^2 - S_Y^2) = D(S_Z^2 - \tfrac{2}{3}) + E(S_X^2 + S_Y^2) \tag{1.12}$$

where:

$$D = -\frac{3Z}{2} = \frac{3}{4}(g\beta)^2\left\langle\frac{r^2-3z'^2}{r^5}\right\rangle \tag{1.13}$$

$$E = \frac{Y-X}{2} = -\frac{3}{4}(g\beta)^2\left\langle\frac{x'^2-y'^2}{r^5}\right\rangle \tag{1.14}$$

These parameters, D and E, are called the zero-field splitting (zfs) parameters and have units of energy. Each zero-field energy level is associated with a principal axis, defined as the Z axis, (Equation 1.11) chosen such that $D \geq 3E$. Therefore, the Z axis is the axis split the furthest from the other two. The splitting of the two remaining triplet sublevels equals 2E. The zero-field splitting energy levels of this triplet exciton are shown in Figure 1.4.

When E=0, two levels are degenerate (X=Y), and the triplet is said to be axially symmetric. Indeed, E is used as a measure of the departure from axial symmetry of the triplet. Following the above convention, an upper bound for the spacial extent can be calculated from D (shown below). D, then, is often referred to as a measure of the spatial extent of the exciton.

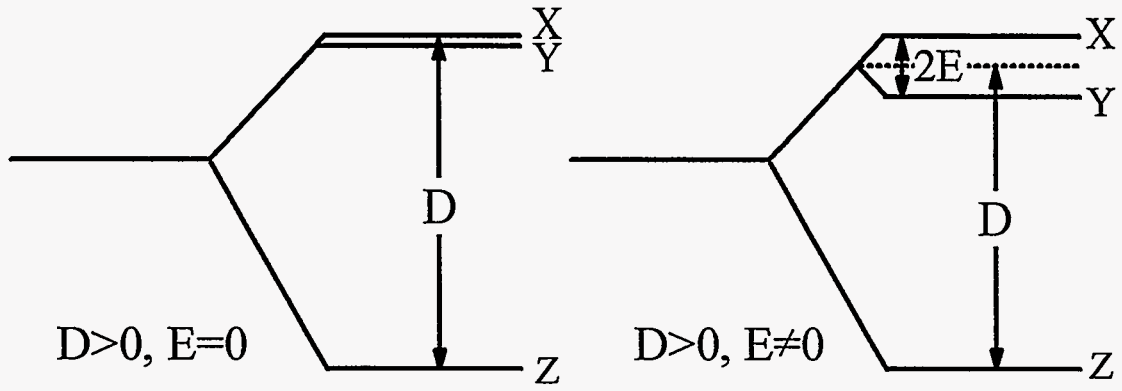

Figure 1.4 Splitting of energy levels in the absence of an external magnetic field.

The full Hamiltonian, with the Zeeman and spin-spin terms, becomes:

$$H = g\beta\vec{H} \bullet \vec{S} - (XS_X^2 + YS_Y^2 + ZS_Z^2) \tag{1.15}$$

The magnetic field $\vec{H}$ has direction cosines (l,m,n) in the molecular axis system. Therefore, in the basis of the functions which diagonalize Equation 1.15, the matrix is:

$$\begin{array}{cccc} & |X\rangle & |Y\rangle & |Z\rangle \\ \langle X| & X & -ig\beta H_n & ig\beta H_m \\ \langle Y| & ig\beta H_n & Y & -ig\beta H_l \\ \langle Z| & -ig\beta H_m & ig\beta H_l & Z \end{array} \tag{1.16}$$

The general solutions are very complicated functions of (l,m,n) so, following Atherton,[5] we consider the special case where the magnetic field is in the z'-direction, $(l,m,n)=(0,0,1)$. The first eigenfunction is $|Z\rangle$ with the eigenvalue of Z. This implies that there will be an energy level unaffected by the magnetic field. The other eigenfunctions are obtained by solution of the remaining quadratic:

$$E_+ = \tfrac{1}{2}(X+Y) + \left\{\left[\tfrac{1}{2}(X-Y)^2\right] + (g\beta H)^2\right\}^{\frac{1}{2}} \tag{1.17}$$

$$E_- = \tfrac{1}{2}(X+Y) - \left\{\left[\tfrac{1}{2}(X-Y)^2\right] + (g\beta H)^2\right\}^{\frac{1}{2}} \tag{1.18}$$

$$E_0 = Z \tag{1.19}$$

A rough plot of the energy vs. magnetic field strength is shown in Figure 1.5. Note that the X and Y levels are mixed and become the $|+1\rangle$ and $|-1\rangle$ energy levels when the magnetic field is directed along z'.

The A and B transitions in Figure 1.5 are full-field transitions while C is the half-field transition. The location of the resonance will depend on the orientation of the crystal with respect to the applied magnetic field. For single crystals, the zero-field splitting parameters can be determined by measuring the positions of the resonances at different orientations of the crystal relative to the magnetic field.

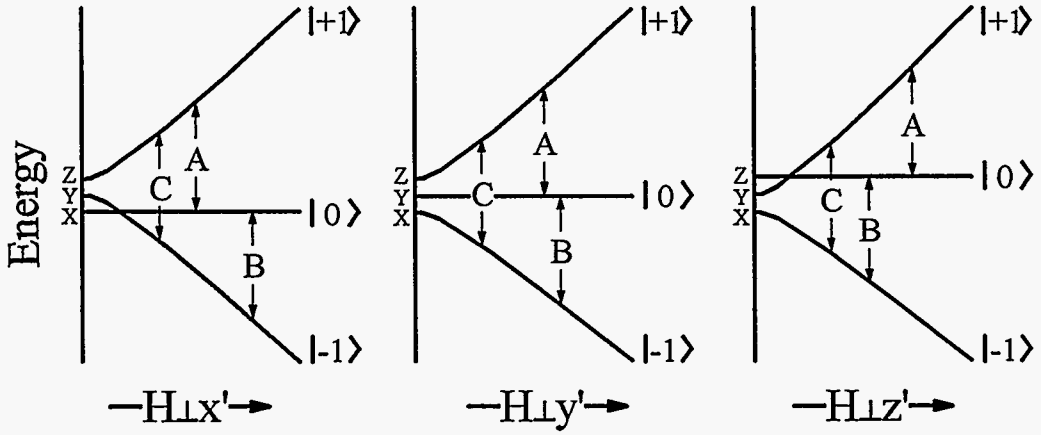

Figure 1.5 Splitting of energy levels for magnetic field **H** aligned with each of the three principal axis.

The resonance spectra in Figure 1.6 shows the PLDMR of naphthalene in a single crystal of durene.[12] Crystalline samples with equivalent sites would only show two full-field transitions (A and B transitions in Figure 1.5). In this case, the naphthalene can reside at two inequivalent sites in this crystal, so four full-field resonances are detected.

All of the samples studied in this work were amorphous or polycrystalline. Any resonance detected, then, is the sum of contributions from all possible orientations of the triplet relative to the external magnetic field. These resonances are called "powder patterns" and are similar to the patterns seen on amorphous samples by ESR. Typical full-field (Figure 1.5 transitions A and B) and half-field (Figure 1.5 transition C) PLDMR powder pattern data is shown in Figure 1.7.

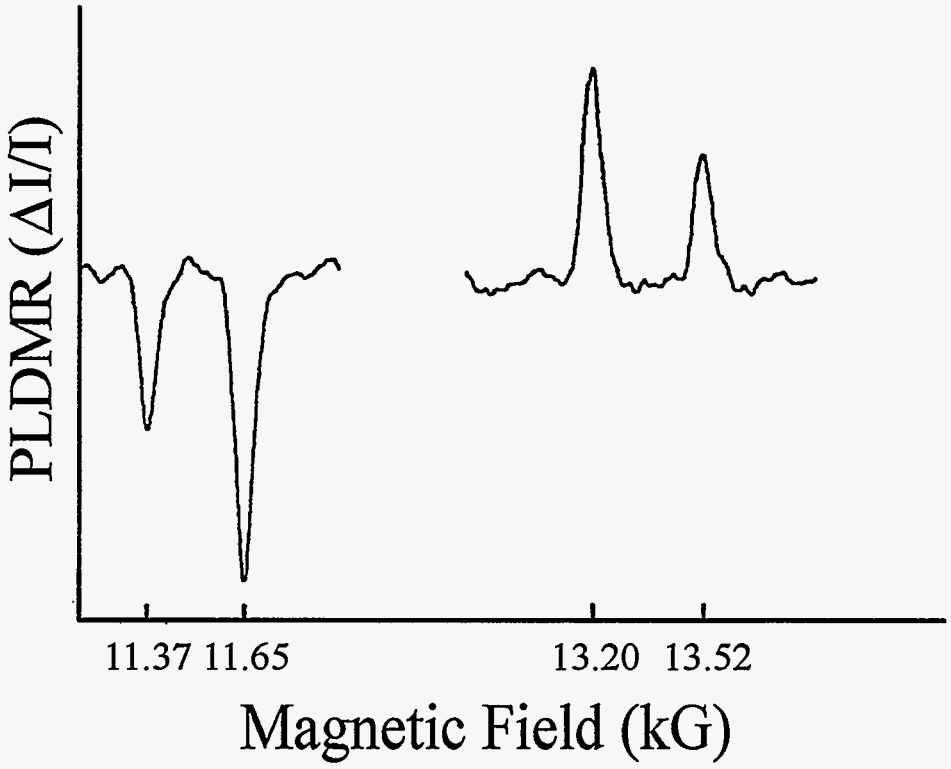

Figure 1.6 Typical single crystal triplet spectra.

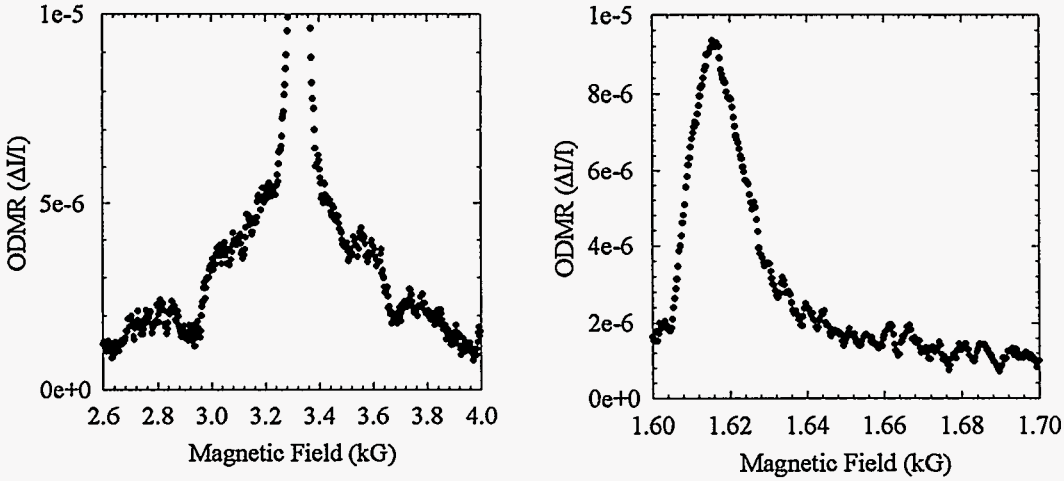

Figure 1.7 Full-field (graph on right) and half-field (graph on left) powder pattern spectra for LPPP.

The value of the magnetic field at which microwaves are absorbed and transitions occur is called the resonant field, H(n,ϕ). This field is a function of the cosine of the polar angle (n=cosθ) and the azimuthal angle ϕ. The analysis is considerably simplified in the axially symmetric case ($E = 0$), for then the transition field is independent of ϕ. In randomly oriented samples, the number of molecules oriented such that the resonance field H lies between θ and dθ is proportional to sinθdθ.

The intensity of the absorption in the field range H to H+dH is:[13]

$$dI = \sum_{\theta} A(H,n)\frac{dn}{dH}dH \tag{1.20}$$

where:

$H=H(n)$ has been inverted to $n=n(H)$

$A(H,n(H))$ is the transition probability

For E≠ 0 Atherton[5] derives the equations which give the critical points of the powder patterns. The critical points of the full-field powder pattern, as functions of $h\nu$ (the energy of a microwave photon), D and E, are:

shoulders at: $$H = (h\nu \pm D/2 \pm 3E/2)/g\beta \tag{1.21}$$

singularities at: $$H = (h\nu \pm D/2 \mp 3E/2)/g\beta \tag{1.22}$$

steps at: $$H = (h\nu \pm D)/g\beta \tag{1.23}$$

The critical points of the half-field powder pattern, as functions of $h\nu$, D and E, are:[14,15]

singularity at: $$H = \sqrt{\left(\frac{h\nu}{2g\beta}\right)^2 + \frac{D^2+3E^2}{(g\beta)^2}} \tag{1.24}$$

shoulder at: $$H = \frac{h\nu}{g\beta}\sqrt{1 - \frac{1}{2}\left(\frac{D-E}{h\upsilon}\right)^2} \tag{1.25}$$

Figure 1.8 shows Swanson's[16] computer simulations of three full-field powder patterns. The black curve, with E=0 G, has the shoulder and singularity of each transition occurring at the same field value. The blue curve, with E=87 G, moves the singularities toward $H=h\nu/g\beta$ and moves the shoulders outward. Finally, the red curve, with E=D/3G, merges the singularities at $H=h\nu/g\beta$ and merges the shoulders with the step. In each case, the step location has not changed.

Swanson's half-field simulation (Figure 1.9) is characteristically asymmetric. Only one singularity is observed at $H=H_{min}<h\nu/2g\beta$. The pattern at the step (H~1.667kG) gradually decreases to zero due to the zero transition probability at that value.

Example 1.1

The resonances in Figure 1.8 were calculated for polythiophene (discussed later) using $D/g\beta = 520$G. Using this value we can estimate the extent of the triplet wavefunction as follows:

Since $\left|\left\langle\frac{r^2-3z^2}{r^5}\right\rangle\right| \le \left|\left\langle\frac{2}{r^3}\right\rangle\right|$ (maximum occurs when $z=r$) we can rewrite equation 1.13:

$$r_{ub} \cong \left(\frac{3g\beta}{2}\right)^{\frac{1}{3}}\left(\frac{D}{g\beta}\right)^{-\frac{1}{3}} = \left(\frac{3(2.0023)\left(.9174\text{x}10\text{–}20\frac{erg}{G}\right)}{2}\right)^{\frac{1}{3}}\left(\frac{D}{g\beta}\right) = 30.2\left(\frac{D}{g\beta}\right)^{-\frac{1}{3}}\text{Å}$$

$$= 3.8\text{Å} \qquad (1.26)$$

Example 1.2

One of the triplet resonances in C_{60} films is measured to have a 250G difference between the low-field step and the high-field step. The extent of this triplet can be estimated right from the graph (see Equation 1.23) as:

$$\Delta H = H_{high} - H_{low} = (h\nu + D)/g\beta - (h\nu - D)/g\beta = 2D/g\beta \qquad (1.27)$$

Therefore, from 1.26:

$$r_{ub} \cong 30.2\left(\frac{D}{g\beta}\right)^{-\frac{1}{3}}\text{Å} = 30.2(125)^{-\frac{1}{3}}\text{Å} = 6\text{Å}$$

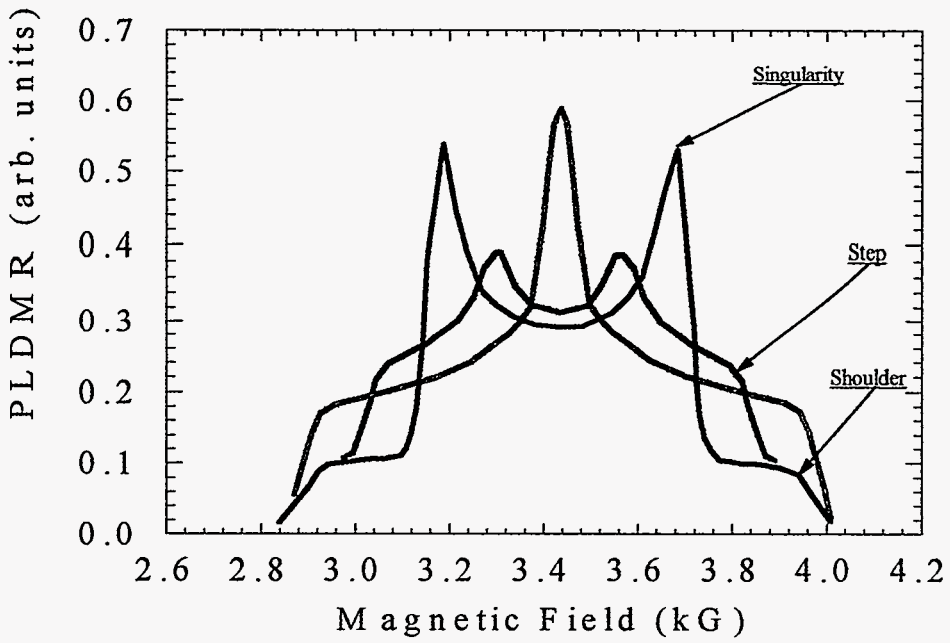

Figure 1.8 Computer simulation of full field triplet powder patterns. All simulations used $D/g\beta$=520G, $h\nu$=9.352Ghz and H_1 perpendicular to H_0. The black curve results from $E/g\beta$=0G, the blue from $E/g\beta$=87G and the red from $E/g\beta$=D/3G.

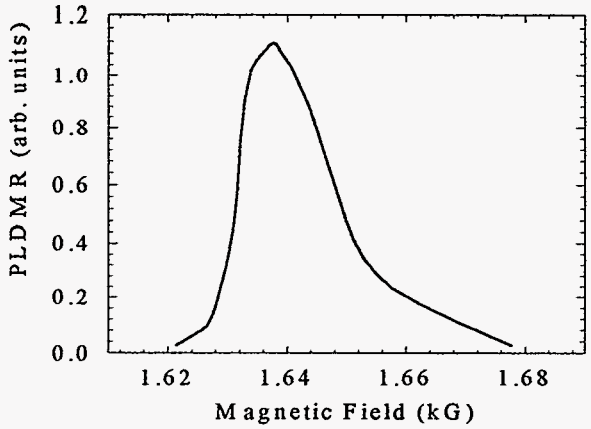

Figure 1.9 Computer simulation of half field powder pattern. This simulation used $D/g\beta$=602G, E=0, $h\nu$=9.352Ghz and H_1 perpendicular to H_0.

1.4 Experimental Techniques

There are a number of experimental methods used to perform PLDMR experiments. In one method, no external magnetic field is applied, so the splitting is accomplished by spin-spin interactions ($\Delta E_{S\text{-}S}=h\nu$). This technique, called zero-field PLDMR, requires the use of a microwave sweep generator capable of generating microwaves over an octave of frequencies and a cavity capable of continuous tunability over the same range. While this technique frees one from the use of a magnetic field and the analysis of triplets randomly orientated with respect to that field, the added complications of the microwave gear, in addition to the inability to analyze samples with no energy splitting in zero-field, restrict its applicability.

Single crystal samples can be used to measure the precise zero-field splitting (zfs) parameters. However, for amorphous samples, the determination of the zfs parameters is also possible, as described above.

Other PLDMR methods utilize magnetic fields. One method varies the magnetic field sinusoidally and uses a lock-in amplifier to arrive at a derivative spectra similar to an ESR spectrum. Our method chops the microwave excitation source to get the spectra without further data processing.

Two cavity geometries are extensively used in PLDMR experiments. In the first method, the cell is located so that H_1, the microwave magnetic field, is parallel to H_0, the magnetic field provided by the electromagnet. This method allows optical pumping with a circularly polarized laser and it allows the entire half-field ($\Delta m_S \pm 2$) powder pattern to be observed. In some systems, such as mercury vapor, the resonance can only be observed by monitoring the light emitted along the magnetic field.[17]

If the cavity is located such that H_1 is perpendicular to H_0, as in our spectrometer, we can observe the $\Delta m_S=\pm 1$ resonance and most of the $\Delta m_S=\pm 2$ resonance. Optical access, for both the excitation and the luminescence, is only necessary through the side perpendicular to the magnetic field.

1.5 Experimental Apparatus

The PLDMR system was assembled by L.S. Swanson around 1989[16] and was extensively upgraded by the author from 1994-1997. The schematic of the PLDMR system is shown in Figure 1.10. The apparatus has a great deal of flexibility; with minor modifications it is able to measure PL, PLDMR, electroluminescence detected magnetic resonance (ELDMR), electrically detected magnetic resonance (EDMR), photocurrent detected magnetic resonance (PCDMR), and frequency resolved optically detected magnetic resonance (FRODMR) (described below). The addition of a Digital Storage Scope and amplifier would also allow time resolved optically detected magnetic resonance (TRODMR) experiments.

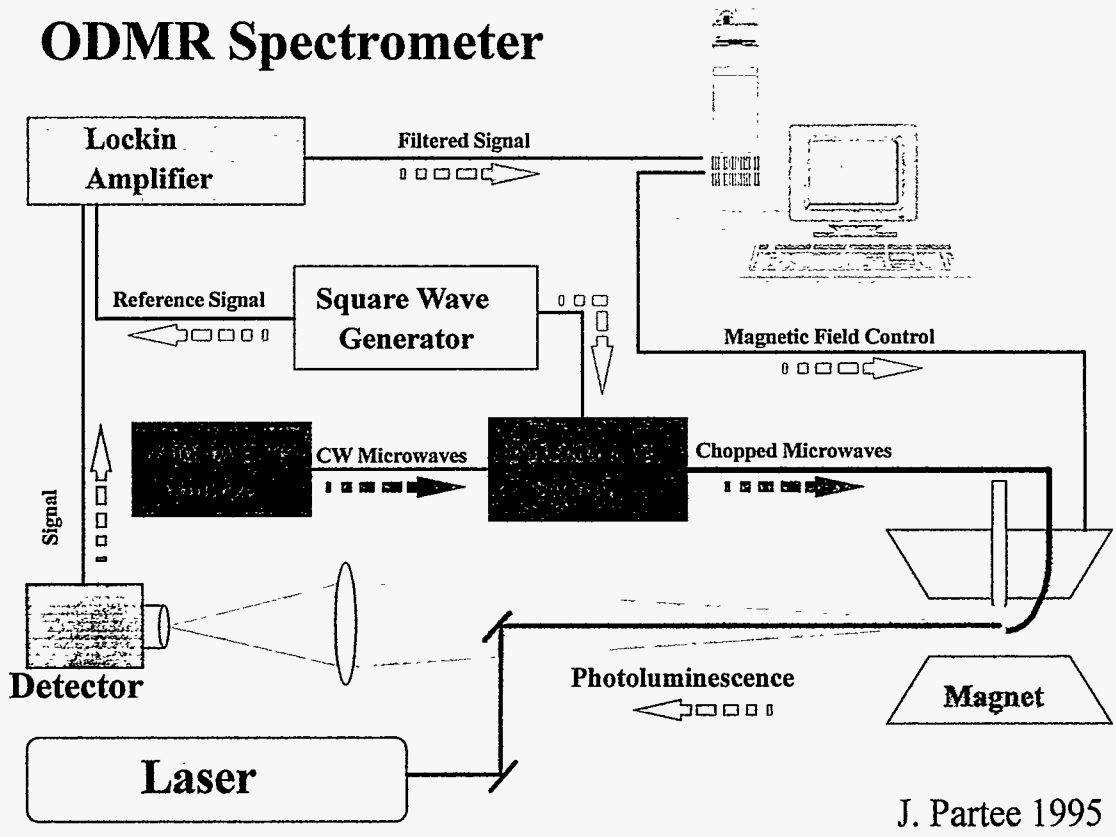

Figure 1.10 Schematic of ODMR Spectrometer.

For PLDMR experiments, the laser or UV lamp excitation is directed via mirrors and lenses onto a sample sealed in a 5mm outer diameter quartz tube. The sample is located in a quartz cryogenics system (allowing temperatures down to 6K) which is inside a larger TE_{103} microwave cavity resonating at ~9.35GHz. The sample is carefully placed at a region of maximum magnetic field and consequently minimum electric field. The quartz jacket of the cryogenics passes through the cavity at regions with small current density so the internal magnetic field is approximately parallel at the location of the sample.

The microwave power, up to 1.74W, is supplied by a Gunn diode oscillator, amplified by a Hughes traveling wave tube amplifier. Proper coupling to the cavity is accomplished by varying the microwave frequency, the frequency meter, and the tuning screw adjacent to the iris between the cavity and the waveguide to which it is connected. The microwaves are chopped, for lock-in amplification detection, by a square wave generator connected to a pin diode. The magnetic field is supplied by a Harvey-Wells electromagnet and power supply.

Optical access to the cavity is achieved through the face parallel to the magnetic field. The PL from the sample is collected and sent into a detector; either a silicon detector or a photomultiplier tube. This signal is sent to the lock-in amplifier which pulls out the part which has been affected by the microwaves and reports that information to the data acquisition computer. The computer prints, in real time, a plot of PLDMR vs. magnetic field strength. The relative change in the luminescence intensity ($\Delta I/I$) is typically 1 part in 10^3 to 10^6. We note, in passing, that much of the reason for this sensitivity can be directly attributed to the laser intensity stabilizer which decreases the laser noise by a factor of ~20.

ELDMR, PCDMR and CDMR require electric feedthru connections which tends to couple significant amounts of microwave power out of the cavity and leak air around the cryogenic o-ring which seals the sample rod into the cryogenics. The first problem is minimized by using small wires and keeping the amount of metal material to a minimum. The second problem is solved by replacing the previously used teflon rod with wires running down the side with a two-stage quartz rod designed by the author. The top of the quartz rod is hollow, and the wires are fed through the center of the rod and sealed at the top with

epoxy. The last inch of the rod is solid and a flat platform for the sample is sanded into this part. The two stages of the rod are bonded using an acetylene torch and two small holes are cut to allow the exit of the feedthru wires.

1.6 Novel Magnetic Resonance Techniques

In the last 30 years, the basic technique has been expanded to include photoinduced absorption (PADMR) and electroluminescence (ELDMR) detected magnetic resonance. In addition, measuring the changes in the conductivity (or current) at magnetic resonance (CDMR) and in the photocurrent (PCDMR) provides additional physical information with minor modification to the ODMR spectrometer. Finally, time-resolved measurements (TRODMR) and frequency domain measurements (FRODMR), described below, give new insight into the lifetimes of paramagnetic species.

1.7 Lifetime Measurements

Time resolved optically detected magnetic resonance (TRODMR) and frequency resolved optically detected magnetic resonance (FRODMR) are two novel experimental methods used to gain information about the type of recombination processes and the lifetimes of the spin states affected by the application of microwave radiation. Both techniques have been used previously on diverse systems such as amorphous silicon,[18,19] porous silicon[20] and π-conjugated polymers.[21]

These two measurements can be simply related by considering an electrical circuit where a resistor and a capacitor are connected in series to a square wave generator. To find the RC constant (or τ, the lifetime) of this low-pass circuit there are two methods that can be employed. The simplest way to measure RC would be to connect an oscilloscope across the capacitor and look at the waveform. It is well known that the rise time of an RC circuit is 2.2RC, so by observing the rise time on the oscilloscope we can find τ (or RC). This method is analogous to TRODMR.

A second, more difficult, way to find RC involves varying the frequency, ω, of the square wave generator and observing the gain. Plotting the gain vs. ω and using a curve fitting program will reveal τ. This method is analogous to FRODMR.

1.8 PLDMR Lifetimes

In order to find a PLDMR, two conditions must be satisfied: (i) the populations of the different magnetic spin sublevels must be unequal and (ii) the lifetime affected by the resonance conditions must lie within the detectable range (~10μs to 10ms). To satisfy condition (i) the magnitude of the departure from equality is defined:[22]

$$P_{ij} \equiv \frac{n_i - n_j}{n_i + n_j} \tag{1.28}$$

where:

n_i and n_j are the populations of levels i and j

The spin polarization of a system in thermal equilibrium follows Boltzmann statistics:

$$P_{ij} = e^{-\Delta E/k_B T} \tag{1.29}$$
$$n_1 = n_0 e^{-(E_1 - E_0)/k_B T} \tag{1.30}$$
$$n_0 = n_{-1} e^{-(E_0 - E_{-1})/k_B T} \tag{1.31}$$

where:

E is the energy

1,0,-1 subscripts refer to the appropriate spin level

k_B is the Bolzmann constant

The spin-lattice relaxation time, T_1, characterizes the rate at which the departure of the spin polarization from Boltzmann statistics decays to thermal equilibrium. The response of the PL following microwave excitation depends exponentially on the spin-lattice relaxation time (Figure 1.11). When the microwave excitation is turned off, PL decays exponentially to the

original steady-state level at a rate governed by the radiative recombination lifetime (τ_R). For simplicity, we assume $T_1=\tau_R$.

1.9 Time Resolved Optically Detected Magnetic Resonance

The typical time resolved (TR) experiment is accomplished by taking a sample and exciting it by a δ-function light pulse. The resulting luminescence is detected in a very narrow gate some time, t, after the pulse. A laser is used to generate the δ-function light pulses, and a boxcar integrator scans the decay curve.

For observation of TRODMR, the magnetic field is set to the peak of a resonance and the microwaves are chopped at 70-80Hz. A signal averager, triggered by the microwave chopper, is used to detect the PL.[23]

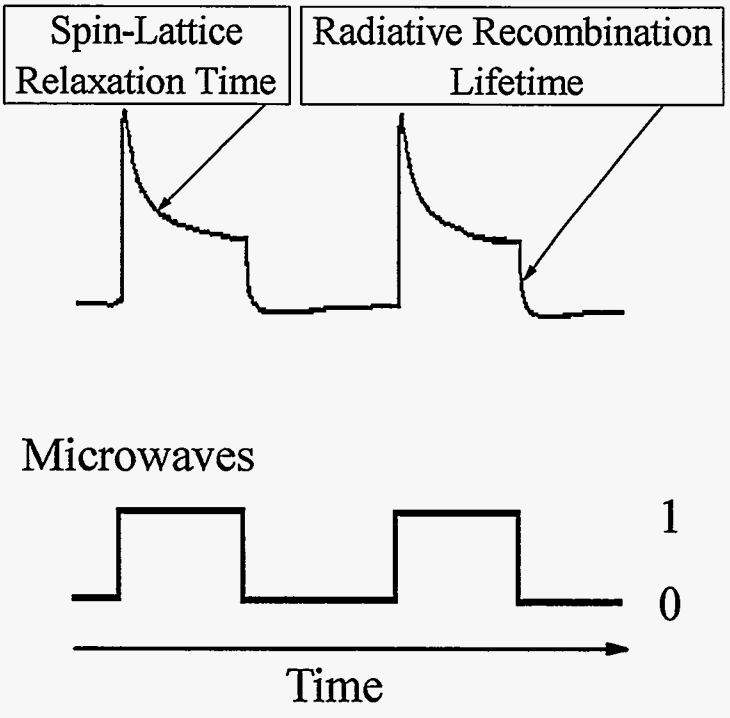

Figure 1.11 Response of photoluminescence from a ZnS:Cl crystal[22] to the application of microwaves at a magnetic field corresponding to a resonance.

Figure 1.12 (b) shows the typical response of the PL to square wave chopped microwaves. Simple exponential evolution toward equilibrium is observed at the application and the removal of microwaves. This type of TRODMR signal corresponds to a process which is only indirectly affecting the radiative recombination. For instance, enhancing the recombination of non-radiative polarons, which are serving as singlet exciton quenching centers, could give such a signal. The application of microwaves are not directly affecting those species involved in photoluminescence. Therefore, processes exhibiting this type of behavior are called an indirect process or a distant-pair shunt process.

In some TRODMR experiments, a strong positive transient spike is observed when microwaves are applied and a negative spike when microwaves are removed (Figure 1.12 (a)). This signal could be generated if the thermalization time is less than the lifetime ($T_1 < \tau$) in which case the system's electronic levels would follow Boltzmann statistics. Microwave power at resonance would create a small positive effect. This process results from radiative distant pairs. If, however, $T_1 > \tau$ the microwave power at resonance will decrease the antiparallel spin pair density (radiative geminate pairs) leading to a theoretical response shown in Figure 1.12 (c). In either the case of the radiative distant pairs or the radiative geminate pairs, the application of microwaves directly affects the PL.

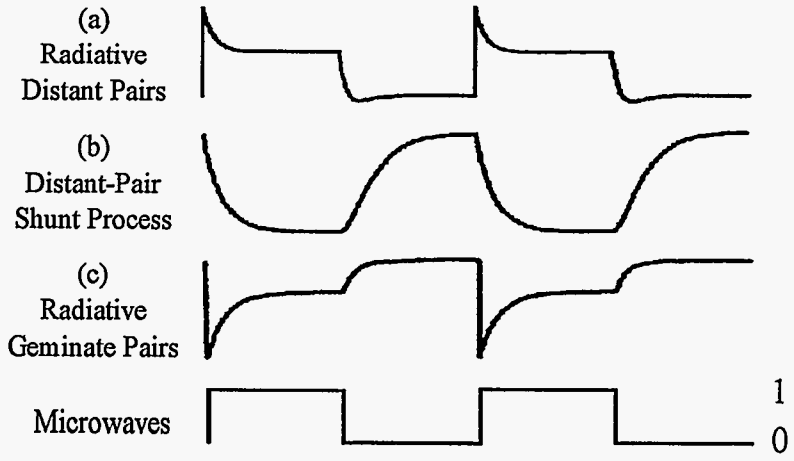

Figure 1.12 Theoretical simulation of the response of the luminescence intensity to a square wave modulation of the microwave power.[18,24,25]

In Figure 1.12 (b) the PL decreases when the microwaves are turned on. This will lead to a quenching ODMR resonance. Similarly, many systems show the same behavior as Figure 1.12 (b), except that the microwaves enhance the PL leading to an enhancing ODMR resonance. Therefore, TRODMR can be employed to gain important information about the processes involved in PL.

1.10 Frequency Resolved Optically Detected Magnetic Resonance (FRODMR)

The simplest form of a frequency resolved experiment is known as the "quadrature method".[19] The excitation is modulated and detected with a lock-in amplifier set in quadrature (phase of the lock-in $\pi/2$ ahead of the phase of the modulation). If the microwave chopping frequency can be varied, FRODMR data can be simply taken with minor modifications to the ODMR data acquisition program. One simply sets the magnetic field on resonance and takes a number of data points at each modulation frequency.

1.11 Non-radiative Processes

The bulk of the work done here on FRODMR involves indirect processes. These processes are well described by the two equations:

$$A(t) = A_0\left(1 - e^{-\frac{t}{\tau}}\right) \tag{1.32}$$

$$D(t) = D_0 e^{-\frac{t}{\tau}} \tag{1.33}$$

where (1.32) describes the system when the microwaves are turned on and (1.33) describes the system when the microwaves are turned off. These same two equations describe an RC circuit where the voltage is measured across the capacitor (Figure 1.13). Therefore, we can use the well known analysis of the RC circuit to find an expression that will relate the timeconstant, τ=RC, to the chopping frequency, f.

$$R = \frac{1}{\sqrt{1+(\omega RC)^2}} \tag{1.34}$$

$$\theta = \arctan(\frac{v_1}{v_2}) = \arctan(\omega RC) \tag{1.35}$$

where:

V_2 and V_1 are described in Figure 1.13

ω is the frequency of the sinusoidal input

θ is the angle between the voltage across the resistor (R) and the capacitor (C)

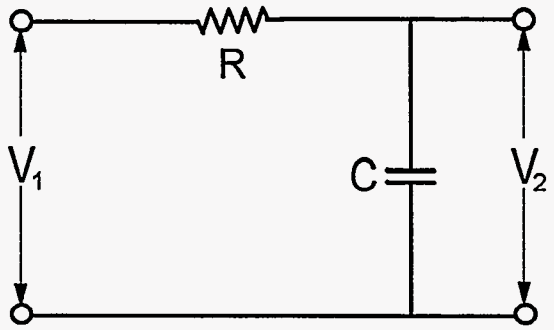

Figure 1.13 Diagram of RC low-pass filter.

The data from a lock-in amplifier is sometimes given in terms of X and Y instead of R and θ, but the usual formulae ($X=R\cos\theta$, $Y=R\sin\theta$) can be used for conversion. Note that often the X signal is called the "in-phase" and the Y signal is called "quadrature". When V_1 is connected to the output of a waveform generator, V_2 can be measured as a function of ω. Figure 1.14 shows experimental and theoretical curve fits for the four quantities that can be measured with a lock-in amplifier. The value for R is 182Ω and the value for C is 1μF.

The theoretical fits, using Equations (1.34 and 1.35) are quite good except for the case of θ, which suffers from phase delays in the wiring at higher frequencies. These phase delays will not affect R, but they will slightly affect X and Y.

It is easy to verify that the peak of Y and the point where X=Y occurs when:

$$\omega\tau=1 \tag{1.36}$$

Furthermore, the breakpoint or "knee" of R on the log-log plot (Figure 1.14(b)) also occurs when $\omega\tau=1$.

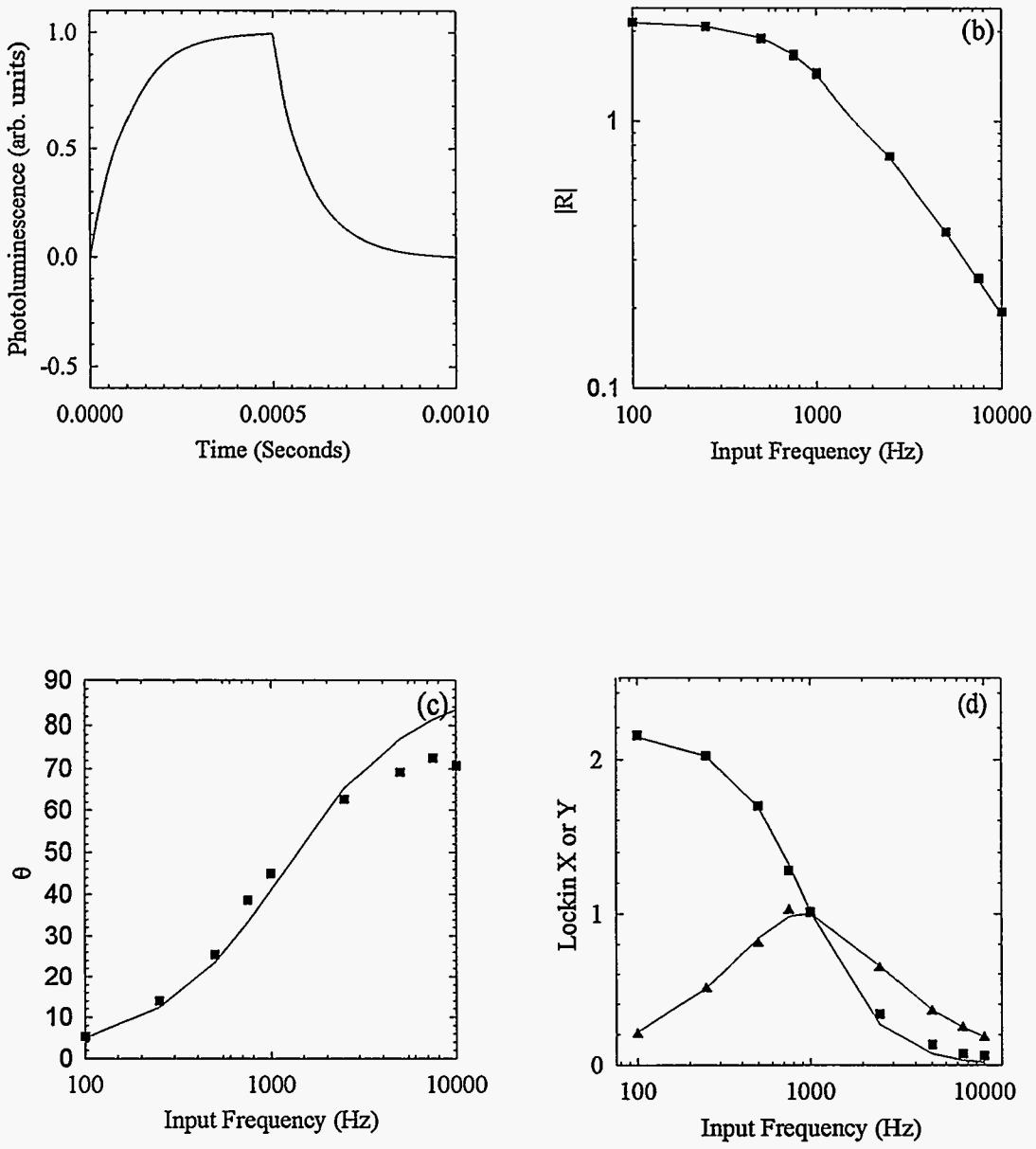

Figure 1.14 (a) PL output modelled by voltage in an RC low-pass filter Output from lock-in amplifier (data points) and theoretical fits (lines) for: (b) R, (c) θ and (d) X (squares) and Y (triangles).

Depinna[19] derives the same results using a more rigorous method, reproduced below. Depinna assumes that the kinetics are first-order and monomolecular. The excitation (in our case, microwaves) are assumed to be modulated at an angular frequency ω.

$$G(t)=g\sin(\omega\tau) \tag{1.37}$$

where g is the amplitude of the modulation.

For a component of the luminescence with a lifetime τ, we write

$$\begin{aligned} I(\tau,t) &= \int_{-\infty}^{t} \tau^{-1}\exp[-(t-u)/\tau][g\sin(\omega t)]du \\ &= g(1+\omega\tau)^{-1}[\sin(\omega\tau)-\omega\tau\cos(\omega\tau) \end{aligned} \tag{1.38}$$

If $\tan\phi=\omega\tau$, we obtain

$$I(\tau,t) = g\cos\phi\sin(\omega\tau-\phi) \tag{1.39}$$

The lock-in output is given by

$$S(\tau) = (2\pi)^{-1}\omega\int_0^{2\pi/\omega} I(t)R(t) \tag{1.40}$$

where $R(t) = \sin(\omega t)$ for the in-phase component (X) and $R(t) = -\cos(\omega t)$ for quadrature(Y).

Solving integral (1.40) leads to

$$X = \frac{g'}{\left(1+(\omega\tau)^2\right)} \tag{1.41}$$

$$Y = \frac{g'}{\left((\omega\tau)^{-1}+(\omega\tau)\right)} \tag{1.42}$$

where g'=g/2. Using (1.41) and (1.42) to calculate R (and neglecting g) gives:

$$R = \frac{1}{\sqrt{1+(\omega\tau)^2}} \tag{1.43}$$

which is the same as (1.34). Therefore, as expected, the results from a simple RC circuit and those calculated by Depinna[19] are equivalent. Furthermore, since the lock-in amplifier

analyzes the first harmonic of the signal, the treatment using a square wave modulation also leads to Equation (1.43) as shown by Botta's Equation (4)[21] and Kim's equations (3.40) and (3.41).[26]

1.12 Radiative Processes

The nonradiative process is nicely modeled by an RC low-pass filter. The radiative process can be satisfactorally modeled numerically. Figure 1.15 (a) and (c) show two radiative waveforms which were analyzed by multiplying the waveform by sin(ωt) for X and cos(ωt) for Y and integrating. Figure 1.15 (b) and (d) show the modulation frequency dependence of the two waveforms. The solid line corresponds to the modulation frequency dependence of a non-radiative process (Equation 1.43).

It is somewhat tricky to ascertain whether one is measuring a non-radiative process (Figure 1.14) or a radiative process with a fast risetime (Figure 1.15 (a)). However, θ (Figure 1.14 (c)) changes from 0° to 90° for the non-radiative process whereas θ~0 for the radiative process. Discerning the difference can still be a problem,though, if the lifetime lies outside of the range of the spectrometer. Although no radiative processes were observed in this work (with the possible exception of C_{70}), they should be distinguishable from the non-radiative processes if measurements on a suitable sample are made.

1.13 Comparison of TRODMR and FRODMR

TRODMR and FRODMR are entirely equivalent in systems displaying first order kinetics. However, if the response involves more than an exponential decay with a single lifetime, TRODMR can become complicated or ambiguous. This may be clearly seen by considering a system with two first order lifetimes, such as a system with polarons at different sites. By varying the excitation pulse length in TRODMR, the relative contributions of the fast and slow components will be changed. This is a result of the build up of the steady state populations n_i during the pulse.

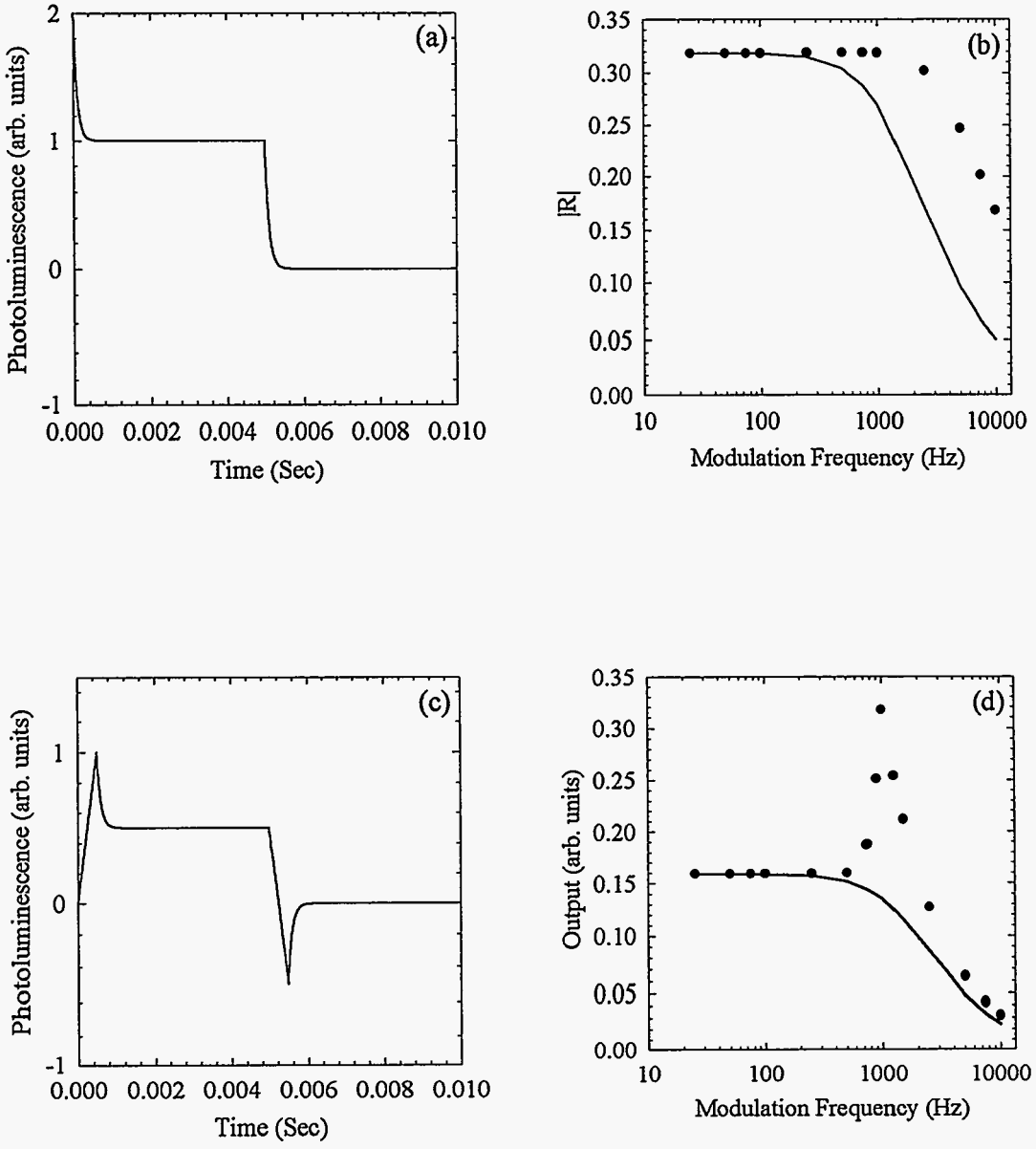

Figure 1.15 (a) Waveform with zero risetime and (b) the modulation frequency dependence. (c) Waveform with finite risetime and (d) modulation frequency dependence.

$$n_i \propto G_i[1-\exp(-\frac{t}{\tau_i})] \tag{1.44}$$

where G_i is the excitation rate during the pulse.

Therefore, the fast pulses will accentuate the fast polarons compared to the slow polarons. For FRODMR the excitation source is continuous, so the two components are present in proportion to their relative intrinsic populations.

Another serious problem with TRODMR was discovered by Tsang.[27] For distant pair systems, the PL intensity can be described by:

$$I(t) \sim I_o t^{-1} \tag{1.45}$$

In this case, the PL lifetime is always equal to the gate delay, since

$$\tau(t) = -\frac{dt}{d(\log I)} = t \tag{1.46}$$

This may account for time resolved measurements on a-Si:H whose lifetime increased as a function of the year measured. In 1976, the reported lifetime using time resolved spectroscopy was 20ns.[28] By 1979, the lifetime had increased to 20μs[27] further increasing to 300μs[29] in 1982. Frequency resolved measurements avoided this problem and gave a τ of 3ms[19] in 1984.

1.14 FRODMR Experimental Details

FRODMR is a very powerful and simple technique. Data are taken by simply varying the microwave modulation frequency and recording the output of the lock-in amplifier. That output is usually given as X and Y which can be converted into R. Equation (1.43) can then be used to find τ.

Although FRODMR is simple, there are multiple sources for experimental errors. Not least among those sources is the lock-in amplifier. The basis of the lock-in detection is

accomplished by compressing all of the signal information into a very narrow bandwidth and amplifying only frequencies in this bandwidth. However, there are a number of features on the amplifier which can provide anomalous readings. The lock-in has notch filters at 60Hz and 120Hz which are used to filter out the noise from the power lines. This feature must be disabled to allow the response to be independent of frequency. However, the feature which enables the lock-in to track the modulation frequency should be enabled. There are a number of filters which can be used to reject signal frequencies which are not interesting. Figure 1.16 shows the lock-in response to an RC circuit under various conditions. For a sine wave modulation, the flat, low-pass, and band-pass filters give the same results. For square wave modulation, the low-pass and band-pass filters are equivalent, but the flat filter (which allows harmonics to contribute) gives higher values at low frequencies.

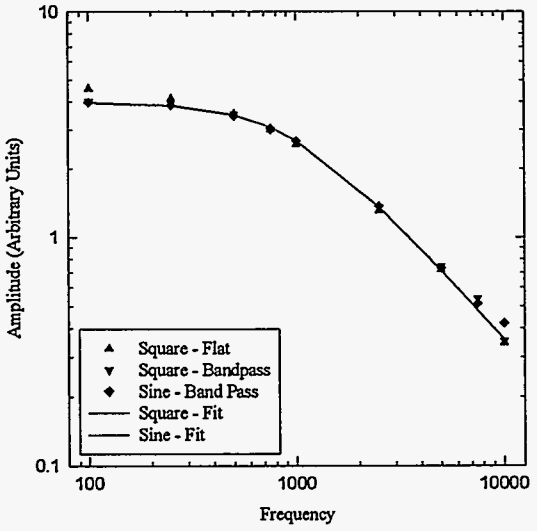

Figure 1.16 Lock-in response to RC circuit.

A common mistake with the FRODMR technique lies in the choice of detectors. The speed of silicon detectors is limited by the RC circuit in the amplifier, so the measurements using a silicon detector with the wrong bandwidth can give wrong answers. The rise time of the circuitry should obviously be above the inverse of the maximum

modulation frequency used. In addition, all the circuitry from the detector to the lock-in must be checked to avoid errors. Commercial LEDs operate in the hundreds of nanoseconds range and can be used to test the circuitry. Figure 1.17 demonstrates that using the PMT with the lock-in set at 100μV allows us to make measurements up to 75kHz. The distribution of the data points reflects the voltage from the Wavetek oscillator which varies by ±5%. No sign of a lifetime-induced breakpoint is seen.

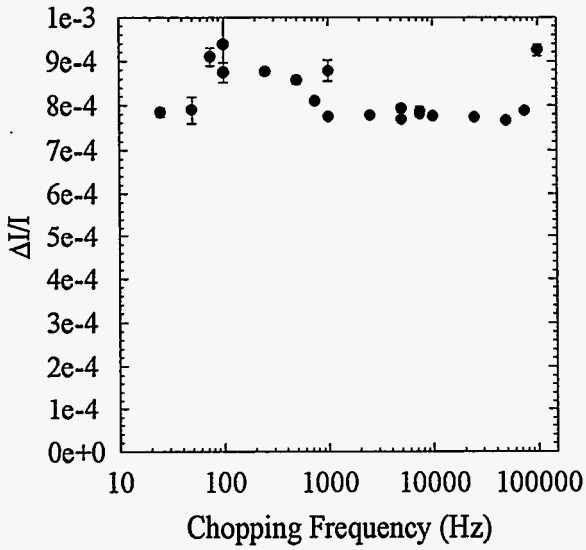

Figure 1.17 System response to a commercial LED with risetime of 50ns.

CHAPTER 2. INTRODUCTION TO π-CONJUGATED SYSTEMS

For the past half century, conventional insulating polymer systems have rapidly been accepted in place of conventional structural materials such as wood, metal and ceramics. The high strength, light weight, low cost and easy processing of these polymers is largely responsible for their extensive use. In 1977, the first electrically conducting organic polymer, doped polyacetylene $(CH)_x$, was reported.[30] This discovery opened up a new class of polymers called π-conjugated polymers named for the overlap of carbon p_z orbitals and alternating carbon-carbon bond lengths. These conducting polymers (actually semiconducting polymers) may be an attractive alternative to conventional semiconductors for a number of reasons; easily modified band gap, electroluminescent properties, flexibility, solubility, and low cost. Some of the applications envisioned for these conjugated polymers are: lasers, light emitting diodes (LED), EMI shielding, batteries, structural materials, photovoltaic devices, thin film transistors, and photodiodes.[31]

It is the LED application that captures the greatest interest of physicists at this time. Currently, LEDs are produced using inorganic III-V or II-VI compounds. The III-V materials, such as GaAs, are moderately expensive and difficult to manufacture. The II-VI materials, such as ZnS, provide low efficiency and poor reliability. Conjugated polymers can have high quantum yields and are produced quite cheaply. However, questions about the long-term stability of the devices remain to be answered. Two companies, UNIAX and Cambridge Display Technologies, have been formed in an attempt to bring this technology to the market. Typical polymeric LEDs are built by depositing indium-tin-oxide (ITO) on a substrate, usually glass. The polymer solution is then spin-coated onto the ITO. Finally, a metal contact (e.g. aluminum) is evaporated onto the top surface of the polymer layer. Figure 2.1 shows a schematic of such a device. When a bias is applied, the electroluminescence is transmitted through the transparent ITO and substrate. Investigations into the EDMR, ELDMR, and PCDMR (described previously) of these devices should lead to important insights into the spin-dependent recombination processes which may help to improve the efficiency, lifetime, and intensity of the devices.[32]

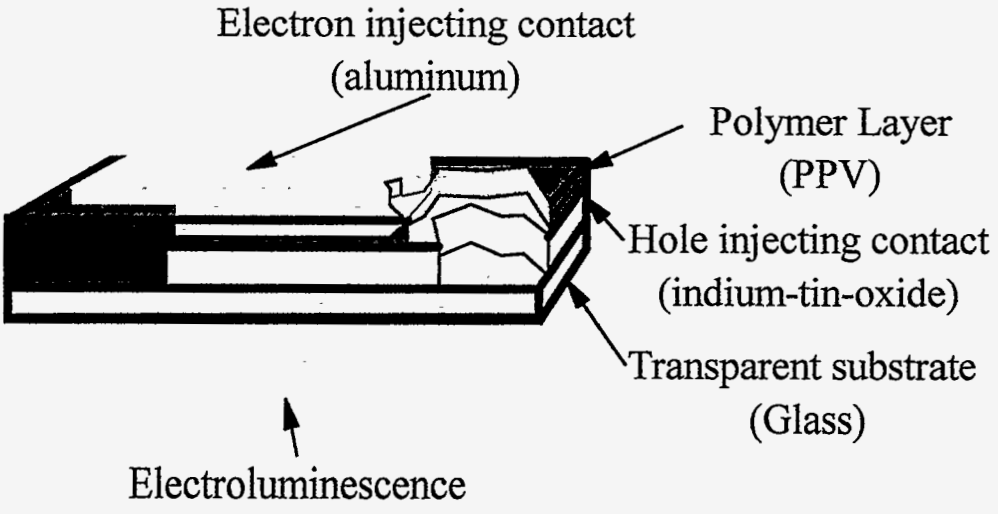

Figure 2.1 Typical structure for a semiconducting polymer LED.

2.1 Introduction to π-conjugated Polymers

Linus Pauling was the first chemist to express the idea of hybridization[33] which is critical to the explanation of these organic polymers. While many chemical structures manifest hybridization, carbon is remarkably flexible, exhibiting three schemes: sp, sp^2 and sp^3. The hybrid sp orbital (e.g. BeF_2 or C_2H_2) yields two bonding hybrid orbitals. Similarly, the sp^2 (e.g. BF_3 or C_2H_4) and sp^3 (e.g. CH_4 or C_3H_8) yields three and four bonding hybrid orbitals respectively. The important feature which separates ethylene (C_2H_4) and acetylene (C_2H_2) from the other organic molecules like propane (C_3H_8) or methane (CH_4) is the existence of the π-bond. One singly occupied sp^3 orbital from each adjacent atom in propane (Figure 2.2a) overlaps endwise in the region between the carbon nuclei forming a strong σ-bond. The other sp^3 orbitals from each carbon atom overlap with the singly occupied σ-orbitals of the hydrogen atoms forming strong σ-bonds. Similarly, in ethylene (Figure 2.2b), the carbon-hydrogen bonds are σ-bonds, but the moderately high reactivity shows that some of the outer electrons are available for reactions. The remaining p_z electrons account for the reactivity and are at a minimum energy when the orbitals are parallel to each other. In this position, the orbitals overlap sideways (laterally) and form a

relatively weak covalent bond called a π-bond. Similarly, the triple bond in acetylene (Figure 2.2c) will have two π-bonded electron pairs perpendicular to each other.

Other important constituents of these organic polymers are benzene rings and derivatives. Like ethylene, benzene is sp^2 hybridized with each carbon atom forming a bond with two neighboring carbon atoms and one hydrogen atom. The remaining electron lies above and below the plane of the molecule forming a π–bond (Figure 2.3).

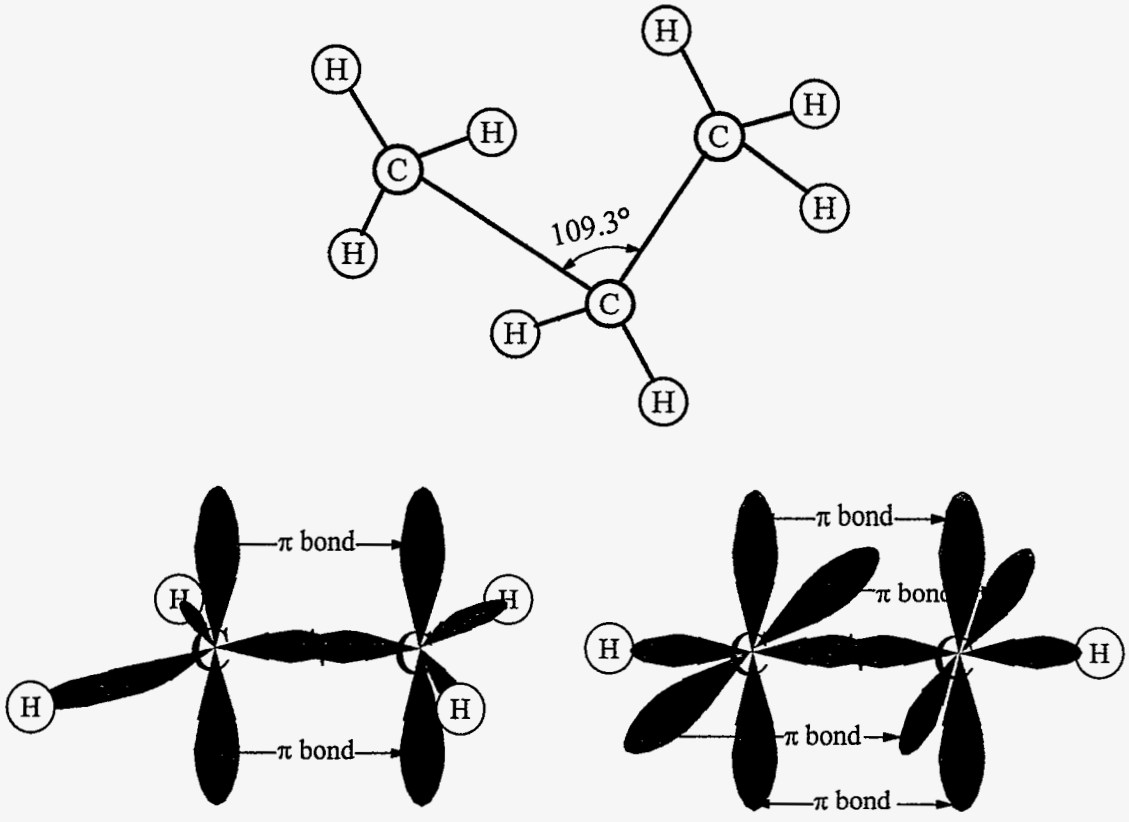

Figure 2.2 (a) Propane (b) ethylene (vinylene) (c) ethynylene (acetylene) The blue orbitals form σ-bonds. The red p_z orbitals form π-bonds.

Because of these π-electrons, a delocalized electron cloud forms above and below the benzene ring. A benzene molecule is considered to be a resonance hybrid. X-ray diffraction and infrared spectroscopy studies reveal that the six carbon atoms form a regular hexagon.[33] The molecule is planar and all carbon-carbon bonds are identical. No single

configuration of double and single bonds can be drawn which is consistent with these data (Figure 2.4), therefore, the benzene molecule is often represented with a circle in the center. Aromatic rings can incorporate a heteroatom such as sulphur (thiophene), oxygen (furan), or nitrogen (pyrrole) (Figure 2.4).

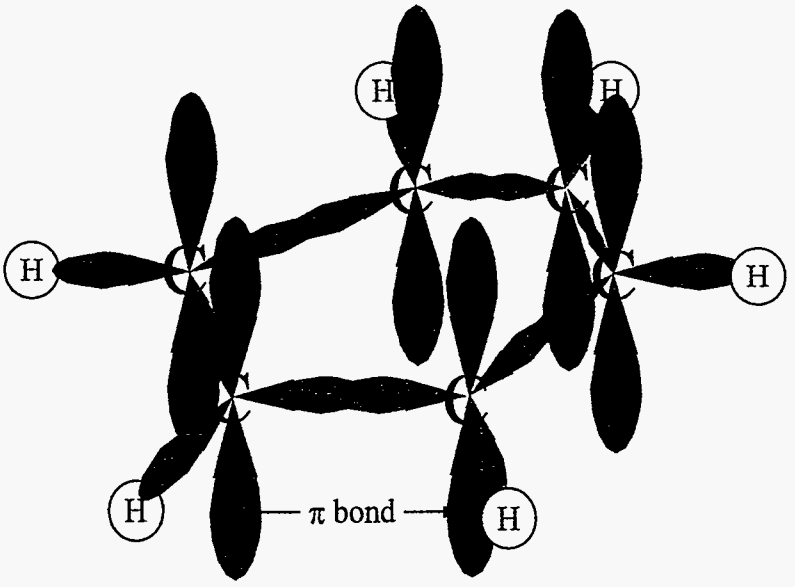

Figure 2.3 Representation of benzene molecule with p_z orbitals shown in red.

2.2 Photoexcitations in π-conjugated Polymers

In 1979-1980 Su, Schrieffer and Heeger[34,35] modeled the 1-D degenerate ground state polymers to show that solitons are the primary excitation. Simple polymers such as trans-polyacetylene (t-(CH)x) were well described by this model. The behavior of other π-conjugated polymers with nondegenerate ground states is quite different, mainly because solitons are not stable on these types of chains. Polarons and bipolarons (Figure 2.5) are invoked to explain the behavior in these polymers which constitute the bulk of known π-conjugated polymer systems. However, this continuum band picture does not accommodate tightly bound localized molecular singlet and triplet excited states.[4] Yet these latter states have provided the basis for understanding the photophysics of π-conjugated organic molecular solids such as anthrecene.[8]

The ground state of most π-conjugated polymers is not degenerate. Solitons are not stable on these types of polymers and the primary charged photoexcitations are believed to be polarons. Twists and bends in the polymer structure may break the π-bonds, shortening the conjugation length (the length of the uninterrupted π orbitals). The shorter the conjugation length, the higher the energy separation between the ground state highest occupied molecular orbital (HOMO) and lowest unoccupied molecular orbital (LUMO). Therefore, many twists and turns lead to higher band gap polymers. In addition, SSH theory predicts the existance of states in the gap. It should be noted that support in the physics community exists for both the continuum picture[36-38] and the molecular excitonic picture.[39-42]

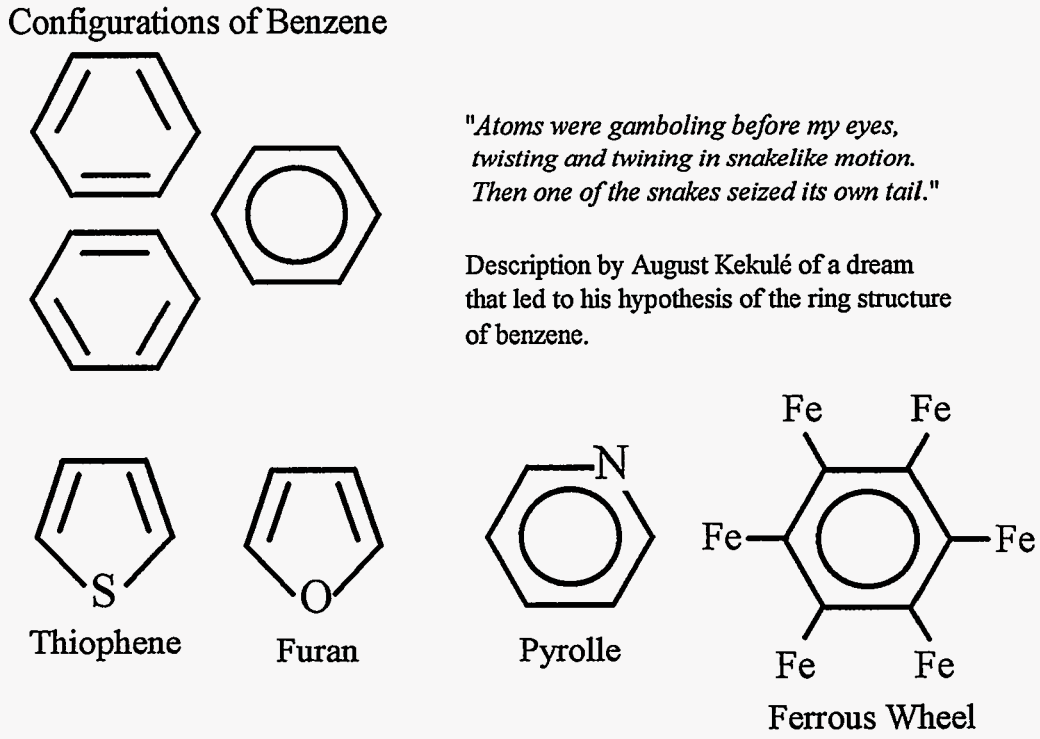

Figure 2.4 Benzene with two possible bonding configurations.
Other molecules: thiophene, furan, pyrolle, ferrous wheel.

The most important excited states in π-conjugated polymers are the neutral photoexcitations. It is generally accepted that short-lived (400ps)[43] singlet excitons are responsible for the photoluminescence in conjugated polymers. However, recent experiments[44] have yielded weak phosphorescence indicating a weak radiative recombination path for triplets. Significant decay channels in nondegenerate ground state π-conjugated polymers are shown in Table 2.1. Figure 2.5 shows the qualitative scheme for the energy levels in the polymers.

The photoluminescence (PL) spectra of the films and the electroluminescence (EL) spectra of the polymer diodes have usually been found to be nearly identical. Therefore, the emission process should be the same. This radiative process is most likely the fusion of free polarons which result from the injected electrons and holes, into singlet excitons which relax to the 1^1B_u (notation from group theory) energy level and then decay radiatively to the ground state (Equation 2.1). In the case where the polaron pairs have parallel spins, the process outlined in Equation 2.2 will occur.

Whereas singlet excitons are responsible for the radiative recombination, it is now believed that the recombination of trapped polaron pairs (Equation 2.3) is nonradiative. Modulation frequency measurements made in this work support this interpretation. This spin-dependent process is most likely to occur if the spins are antiparallel. The trapped polaron pairs can also function as nonradiative singlet exciton S_1^* quenching centers (Equations 2.4 and 2.5).

Another spin-dependent process, which is especially important in polymer LEDs, is the fusion of like-charged spin-½ polarons to doubly-charged spinless bipolarons (Equations 2.6 and 2.7). The mobilities and lifetimes of these bipolarons are probably longer than that of polarons since the most likely decay channel is that shown in Equations 2.8 and 2.9.

Radiative triplet-triplet fusion (Equation 2.10) is often observed in small molecules like anthracene. However, in π-conjugated systems a more likely recombination pathway is shown in Equation 2.11.

Table 2.1 Spin-dependent decay channels for various excitations in non-degenerate ground state π-conjugated polymers.[4]

Spin-dependent decay channels	
$p_f^+ + p_f^- \rightarrow S_1^* \rightarrow 1^1B_u + phonons \rightarrow S_0 + h\nu + phonons$	2.1
$p_f^+ + p_f^- \rightarrow T_1$	2.2
$p_t^+ + p_t^- \rightarrow S_0 + phonons$	2.3
$S_1^* + p_t^+ \rightarrow S_0 + p_t^+ + phonons$	2.4
$S_1^* + p_t^- \rightarrow S_0 + p_t^- + phonons$	2.5
$p_f^+ + p_f^+ \leftrightarrow bp^{++}$	2.6
$p_f^- + p_f^- \leftrightarrow bp^{--}$	2.7
$bp^{++} + p_f^- \rightarrow p_t^+$	2.8
$bp^{--} + p_f^+ \rightarrow p_t^-$	2.9
$T_1 + T_1 \rightarrow S_1^* \rightarrow S_0 + h\nu + phonons$	2.10
$T_1 + S_1^* \rightarrow T_1 + S_0 + phonons$	2.11

where:

p_f^x and p_t^x are free and trapped polarons, respectively

T_1 are triplet excitons

S_0 and S_1^* are the ground state and excited singlet states, respectively

1^1B_u is the lowest state in the singlet manifold

bp^{xx} are bipolarons

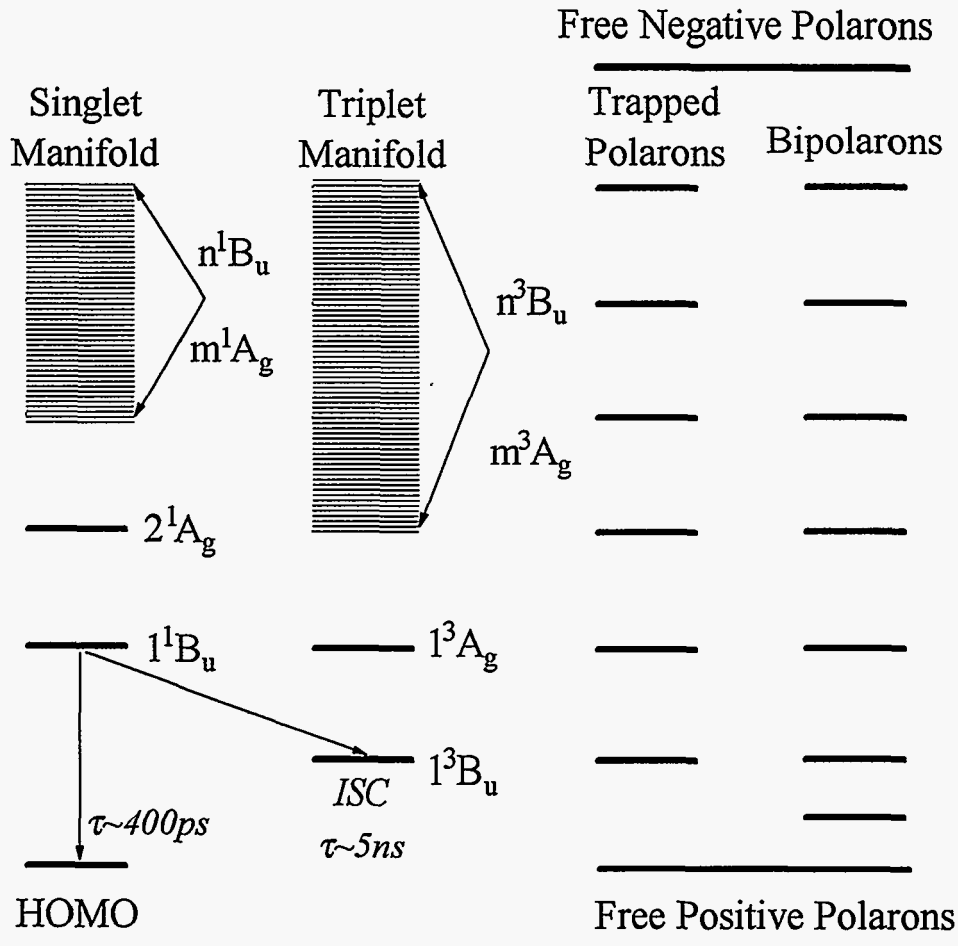

Figure 2.5 Schematic energy levels of singlet, triplet, trapped polaron, bipolaron manifolds in luminescent π-conjugated polymers.[7]

2.3 Types of π-conjugated Polymers

A wide variety of π-conjugated polymers have been synthesized.[45] A few of the polymers studied in this work are shown in Figure 2.6. Other polymers will be introduced when the results of measurements on them are presented below.

π-conjugated polymeric systems are bound by weak van der Waals interactions or by crosslinks. Unsubstituted polymers are insoluble and brittle, making them difficult to process. However, the addition of side groups separate the chains and weaken the crosslinking, leading to soluble, flexible, and processible polymers.

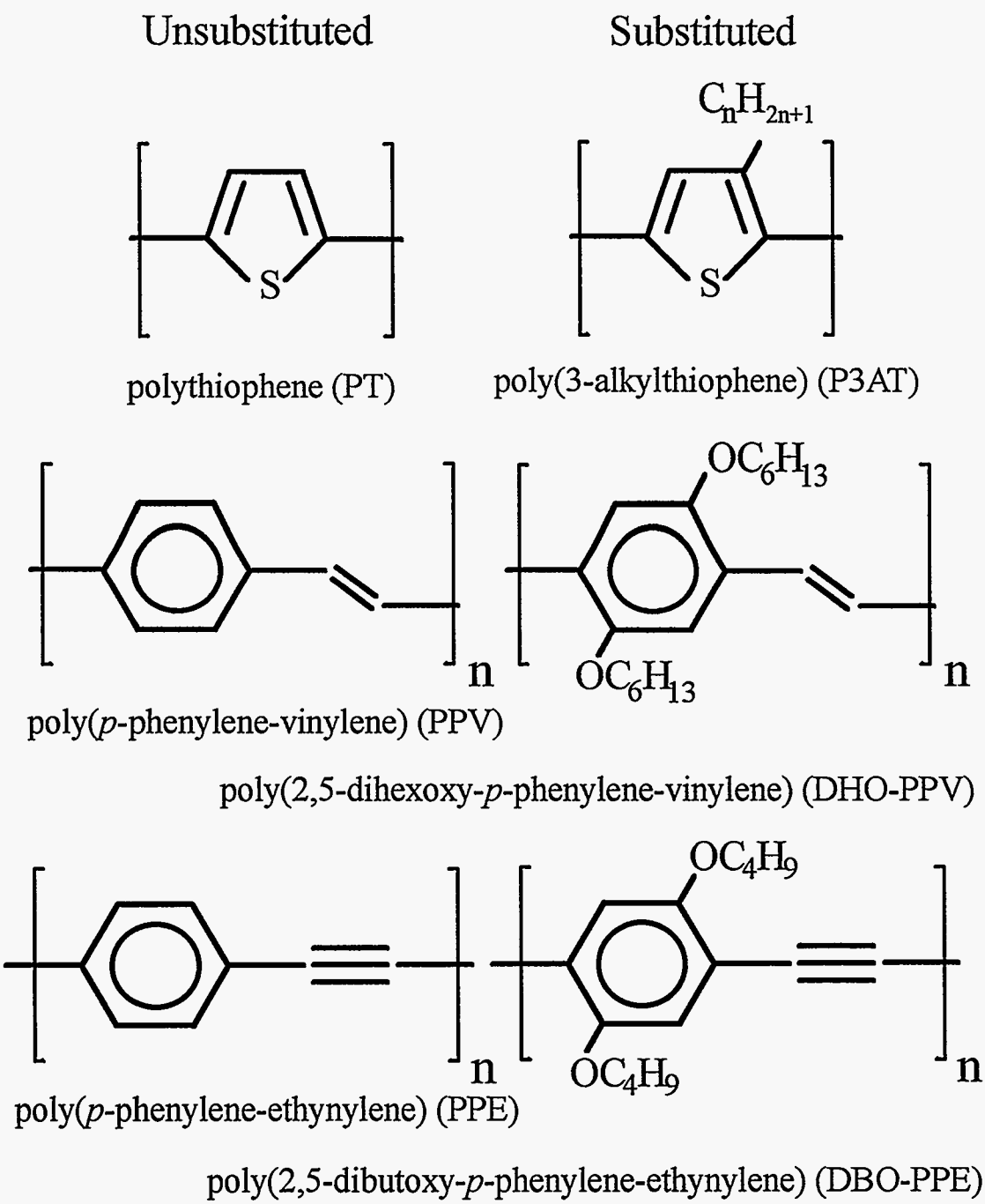

Figure 2.6 Chemical structure of unsubstituted and substituted π-conjugated polymers.

Polythiophene and its 3-alkyl derivatives are weakly nondegenerate ground state π-conjugated semiconducting polymers. They can be oxidatively doped to conductivities greater than 1000S/cm^2, exhibit nonlinear optical responses and are fairly stable in air.[46] PPV and its derivatives also demonstrate nonlinear optical properties. Recent work on the electroluminescent qualities of this polymer have spawned two companies dedicated to the commercialization of PPV devices. In addition, the fast photoinduced charge transfer from MEH-PPV to C_{60} has opened new avenues for photovoltaic devices and other applications.[47] PPE is found to have a higher yield and band gap than PPV, but has not been as heavily investigated. However, it is far less susceptible to oxidation than PPV, and therefore warrants additional studies.

2.4 PLDMR of π-conjugated Polymers

PLDMR measurements have provided signatures of polarons and triplet excitons (T_1) in a variety of PPVs, P3ATs, ladder-type PPPs (LPPPs), and other π-conjugated polymers.[48-53] A good overview of the results can be found in Reference 4. This condensed version, reproduced and slightly rewritten below, was submitted to the 1997 Society of Plastics Engineers Conference in Toronto, Canada.

This section reviews recent ODMR studies of the polaron resonance in PPVs and P3ATs, including UV-excited measurements which provide insight into the energy levels and dynamics of excitons, polarons and bipolarons. The results are consistent with the conclusions of other studies,[54,55] that besides generation of S_1^* states which relax to 1^1B_u, photoexcitation at $\lambda_{ex} \geq 458$ nm largely results in generation of trapped polarons and bound interchain and intrachain-interconjugation segment polaron pairs. Photoexcitation at short λ_{ex}, however, is suspected to generate free polarons which may fuse to either singlet or triplet excitons, bipolarons,[32,46,49-51] or decay to trapped polarons.

The photogenerated singlet excitons may decay by various mechanisms: (i) relaxation to the 1^1B_u, which then decays radiatively (Equation 2.1), (ii) nonradiative decay through quenching by polarons, bipolarons, or other electric-field-generating centers

(Equations 2.4, 2.5, 2.11),[56-59] (iii) intersystem crossing (ISC) to low-lying triplet excitons,[7,41,44,48] or (iv) possible fission to trapped interchain polaron pairs (Equation 2.12). The generation of the trapped polaron pairs is apparently induced either at segments of adjacent chains, in which case the pairs are interchain and equivalent to excimers, charge-transfer excitons (CTEs), or spatially indirect excitons,[54] or at conjugation defects such as sites which are close to an adjacent chain, sites adjacent to C_{60}^- counterions[53] and possibly cross-linking sites.

The earlier ODMR studies[7,14,46,48,53] did not distinguish between trapped and free polarons and suggested that the PL-enhancing polaron resonance obtained by visible excitation is due to magnetic resonance enhancement of polaron fusion to singlet excitons as seen in Equation 2.1. This interpretation, however, is problematic: As shown elsewhere[52] and below, the lifetime of the polaron pairs yielding the resonance is in the microsecond to millisecond range. Yet in PPVs and LPPPs the tail of the PL in this range is very weak.[60,61] In addition, other results indicate that the trapped polaron pairs generated by visible excitation, whose lifetime increases exponentially with their separation,[62] recombine nonradiatively.[54,63,64] The PL-enhancing resonance is therefore reassigned to the role of these polarons as quenching sites for excitons.[32,50-53,56-59] (Equation 2.2-2.3) An interesting variant of these processes[65] which should be considered is quenching of S_1^* by trapped polaron pairs which dissociates the pair to generate free polarons:

$$S_1^* + p_t^- + p_t^+ \rightarrow S_0 + p_f^- + p_f^+ + phonons \qquad 2.12$$

This mechanism may provide an elegant explanation for the photoconductive response of e.g., PPVs, at the absorption threshold.[66]

At short λ_{ex}, a PL-quenching polaron resonance emerges in the PPVs and P3ATs, similar to the EL-quenching resonance observed in LEDs[32,46,49-51] and consistent with the formation of free polarons which may fuse to spinless bipolarons, singlet, or triplet excitons. The gap between the absorption edge, which is the energy of the 1^1B_u, and the emergence of the PL-quenching resonance, is then equal to the 1^1B_u binding energy, *defined as the energy*

required to dissociate it to free polarons. This energy is measured to be ~0.8 eV in 2,5-dioctoxy-PPV (DOO-PPV) and poly(3-hexyl thiophene) (P3HT).[67]

Typical polaron resonance spectra of 2,5-dihexoxy PPV (DHO-PPV) and poly(3-hexyl thiophene) (P3HT) at various λ_{ex} are shown in Figure 2.7. As clearly seen, the polaron resonance is positive at λ_{ex} = 458 nm but in DHO-PPV it is weakly negative at λ_{ex} = 430 nm (2.88 eV), and its quenching intensity increases with decreasing λ_{ex}. In P3HT no resonance is detectable at λ_{ex} = 430 nm. This could also be due to the low available excitation intensity (~ 5 mW) (see above). At $353 < \lambda_{ex} < 406$ nm, however, a PL-quenching component could be observed in addition to the enhancing resonance. At λ_{ex} = 308 nm the quenching resonance is dominant and the PL-enhancing resonance is almost undetectable.

An interesting question arises as to the nature of the spin polarization of the polaron pairs off and on resonance. In order to observe an ODMR resulting from a spin-½ excitation, its spin-lattice relaxation time T_1 cannot be shorter than its lifetime τ.[68] At the same time, Frankevich et al.[55] and Yan et al.[54,69] suggest that the trapped polaron pairs are almost entirely geminate, which implies that their spin configuation is predominantly antiparallel. Frankevich[70] has also suggested that the decay rate of parallel pairs to triplet states is faster than the recombination rate of antiparallel pairs. Therefore, upon the net transfer of antiparallel pairs to parallel pairs at the resonant field, the overall lifetime of the polaron pairs is reduced, their steady-state population decreases, the rate at which singlet excitons are quenched nonradiatively decreases, and the PL increases. However, photoinduced absorption detected magnetic resonance (PADMR) studies of these polymers haven't indicated that the population of triplets increases at the spin-½ resonance.[71]

The alternative scenario assumes that the decay rate of parallel spin pairs is slower than that of antiparallel pairs, and that the PLDMR is due to a net population transfer from parallel to antiparallel spins among the long-lived nongeminate trapped pairs. In this scenario, the PL-enhancing resonance is unrelated to the geminate pairs. Although the density of nongeminate pairs is probably very low compared that of geminate pairs, the possibilities that it may be enhanced by either singlet quenching-induced dissociation (Eq. (4)) or by stepwise thermal dissociation[72] are interesting and deserve further attention.

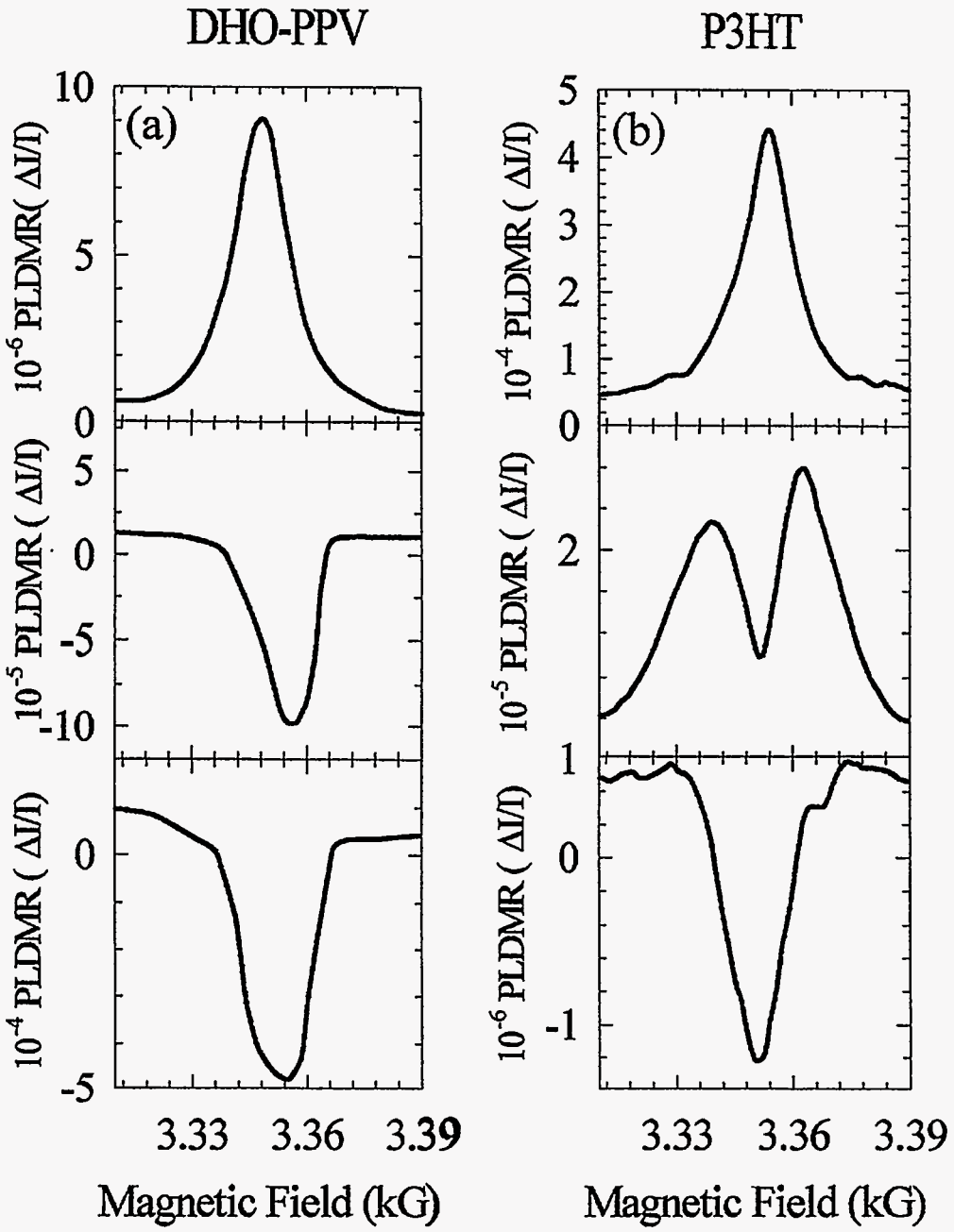

Figure 2.7 (a) DHO-PPV at (top to bottom) λ_{ex}=458, 430, and 406nm. (b) P3HT at (top to bottom) λ_{ex}=458, 353, and 308nm. Microwave power for all spectra was 1400mW except for the spectra taken at 458nm, at which it was 40mW. Temperature was set at 10K for all spectra.

The second scenario described above, in which the PL-enhancing polaron resonance is assigned to nongeminate trapped polaron pairs, implies that these pairs do not fuse to either singlet or triplet excitons. This conclusion is consistent with previous suggestions that they are interchain in nature.[32,51,52,54,64,69] However, the question of fusion of like-charged trapped polarons to bipolarons should also be addressed. If the source of the PL-quenching polaron resonance at short λ_{ex} is the spin-dependent generation of bipolarons (see below), then the results imply that these are usually not generated by trapped polarons. This is indeed consistent both with the interchain nature of the trapped polaron pairs and with recent results which suggest that the density of bipolarons generated by visible excitation is probably far lower than previously thought.[73]

In summary, the polaron photoluminescence (PL)-detected magnetic resonance (PLDMR) of poly(p-phenylene vinylenes) (PPVs) and poly(3-alkyl thiophenes) (P3ATs) at various excitation wavelengths λ_{ex} was reviewed. The PL-enhancing polaron resonance observed at long λ_{ex} was attributed to magnetic resonance enhancement of nonradiative recombination of trapped polaron pairs, which are nonradiative singlet exciton quenching centers. At λ_{ex} shorter than a threshold value, a PL-quenching polaron resonance appears in typical PPVs and P3ATs. This feature is suspected to result from magnetic resonance enhancement of bipolaron generation by intrachain fusion of like-charged free polarons, which are similar to the carriers which fuse to singlet excitons in the light-emitting diodes. The gap between the absorption edge, believed to be the energy of the radiative 1^1B_u singlet exciton, and the onset of the PL-quenching polaron resonance, is then a measure of the 1^1B_u binding energy, defined as the energy required to dissociate it into free polarons. This binding energy is found to be ~0.8 eV in both 2,5-dioctoxy-PPV and P3HT.

2.5 Introduction to C_{60} and C_{70}

The discovery of C_{60} and C_{70} launched a widespread and intense investigation into the properties of these novel carbon allotropes. The C_{60} and C_{70} molecules are shown in Figure 2.8. Two carbon-carbon bond lengths are found on the C_{60} structure, corresponding to

single (1.45Å) and double (1.40Å) carbon-carbon bonds. C_{60} and C_{70} both share the geodesic dome shape with 20 hexagons and 12 pentagons in C_{60} and 25 hexagons and 12 pentagons in C_{70}. Like ethylene, the carbon atoms in fullerene molecules are sp^2 hybridized with three C-C bonds and one p_z orbital. A number of methods have been used to probe these systems, including light-induced electron spin resonance (LESR),[74] photoluminescence detected magnetic resonance (PLDMR),[75] and absorption detected magnetic resonance (ADMR).[76] These three techniques have provided a wealth of information about the spin-dependent processes occurring in C_{60} and C_{70}. The initial PLDMR studies assigned the spin-½ resonance at g~2.0017 to enhanced polaron recombination which reduced the rate of quenching of singlet excitons by these polarons.[77] Recent time-resolved LESR measurements indicate that that resonance may actually result from a radical-triplet pair mechanism.[78]

2.6 PLDMR Studies of C_{60} and C_{70}

Films for PLDMR and ADMR are prepared in one of two ways: (i) evaporation, whereby the C_{60} or C_{70} is dissolved in a toluene solution and a film is formed when the toluene is allowed to evaporate under a vacuum. (ii) sublimation, whereby the C_{60} or C_{70} is heated and allowed to cool and crystallize on a substrate. The C_{60}:T/PS and C_{70}:T/PS were simply prepared by mixing polystyrene, toluene and C_{60} or C_{70} in the proper proportions and sealing in a quartz tube. The experimental setups are described elsewhere.[76-78]

The visibly-excited PLDMR spectra of C_{60} and C_{70} films are remarkably similar, both showing a central, spin-½ resonance and a number of full-field triplet signatures. The fluorescence detected magnetic resonance (FDMR) of C_{60}:T/PS and C_{70}:T/PS are similar but lack the spin-½ resonance observed in the films. In addition, C_{70}:T/PS exhibits phosphorescence.

Figure 2.9(a) shows the full-field PLDMR spectra of a C_{60} film. Note the shoulders occurring with a full width at half maximum (FWHM) of 250G and 640G. The 640G triplets are believed to be localized on a pentagon or hexagon and stabilized by coupling to a

bond on adjacent molecules, similar to the triplets observed in π-conjugated polymers (Chapter 4 below).

The same features are translated onto the C_{70} PLDMR spectra (Figure 2.9 (b)) as shoulders with 360G and 720G FWHM. Furthermore, the delocalized triplet is slightly narrower in C_{70} than in C_{60} probably due to the larger molecular size of C_{70}.

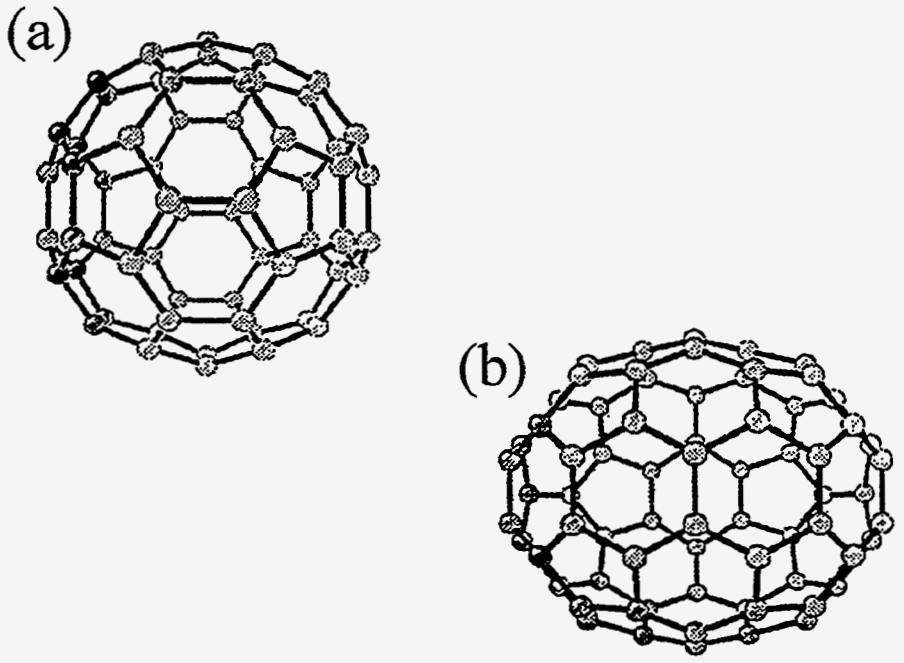

Figure 2.8 Diagrams of (a) C60 and (b) C70 molecules.

Photoexcitation of C_{60} films with visible light induces a reversal in sign of the spin polarization of the spin-½ radicals,[78] probably resulting from spin-selective quenching of triplet excitons, accounting for the results of Wei et al.[79] They observed that type (i) C_{60} films showed a spin-½ ADMR but type (ii) films, which were thought to have low native defect density, did not. The original PLDMR measurements[75] assigned the spin-½ resonance to polaron recombination. However, in light of the previous information, the PLDMR measurements and the LESR measurements could thus be explained by a radical-triplet pair mechanism.

Figure 2.10(a) shows the total PLDMR of C_{60}:T/PS. There is no spin-½ resonance for these isolated molecules. However, two triplet peaks, split by ~120G with shoulders separated by ~230G were seen. Calculation of the zero-field splitting parameters D and E[75] reveal that D~122G and E~9G, implying an axially symmetric triplet exciton delocalized over the entire molecule. Since the isolated molecules do not show the ~720G feature seen in films, it is believed that that pattern is due to a triplet localized on a face and stabilized by a neighboring molecule.[80] The fluorescence PLDMR (FDMR) (Figure 2.10(b)) and the phosphorescence PLDMR (PhDMR) (Fig 2.10(c)) of C_{70}:T/PS differ dramatically. The FDMR is ~200G wide with a central peak at g~2. Since the molecules are isolated, it not possible to explain these resonances in terms of a radical-triplet pair mechanism. Instead, the FDMR is attributed to ground-state repopulation.[81] The shape of the resonance and the amplitude of the g~2 peak can be described by a triplet exciton with zero-field splitting parameters of D~100G and E~D/3, i.e. an axially asymmetric triplet delocalized over the entire molecule.

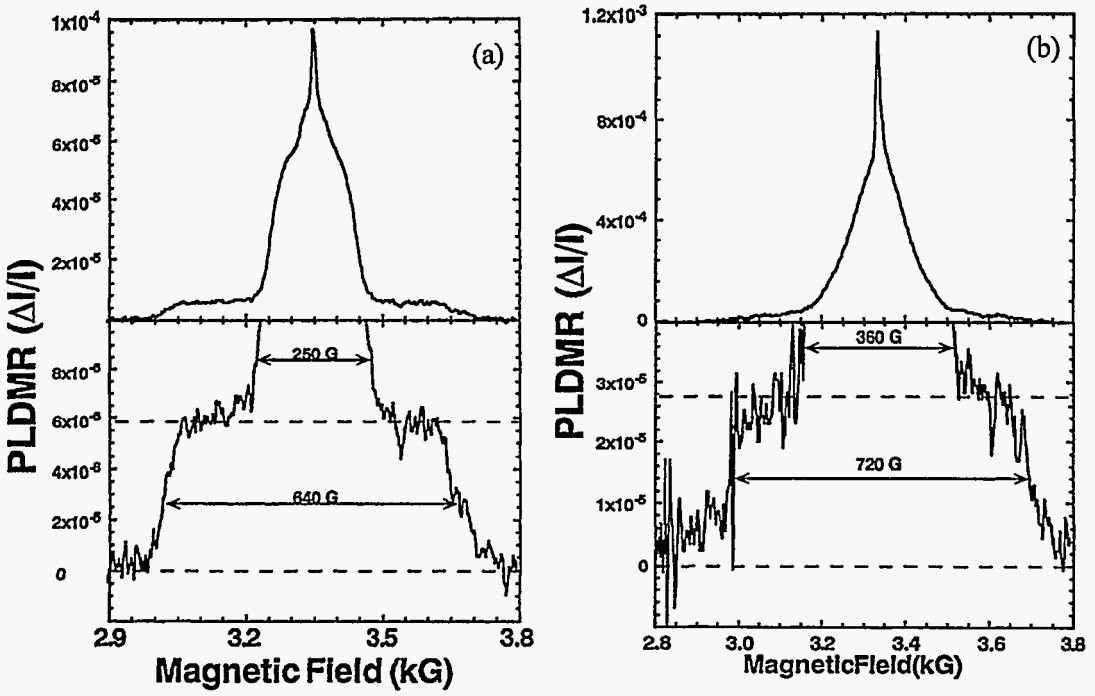

Figure 2.9 PLDMR full-field powder pattern of (a) C_{60} and (b) C_{70} film.[77]

The PhDMR of C_{70} glasses is due apparently to the direct radiative decay of the long-lived triplets. It is an order of magnitude more intense than the FDMR; its strong temperature dependence results apparently from a dynamic Jahn-Teller effect.[81]

2.7 Summary

The assignment of the spin-½ resonance in C_{60} and C_{70} films to radical-triplet pairs is consistent with the PLDMR and ADMR results. The two triplet resonances in the films are due to (i) triplets localized on a face adjacent to a neighboring molecule and (ii) triplets delocalized over the whole molecule. Triplet (i) is not observed in C_{60}:T/PS or C_{70}:T/PS. In frozen solutions of π-conjugated polymers the amplitude of triplets similarly localized on a phenyl ring[16] increases with increasing concentration. Since only long-lived (>0.1ms) processes can yield an observable PLDMR,[82] these tripets are believed to be stabilized by coupling with adjacent molecules.

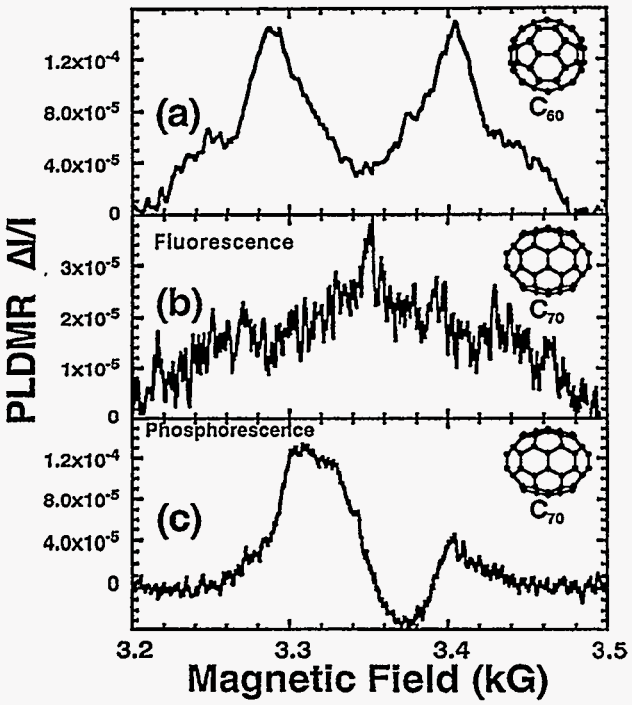

Figure 2.10 (a) The PLDMR of C_{60}:T/PS and of the (b) fluorescence and (c) phosphorescence of C_{70}:T/PS.[22]

CHAPTER 3. PLDMR MEASUREMENTS ON POLY(*P*-PHENYLENE)-TYPE LADDERPOLYMERS

This chapter describes the spin-½, spin-1 and lifetime PLDMR measurements on poly(*p*-phenylene)-type (PPP) ladderpolymers (LPPP) (Figure 3.1). In this chapter, we present evidence to suggest the presence of long-lived (20μs to 4ms) interchain and intrachain-inter(conjugation) segment trapped polaron pairs, which quench singlet excitons nonradiatively and recombine nonradiatively. To avoid confusion, the intrachain-inter(conjugation) segment polaron pairs will hereafter be called intersegment pairs.

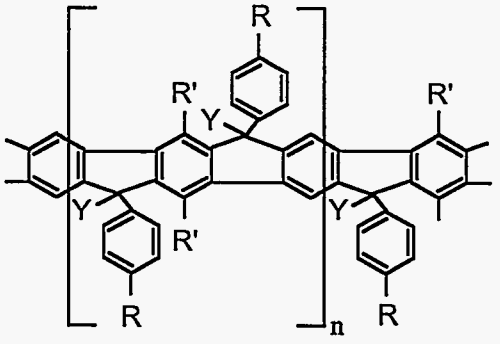

Figure 3.1 Chemical structure of m-LPPP, Y=CH_3, R=$C_{10}H_{21}$, R'=C_6H_{12}, n=52.

3.1 Introduction to LPPP

The class of ladder-type polymers is highly attractive for possible industrial applications such as LEDs and polymer lasers. Specifically, the high quantum yield (24% in films and 85% in solutions),[83] the structural regularity[84] and the solubility in nonpolar solvents are all indispensible for eventual marketability. In addition, the absence of competition between the stimulated emission and the photoinduced absorption[85] allow LPPP to be optically pumped. The synthesis[86] results in a planarization of neighboring phenyl rings and the suppression of twisting around inter-ring bonds. In addition, the conjugation length

of the polymer is expected to increase relative to PPP. Figure 3.2 shows the absorbance as well as the PL excitation and emission for m-LPPP film at room temperature. The PL exhibits a strong band around 550nm which is nearly temperature independent but weakens with decreasing concentration of m-LPPP in m-LPPP/poly(methyl methacrylate)(PMMA) blends. Since aggregation is known to occur in m-LPPPs[83,87] the cw PL spectrum is thought to be due to interband transitions, peaking at 465 and 490nm, and to a broad aggregate emission, peaking at 550nm.[85]

The work reported here focuses exclusively on m-LPPP, so named for the methyl substituent at the methin bridge (symbol Y in Figure 3.1). m-LPPP has the highest degree of order among the LPPPs.[85]

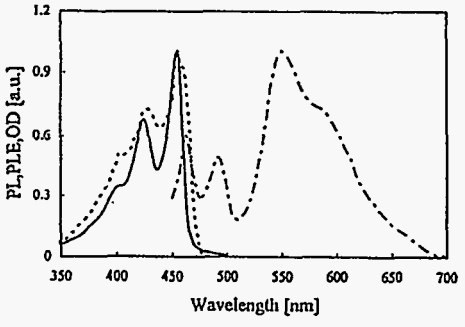

Figure 3.2 Optical density (OD, solid), photoluminescence emission (PL, dash-dotted, excitation at 390nm) and PL excitation (PLE, dotted, emission at 490nm)[85] of LPPP film at 300K.

3.2 LPPP Spin-½ Resonance

The m-LPPPs did not exhibit any observable PLDMR when excited at 360nm even though the PL was quite bright at that wavelength. However, excitation at 457.9nm resulted in the strong PL-enhancing resonances shown in Figure 3.3. The spin-½ resonances in a frozen toluene solution and in a film are shown in Figure 3.3. The lineshape can be fitted by two Gaussians or two Lorentzians split by 1.5±0.5G.[88] The full width at half

maximum (FWHM) for the Lorentzian fit of the solution's low- and high-field components are $\Delta H_{½}$~17 and 3.8G, respectively. In analogy with ESR, Lorentzian lineshapes are expected when the spin-½ particles are isolated and noninteracting. The Gaussian fits are most appropriate when the spins are close together and are dipolarly coupled. Lineshape fits on PPVs can also be accomplished by either two Gaussian or one Lorentzian curve.[48] However, the lineshape in P3AT could only be fit satisfactorially using two Gaussian curves.[40] The lineshapes for LPPP are analyzed using Lorentzian curves as they yield slightly better fits.

The lineshape of the resonance in the m-LPPP films is considerably broader than in the frozen solution (Figure 3.3). Table 3.1 summarizes some important linewidths for the solution and film.

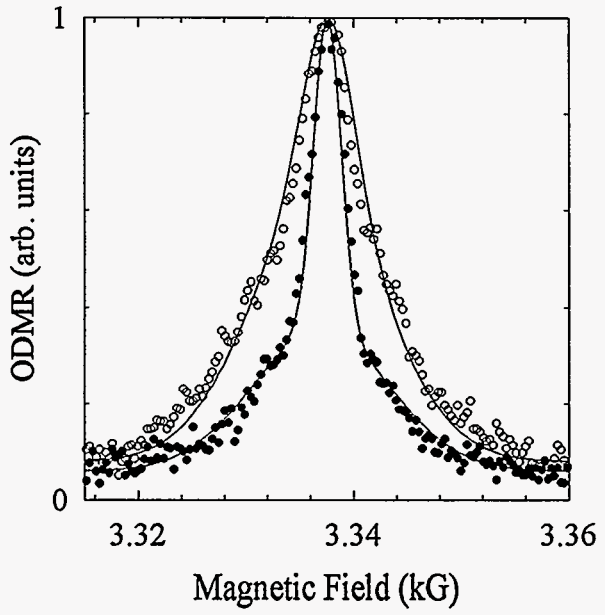

Figure 3.3 Narrow g=2 resonance for m-LPPP film (open circles) and solution (closed circles) at 20K.

The 5.1 and 25 G widths of the Lorentzian components in the film are broader than those of the frozen solution. In addition, the relative strength of the broader component is higher in the films. In the frozen solution, the ratio of the amplitudes of the broad-to-narrow components is only 0.2, but in the films it is 1.04. The decrease of the broad component in solution supports a picture in which the broad component is due to close interchain polaron pairs and the narrow component results from separated intersegment pairs. Note, however, that the linewidth of the narrow component decreases by 25% in solutions, whereas the broad component decreases by 32%. It is not clear why the intersegment pair resonance linewidth should decrease unless the solvent were playing a role in the chain morphology.

Perhaps the most appropriate fitting method would utilize a Gaussian for the broad component and a Lorentzian for the narrow component. The broad component occurs at a higher g-value than the narrow component, consistent with reported results on P3AT.[40,48]

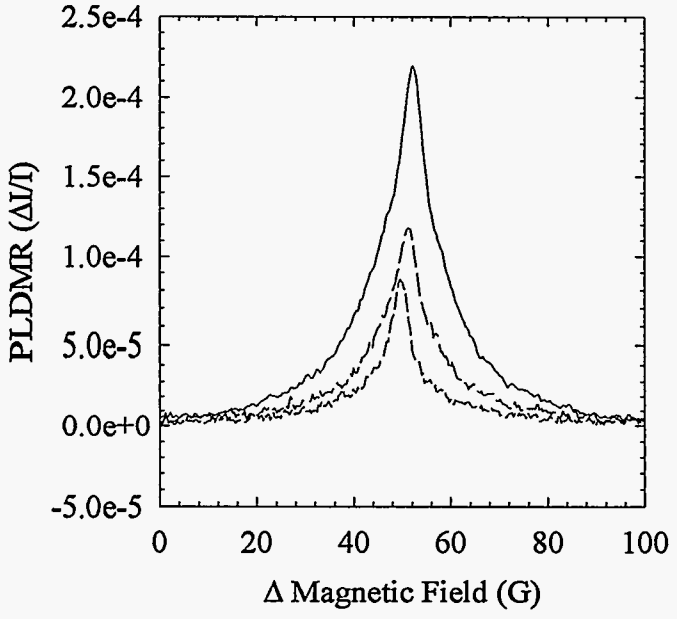

Figure 3.4 Narrow g=2 resonance for a m-LPPP film at 40, 203 and 811mW microwave power at 20K. Excitation by 18mW of the Ar^+ laser line at 457.9nm.

Table 3.1 Linewidths ($\Delta H^1_{1/2}, \Delta H^2_{1/2}$) of the broad and narrow component fits of m-LPPP films and solution spin-½ PLDMR; P denotes the microwave power.

Sample	P[mW]	$\Delta H^1_{1/2}[Gauss]$	$\Delta H^2_{1/2}[Gauss]$
Solution	811.0	17.0	3.8
Film	811.0	25.0	5.1
Film	203.0	22.0	4.0
Film	40.0	21.0	3.8

The microwave field can contribute to the width of the observed linewidth as shown in Figure 3.4 and by the fitting parameters in Table 3.1. In this case, the microwave field contributes only slightly to the linewidth at 811mW.

The PL (Figures 3.2, 3.5, 3.6 and 3.7) and the spectral dependence of the spin-½ PLDMR (Figures 3.5, 3.6 and 3.7) are corrected for detector response, but not for self-absorption. The emission from dilute m-LPPP solutions (λ_{ex}=457.9nm) is very different from that of the film, with successively weaker peaks at ~465, ~490, and ~540nm. Only the low-energy component of the 465nm peak is resolved due to its proximity to the λ_{ex}(Figure 3.5).

Figure 3.5 also shows that the spectral dependence of the PLDMR (sd-PLDMR) in frozen m-LPPP solution is identical to the PL, demonstrating that all of the emission bands contribute proportionally to the resonance. However, Figure 3.6 shows that the resonance is chiefly due to the aggregates, since the largest contribution to the sd-PLDMR is around 540nm. The films producing the emission and spectral dependence of the resonance shown in Figure 3.6, in which the contribution of aggregates is large, are referred to as Type I films.

The PL and sd-PLDMR of m-LPPP films, produced by another method which results in an aggregate-poor film, are shown in Figure 3.7. The PL is similar to that of the frozen solutions and is therefore suspected to be dominated by the decay of intersegment excitons. However, a weak aggregate signature is observable and it is sufficiently strong to yield a PLDMR as intense as that of the 490nm band.

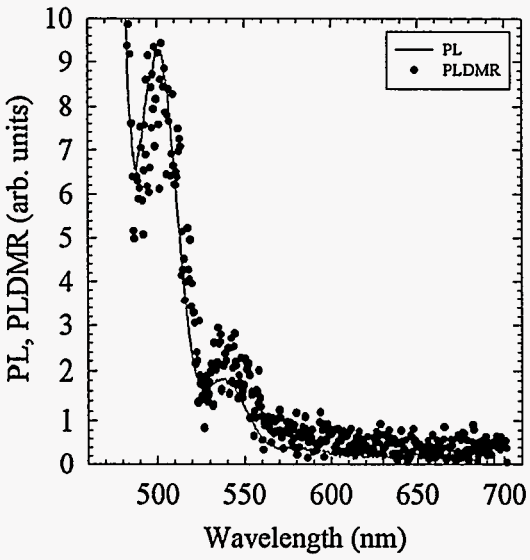

Figure 3.5 Spectral dependence of the g=2 PLDMR and the PL spectrum for a m-LPPP solution at 13K.

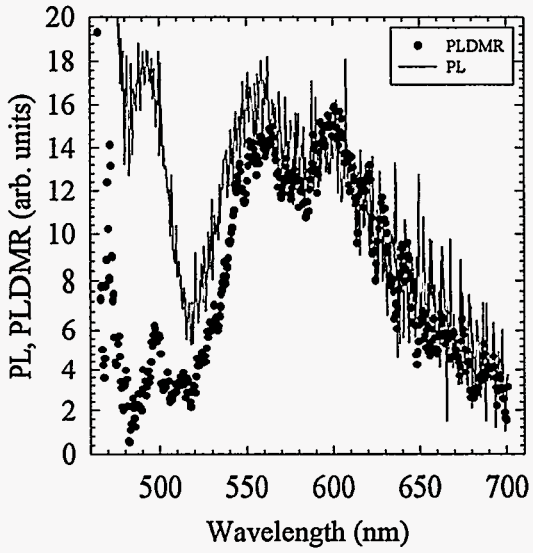

Figure 3.6 Spectral dependence of the g=2 PLDMR and the PL spectrum for a type I m-LPPP film at 20K.

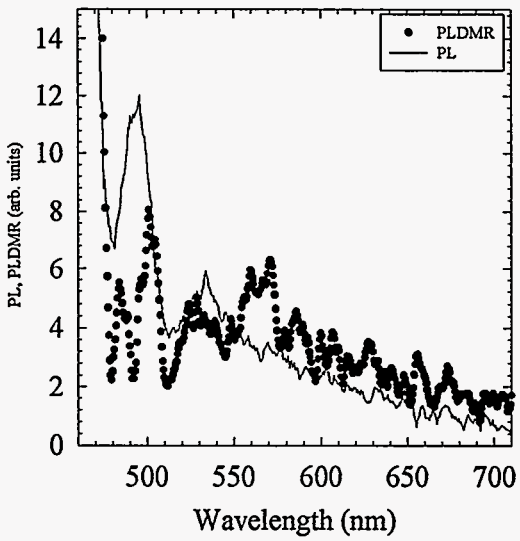

Figure 3.7 Spectral dependence of the g=2 PLDMR and the PL spectrum for a type II m-LPPP film at 20K.

The frequency-resolved ODMR (FRODMR) technique, outlined in Chapter 1, also provides new insight not only into the m-LPPPs but also into the basic photophysics of π-conjugated polymers. FRODMR will measure the lifetime of the process affecting the radiative recombination; it will not necessarily measure the lifetime of the radiative species. This is a key point in resolving the different polymer dynamic models. Figure 3.8 shows the dependence of the lock-in modulus, R on the microwave chopping frequency, f in a m-LPPP films at 20K. When R is determined by a single time constant τ, it is described by Equation 1.43. However, the observed behavior could not adequately be described by a single time constant, therefore, a second time constant was introduced:

$$\vec{R} = \frac{c_1 \exp[i \arctan(2\pi f\tau_1)]}{\sqrt{(1+(2\pi f\tau_1)^2)}} + \frac{c_2 \exp[i \arctan(2\pi f\tau_2)}{\sqrt{(1+(2\pi f\tau_2)^2)}} \qquad (3.1)$$

where the variables are the same as in Equation 1.43.

The complex notation is necessary since the lock-in phases of the contributions of the processes may not be equal. At the phase which maximizes the lock-in output, the output is given by the modulus of the vector **R**. The behavior of the modulus of Equation 3.1, with values τ_1 = 666μs, τ_2=39μs, and c1/c2 = 1.4, yields the solid lines in Figure 3.8. The dotted line results from a fit using Equation 1.43 with a single time constant. In both the films and frozen toluene solutions, the fit with a decay process characterized by a single lifetime τ is poor. However, there is good agreement with a model assuming two lifetimes. The lifetimes and amplitude ratios are summarized in Table 3.2. Note that the τ_i in the frozen solutions are much longer than in the films. The larger contribution of the longer τ_i is also consistent with its assignment to intersegment pairs on the same chain.

Thomas et al.[62] have shown that the recombination rate of a P^+-P^- pair should be given by the equation:

$$\tau^{-1} = \tau_0^{-1} e^{-2r/a} \tag{3.2}$$

where:

τ_0^{-1} is the maximum recombination rate

r is the interpair separation

a is the Bohr radius of the polaron

Therefore, the polaron PLDMR in both films and solutions must be due to the recombination of *at least* two different species with different r/a ratios. A distribution of lifetimes around a single value may exist but is unlikely in view of the widely different values of τ_1 and τ_2. The observed behavior is consistent with an assignment of the shorter- and longer-lived components to interchain and intersegment polaron pairs, respectively. In particular, the lifetimes are longer in the frozen solutions, as would be expected from a larger separation between the polarons. However, we would expect one of the lifetimes, that of the intersegment pairs, to remain largely unchanged since the solution should not affect those pairs drastically. While this observation is not clearly understood, it may result from the effects of the solvent on the conformations of the chains.

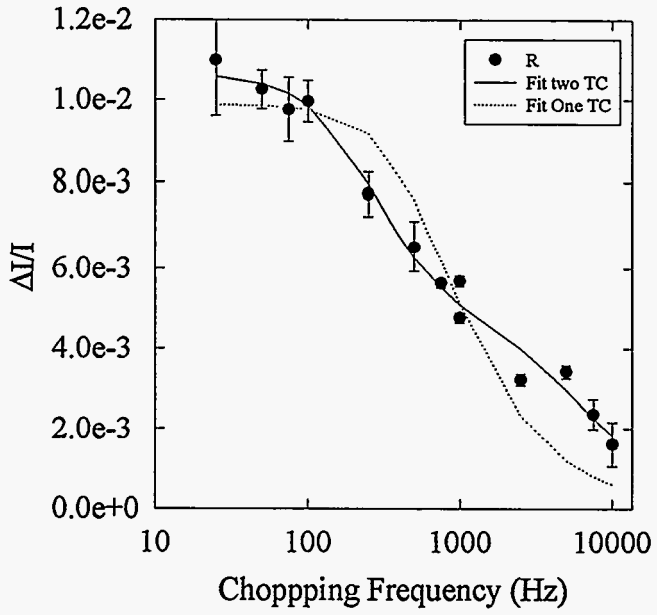

Figure 3.8 Modulus of the g=2 PLDMR signal of a m-LPPP film at 20K.

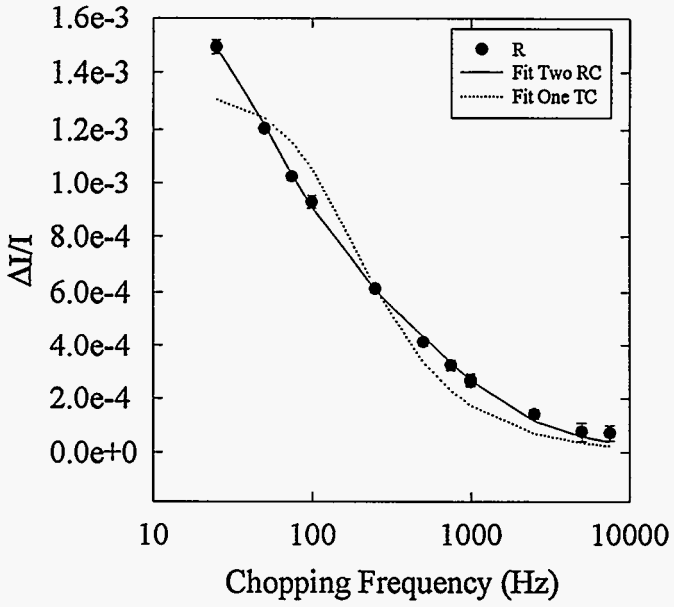

Figure 3.9 Modulus of the g=2 PLDMR signal of a m-LPPP solution at 20K.

Table 3.2 τ_i and c_1/c_2 for m-LPPP film and solution.

Sample	τ_1 (μs)	τ_2 (μs)	c_1/c_2
Film	39.0	666.0	1.4
Solution	365.0	3,280.0	2.1

If the r/a ratio for the fastest process is set to unity, the values of τ_i in the other cases yield the values of r/a given in Table 3.3. Note the high sensitivity of τ to r/a. These results are consistent with the assignment of the resonance to interchain and intersegment polaron pairs.

Table 3.3 Interpair separation to Bohr radius ratios (r/a) for the different polaron lifetimes in m-LPPP solution and film.

Sample	Lifetime (μs)	r/a	Polaron Location
Film	39.0	1.0	interchain
Film	666.0	2.4	intersegment
Solution	365.0	2.1	interchain
Solution	3,280.0	3.2	intersegment

The separation of the closer interchain pairs in solution is larger than that in the films by a factor of 2.1, obviously due to the distance provided by the solvent. The separation of the intersegment pairs on the same chain increased by only 33%. As with the linewidth, this effect may be due to solvent interactions with the polymer.

3.3 LPPP Spin-1 Resonance

The full-field S=1 triplet PLDMR of a m-LPPP film at 10K and room temperature is shown in Figure 3.10. The structure of the full-field triplet pattern at 10K enables the

determination of the zero-field splitting parameters (zfs) as described in Chapter 1.3 (Equations 1.21-1.23). The half-field pattern (Figure 3.11) parameters can be determined via Equations 1.24 and 1.25. Using the locations of the steps (Equation 1.27) in Figure 3.10 gives $D/g\beta$=630G. Therefore, using Equation 1.26, the upper bound of the spacial extent of the triplet is approximately r_{ub}~3.5Å. This result is slightly larger than those calculated on P3ATs[48] and PPVs[40] (note those calculations missed a factor of the cube root of 2 compared to Equation 1.26). In all of these cases, the triplet does not extend much beyond the width of a phenylene or thiophene ring. The shape the pattern in Figure 3.10 is characterized by (i) a single broad singularity at the center which is superimposed on the narrow polaron resonance and (ii) shoulders which occur at the step locations. Therefore, E~D/3, implying a triplet state devoid of any axial symmetry. Calculations based on the half-field pattern agree with the full-field results.

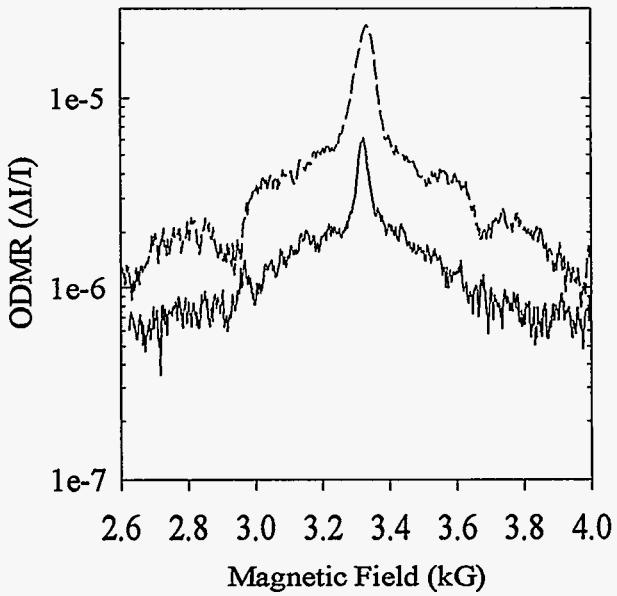

Figure 3.10 m-LPPP film triplet powder pattern at 10K (upper curve) and 300K (lower curve).

The amplitude of the triplet in the solution is ~$2x10^{-6}$ (Figure 3.12) and in the film is ~$4x10^{-6}$, so there is a 50% amplitude reduction from the film to the most concentrated solution. Therefore, the triplet state must be either an interchain excitation or intrachain excitation stabilized by a neighboring chain. We will present evidence in the next chapter that the latter scenerio is the more plausible.

3.4 Discussion

The PL-enhancing polaron resonance observed by excitation of the P3ATs, PPVs and PPEs at $\lambda_{ex} > 458$nm was initially assigned to magnetic resonance enhancement of P^+-P^- fusion to singlet excitons (Equation 2.1). As mentioned in Chapter 2, the long-lived PL of PPVs at $\tau > 10$ns is completely negligible, whereas the lifetime of the antiparallel spin polaron pairs which are responsible for the PLDMR is longer than 10μs. Therefore, we believe that these trapped polaron pairs are responsible (Equation 2.4 and 2.5) for quenching singlet excitons. All of our data is consistent with this conclusion.

The triplet resonance was previously assigned to magnetic resonance enhancement of triplet-triplet fusion to singlets. However, the absence of any delayed fluorescence in m-LPPP rules out this mechanism. Therefore, the resonance possibly occurs due to (i) enhanced nonradiative decay of triplets which reduces the rate at which they quench singlets (Equation 2.11) and/or (ii) ground state repopulation. The first possibility assumes that triplets quench radiative singlets as do polarons. The reduction of the triplet population via magnetic resonance enhancement of their nonradiative decay would increase the PL. The second possibility requires the triplets, which are electrons excited into S=1 states in the molecular exciton picture, to cause a small depopulation of the ground state which in turn decreases the PL. Repopulation of the ground state via magnetic resonance enhancement will lead to a positive PLDMR signal. We note that the second possibility is the only plausible mechanism which can account for the PLDMR of nonphosphorescent tripets in matrix-isolated C_{60} and C_{70}.[77]

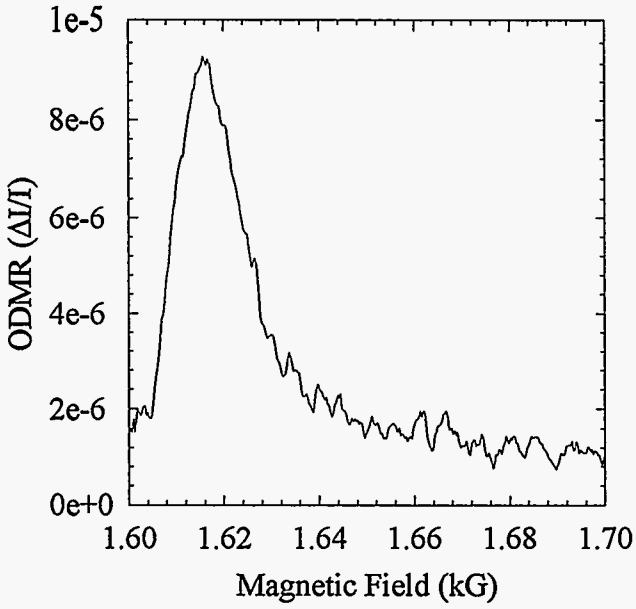

Figure 3.11 m-LPPP film half-field triplet powder pattern at 10K.

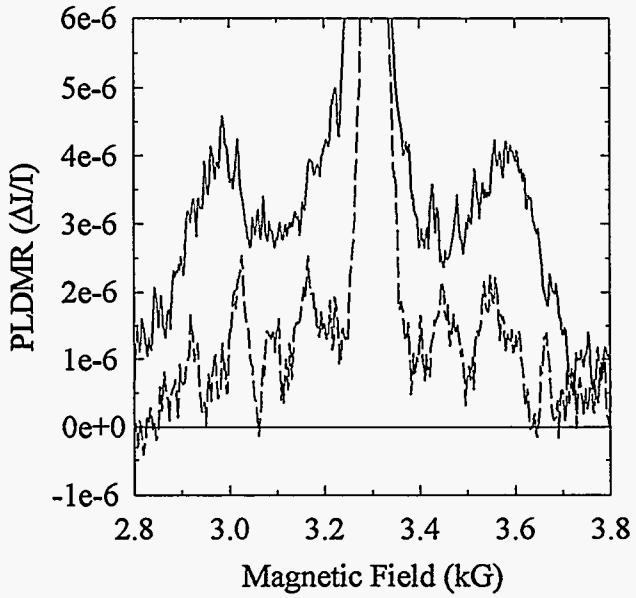

3.12 m-LPPP triplet in film (upper curve) and solution (lower curve) at 10 and 20K, respectively.

The time constants in Table 3.2 should be compared to the photoinduced absorption (PA) of LPPP films.[89] The PA measurements yielded a dominant long-lived component and a faster component with a lifetime of ~1ms. If that faster PA lifetime is due to the same mechanism as the ~670μs lifetime polaron PLDMR, then the shorter-lived polaron PLDMR is unaccountable by PA. This issue remains unresolved.

Furthermore, the photomodulation spectrum of m-LPPP also exhibits a band due to triplet-triplet transitions[90,91] at both low and room temperatures. This triplet is tentatively assigned to the triplets which result in the full- and half-field transitions shown in Figures 3.10 and 3.11.

The PLDMR of the LPPPs should also be compared to the PLDMR and electrically detected magnetic resonance (EDMR) of poly(phenyl phenylene vinylene) (PPPV).[92] In these polymers it was also observed that the resonances come mainly from the low-energy emission bands. Due to the relaxation of slowly recombining polaron pairs, the delayed emission was predicted[93] and observed[94] to shift to lower emission energies. Thus, Dyakonov et al.[92] concluded that only the delayed recombination of distant polarons is influenced by magnetic resonance conditions. They suggested, however, that the PLDMR is due to spin-dependent radiative recombination of these polaron pairs. Yet the results on the LPPPs demonstrate that the lifetimes of the polaron pairs which yield the PLDMR are 40 to 3300μs while those of the interchain polaron pairs or charge transfer excitons (CTEs) which yield the aggregate emission is 855ps.[95] In addition, the modulation frequency measurements shown in Figures 3.8 and 3.9 are consistent with an indirect, and therefore non-radiative, process (Chapter 1.11 and 1.12). The longer lifetimes of the PLDMR producing polaron pairs suggests that the polaron separation is much higher than those yielding the aggregate emission (Equation 3.2). The results on LPPPs thus provide strong evidence that the PL-enhancing spin-½ PLDMR is due to very slow nonradiative recombination of distant polaron pairs, which eliminates their contribution to the quenching of otherwise radiative singlet excitons.

3.5 Conclusion

The recombination pathways of the photoexcitations in a poly(*p*-phenylene)-type ladderpolymer is influenced via singlet and triplet magnetic resonances. The triplets were found in both films and solutions and are assigned to the recombination of triplet excitons of ~3-4Å diameter. The intensity of the triplet in solution is half as intense as the triplet in the film, indicating some kind of interchain effect. This effect results from the stabilization of the triplet by units of adjacent chains.

Spin-½ resonances are observed in polymer films and solutions and assigned to the recombination of both interchain and intersegment polaron pairs. This assignment is supported by the lifetimes of the observed recombining species and the relative intensities of the double Lorentzian peaks describing the resonance curves. The lifetimes of the resonances in the films are shorter by an order of magnitude compared to the solutions. In addition, the broad resonance peak, assigned to interchain pairs, becomes dominant in the films. In solid samples, the presence of aggregate photoluminescence gives rise to a much higher magnetic resonance effect than the photoluminescence of the isolated chains observed in solutions.

CHAPTER 4. PLDMR MEASUREMENTS ON POLY(*P*-PHENYLENE ETHYNYLENE)

This chapter describes the spin-½, spin-1 and lifetime PLDMR measurements on 2,5-dibutoxy poly(*p*-phenylene ethynylene) (DBO-PPE) (Figure 4.1). In this chapter we present evidence to suggest that this PPE, supplied by Y.W. Ding,[96] is a colloidal system. The presence of long-lived interchain and intersegment trapped polaron pairs is indicated. However, their relative strength with respect to each other remains almost unchanged between the film and solution.

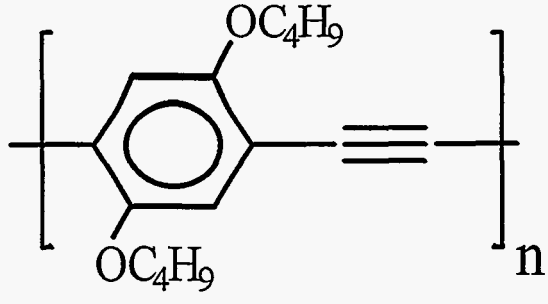

Figure 4.1 Chemical structure of PPE. n is between 25 and 53.[96]

4.1 Introduction to PPE

The PPE-class of π-conjugated polymers have many desirable properties useful for producing devices. However, their potential has not yet been realized due to accompanying problems. The PL yield is comparable to that of PPV[96] and the gap is ~2.7eV. The presence of an ethynylene unit between the benzene rings implies that PPE should be very rigid and possibly well-ordered. The π-electron orbitals are cylindrical (see Figure 2.2) and therefore the mean conjugation lengths are expected to be fairly long.[97] However, the PL (Figure 4.2) spectra is broad with only weak phonon peaks. In addition, the PLDMR spectra[16] is inhomogeneously broadened indicating a large degree of disorder. However, the broad

spectra may be due to smearing of the phonon bands due to single, double, and triple carbon-carbon bond stretch modes. Finally, some of the evidence from this work indicates that DBO-PPE is not actually soluble in the strictest use of that term. In fact, it appears that DBO-PPE solutions might actually be colloidal systems.

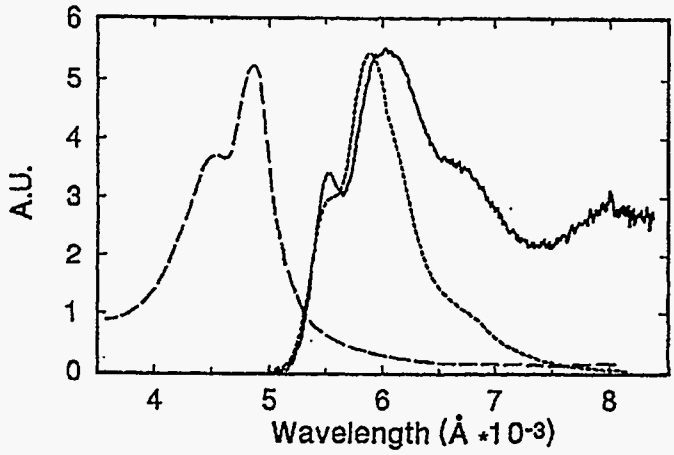

Figure 4.2 The optical absorption (dashed line), photoluminescence (dotted line) and electroluminescence (solid line) of 2,5-dihexoxy poly(p-phenylene ethynylene) (DHOPPE).[98]

4.2 PPE Spin-½ PLDMR

The PPEs were previously studied at various excitation wavelengths from 488 to 308 nm.[99] Unlike in DHO-PPV and P3HT (Figure 2.7), no emergence of a quenching resonance was seen. All of the work in this chapter was carried out at 488nm.

Figure 4.3 shows the spin-½ resonances of the frozen toluene solutions and films. The powder lineshapes are fit to the sum of two Gaussians split by 1.4 G with the broad component at the high-field. The FWHM for the Gaussians are shown in Table 4.1. Unlike the m-LPPPs which showed strikingly different resonances for the film and solution (Figure 3.3), the resonances from the DBOPPE solution and film are almost identical. This provides evidence that the PPE is forming small colloidal balls in solution, leaving the interchain and intersegment interactions largely unchanged. It should be noted that the amplitude of the

broad component does decrease slightly with respect to the narrow component from the films to the solutions. However, this effect is dramatic in m-LPPP. Also contrary to m-LPPP, the linewidths of the Gaussian components are very similar in the films and solutions (Table 4.1).

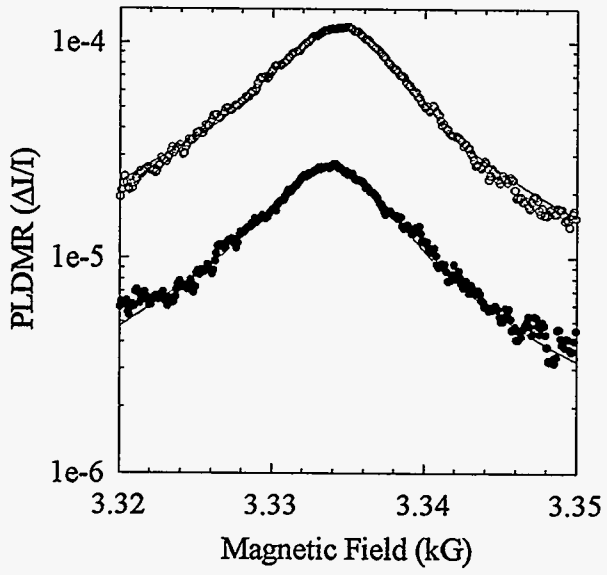

Figure 4.3 Narrow g=2 resonance for PPE film (open circles) and solution (closed circles) at 15K.

Table 4.1 Linewidths ($\Delta H^1_{1/2}, \Delta H^2_{1/2}$) of the broad and narrow component fits of PPE film and spin-½ PLDMR; P denotes the microwave power.

Sample	P[mW]	$\Delta H^1_{1/2}[Gauss]$	$\Delta H^2_{1/2}[Gauss]$	$\frac{\Delta H^2_{1/2}}{\Delta H^1_{1/2}}$
Solution	40.0	18.0	7.0	1.7
Film	40.0	20.0	7.5	1.4

The microwave power dependence of PPE is shown in Figure 4.4. The resonance at 811mW is broadened with respect to the resonance at 40mW by ~ 4 Gauss. The lineshape is unchanged.

The most remarkable result from the DBO-PPE PLDMR studies are the concentration-dependent measurements (Figures 4.5 and 4.6). The amplitude of the PLDMR resonance decreases by a factor of 2 when the PPE is diluted to 0.5 mg/ml. A further, rapid, decrease is noted when diluted to 0.27 mg/ml. However, further dilution to 0.09 mg/ml had very little effect. As noted previously, the lineshapes are unchanged within the resolution of these measurements. Therefore, whatever interactions are occuring in the powder continue in the solutions, albeit more weakly. Figure 4.6 shows a plot of the PLDMR vs. concentration. From the sparse data points, it appears that the PLDMR decreases with decreasing concentration until a critical point is reached.

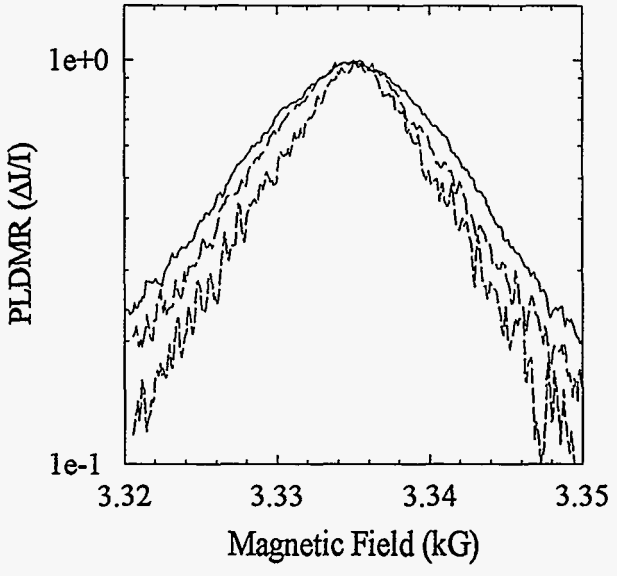

Figure 4.4 Narrow g=2 resonance for PPE powder at 811, 203 and 40mW microwave power (top, middle and bottom curve, respectively). Excitation by 20mW of 488nm laser line at 19K.

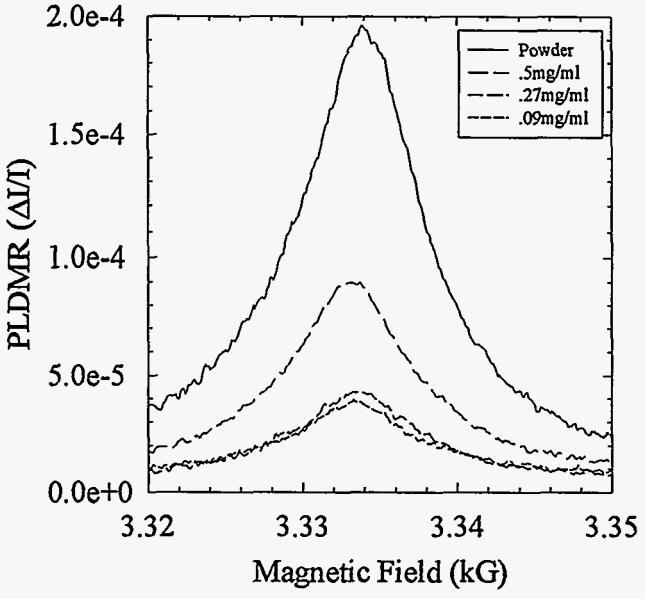

Figure 4.5 The spin-½ PLDMR in powder and frozen solutions of selected concentrations of DBO-PPE.

Thereafter, the resonance does not decrease significantly. These results are borne out in the triplet resonance, discussed below. The constant PLDMR with very dilute concentrations provide further evidence of colloid formation.

The FRODMR measurements, used to find the lifetime of the spin species affected by the resonance conditions, provides information very similar to that of m-LPPP. Figures 4.7 and 4.8 show these measurements from DBO-PPE powder and 0.5 mg/ml solution. The curves are fits of Equations 1.43 and 3.1. The fit to one time constant is unacceptable, but the fit to two time constants, for a total of four variables, must be viewed with healthy suspicion. Changing the initial conditions of the fit can lead to wildly divergent results. The qualitative difference between the powder and solution is unmistakable.

The overall processes are much slower in the solution (Table 4.2), probably due to increased polaron separation or solvent interactions. However, increased polaron separation should lead a narrower lineshape, an effect not noted in DBO-PPE.

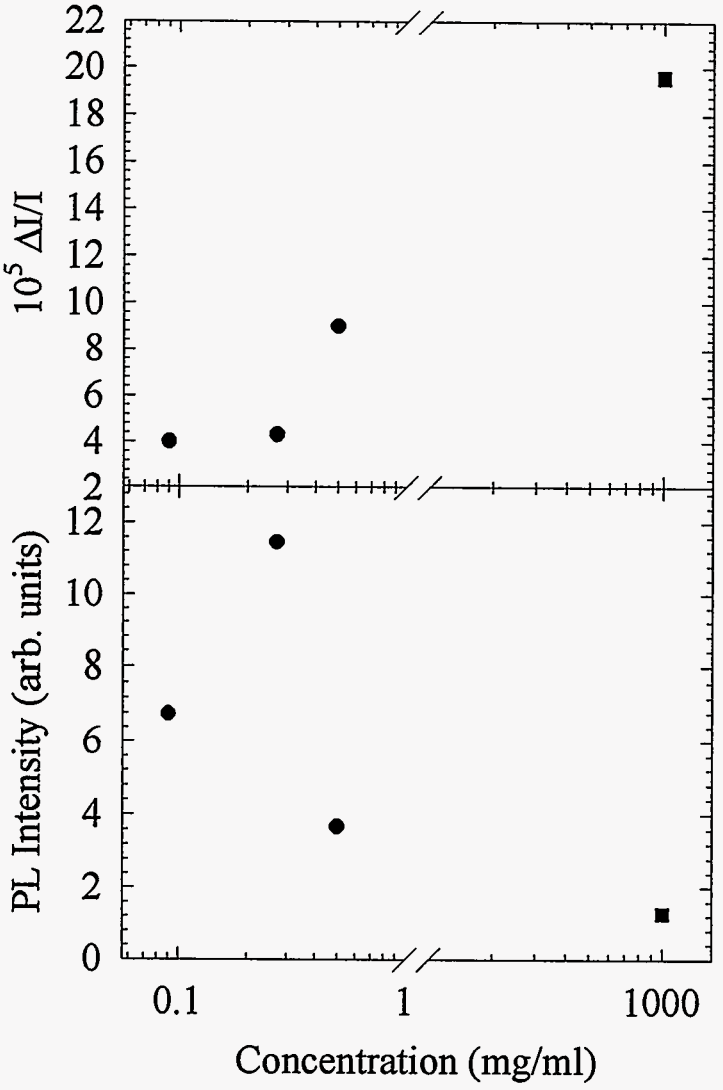

Figure 4.6 The amplitude ΔI/I of the g=2 resonance and the PL intensity I vs. concentration of DBO-PPE in toluene at 15K. The values for DBO-PPE powder are shown at the equivalent concentration of 1000mg/ml.

Lifetime measurements taken at two different microwave powers (Figure 4.9) are also illuminating. The fit to one time constant is poor (τ_{400mW}=26μs, τ_{40mW}=34μs) but it tells us that the dominant lifetime is longer at lower powers. At higher microwave photon density, the polaron pairs, which are quenching the excitonic recombination, are removed from the system at a greater rate. Therefore, the steady state resonance population of polaron pairs is reached more rapidly resulting in a quicker increase in the PL. The lifetime measured by FRODMR is expected to decrease with increasing power. The double τ fits, however, tell a contradictory story. The fast lifetime (interchain) decreases (Table 4.2) as its amplitude increases, but the slow lifetime (intersegment) decreases as its amplitude decreases. The microwaves may possibly be enhancing the interchain recombination at the expense of the intersegment recombination, but the vagaries of the curve fitting process prevent definitive answers.

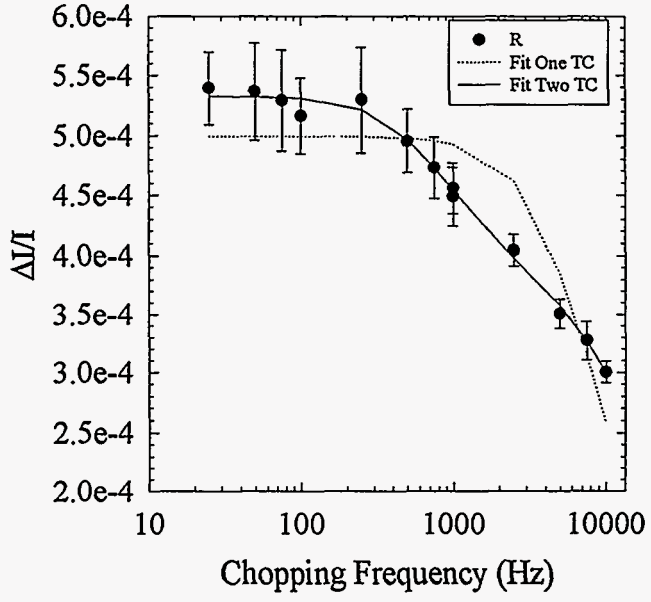

Figure 4.7 Modulus of the g=2 PLDMR signal of DBO-PPE powder at 15K.

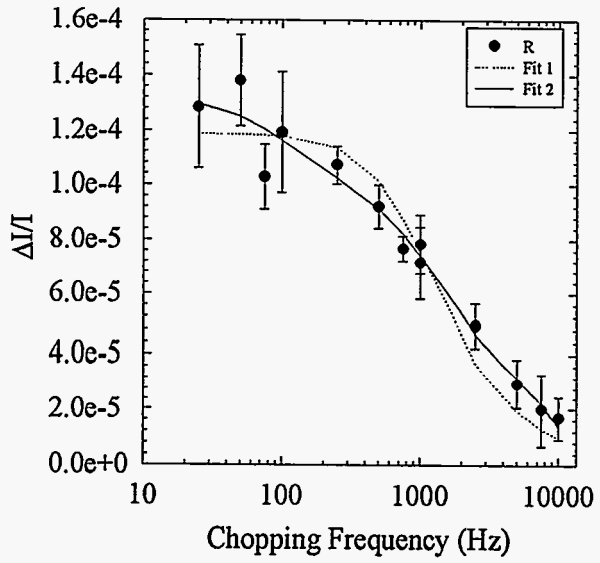

Figure 4.8 Modulus of the g=2 PLDMR signal of DBO-PPE frozen solution at 15K.

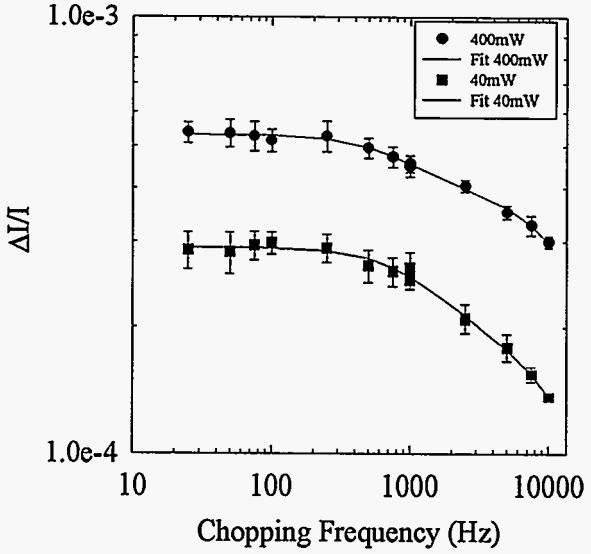

Figure 4.9 Modulus of the g=2 PLDMR signal of DBO-PPE powder at 408 and 40 mW microwave power.

Table 4.2 Lifetime, amplitude and interpair separation to Bohr radius ratios (r/a) for the different polaron lifetimes in DBOPPE solution and films.

Sample	Power	Lifetime(μs)	A_F/A_S	r/a	Polaron Location
Film	40mW	16.0		1.1	interchain
Film	40mW	190.0	1.7	2.4	intersegment
Film	400mW	12.0		1.0	interchain
Film	400mW	238.0	2.0	2.5	intersegment
Solution	400mW	152.0		2.3	interchain
Solution	400mW	2,145.0	2.5	3.6	intersegment

4.3 PPE Spin-1 PLDMR

The triplet state in conducting polymers may be the most prolific of states generated by the fusion of positive and negative carriers in π-conjugated polymer light-emitting diodes (LEDs)[100] but it is only poorly understood. The 25% theoretical upper limit of the electroluminescence (EL) quantum efficiency of the LEDs is derived from spin statistics, which should yield nonluminescent triplets in 75% of these fusion events. Triplet states are directly observed, albeit weakly, in biased polymer LEDs by EL- and conductivity-detected magnetic resonance.[32,48,98] The identification of these triplets with the ubiquitous states due to spin statistics is strongly suspected[32] but not firmly established. Therefore, a basic understanding of the behavior of the triplet states is highly desirable.

In this section we describe the triplet photoluminescence (PL)-detected magnetic resonance (PLDMR) in powders and solutions of 2,5-dibutoxy derivative of poly(p-phenylene ethynylene (PPE)) (DBO-PPE) (Figure 4.1). While the relatively rigid structure of the PPEs suggest that they should also be well-ordered,[101] their relatively broad and structureless PLDMR is actually consistent with considerable disorder.[47] A comparison of the triplet PLDMR of frozen toluene solutions of these polymers, described in this section, provides considerable insight into the nature of the triplet states.

In the frozen DBO-PPE solutions at 15K the amplitude $\Delta I/I$ (i.e., the fractional change in the PL intensity I at the resonant field) decreases rapidly with decreasing concentration, from ~$1.4 \cdot 10^{-5}$ in saturated solutions to ~$6 \cdot 10^{-6}$ in very dilute solutions. The results strongly suggest that the resonance is largely due to a long-lived (~30 μs in DBO-PPE films) triplet state localized on a phenylene ring and stabilized by coupling to a segment of an adjacent chain. The nature of the sites which yield the remnant triplet resonance observed in the very dilute DBO-PPE solutions is also discussed.

The full-field triplet resonance of powder and frozen toluene solutions of selected concentrations of DBO-PPE at T=15 K are shown in Figure 4.10. The full-field triplet pattern is ~1200 G wide in the powder, reflecting a localized triplet state whose extent has an upper bound of approximately 3.6Å or slightly larger than the size of a phenylene ring.[102-103] Note that the patterns are significantly broader than in m-LPPPs, suggesting that the extent of the triplet state is smaller in the PPEs. In addition, in the PPEs the patterns have gradually sloping wings which likely result from a wide distribution of D and E values.

The shapes of the triplet patterns observed in the frozen toluene solutions are identical to that of the powder. Figure 4.11 shows that as the concentration of PPE increases from the very dilute limit, $\Delta I/I$ remains constant until a concentration of ~0.09 mg/ml is reached. Above this concentration, $\Delta I/I$ increases up to the saturation concentration. The value of $\Delta I/I$ in the powder is ~50% higher than in the saturated solution. Figure 4.11 shows that the dependence of the total PL intensity I is qualitatively different from that of $\Delta I/I$, peaking at a concentration of ~0.27 mg/ml.

Due to the relative weakness of the triplet resonance, the lifetime τ, of the triplet state in PPE films determined by measuring the dependence of $\Delta I/I$ on the microwave chopping frequency ν_c could only be roughly estimated. Figure 4.12 shows the behavior of R vs ν_c at T=15 K. The solid line is the behavior of Equation 1.43 with $\tau = 30$ μs. The observed behavior is consistent with a nonradiative process with a distribution of lifetimes around this single value of τ.[104] However, an improved signal-to-noise may reveal a behavior requiring two values of τ, as for the narrow spin-½ resonance (Figure 4.7).

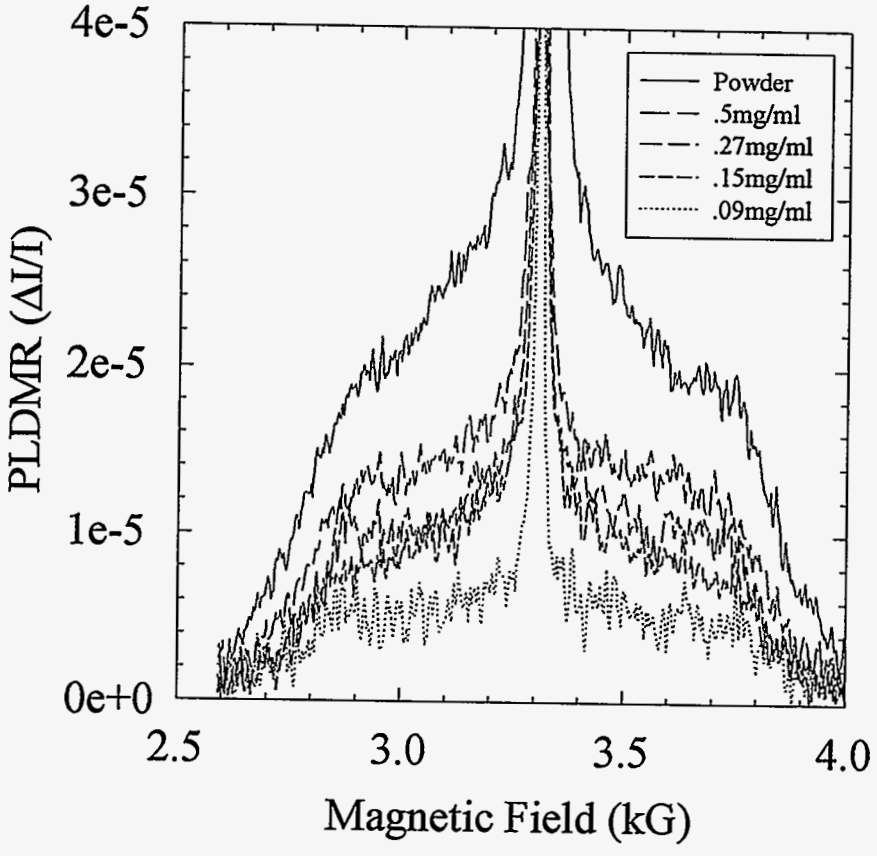

Figure 4.10 The full-field PLDMR of films and frozen toluene solutions of selected concentrations of DBO-PPE at T=15K.

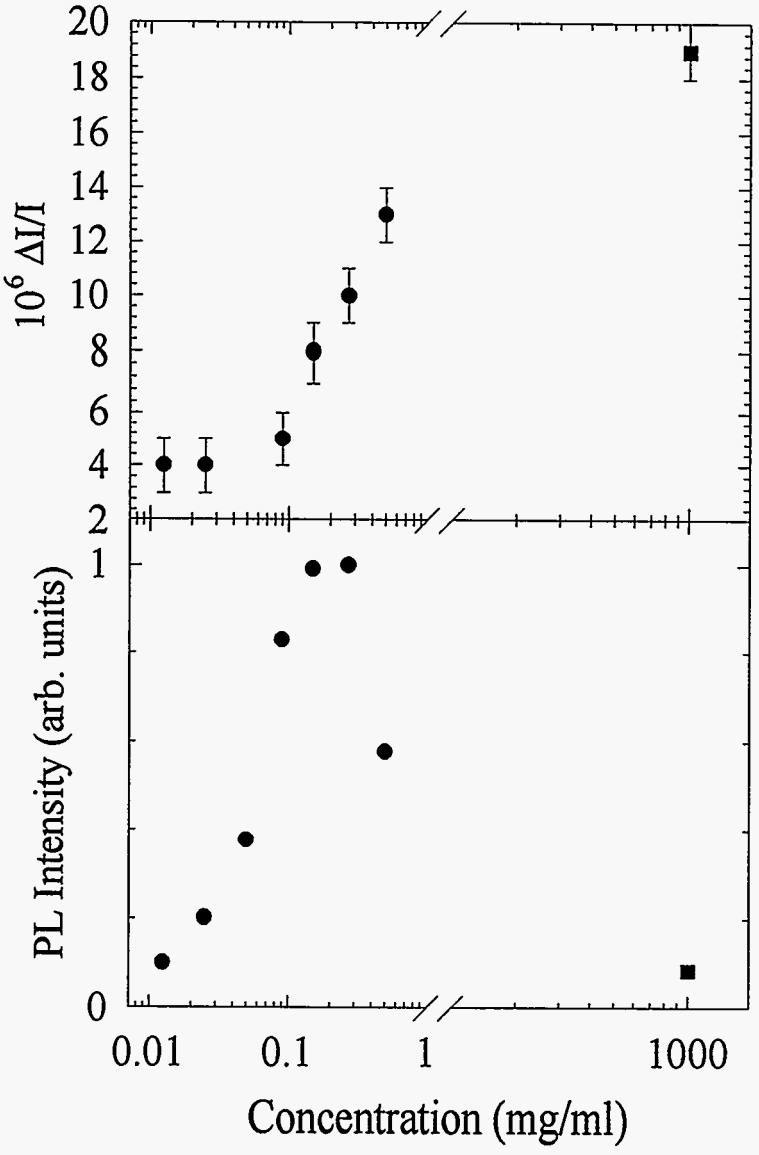

Figure 4.11 The amplitude ΔI/I of the half-field resonance and the PL intensity I vs. concentration of DBO-PPE in toluene at 15K. The values for DBO-PPE powder are shown at the equivalent concentration of 1000mg/ml.

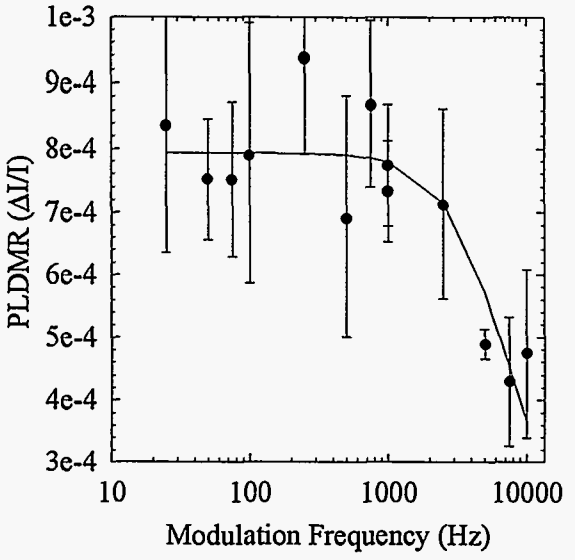

Figure 4.11 The observed behavior, in DBO-PPE, of the modulus of R vs. microwave chopping frequency ν_c at the half-field triplet resonance. T=15K.

4.4 Discussion

In assessing the significance of the results presented in the previous section, we first note that previous room-temperature measurements on P3ATs dissolved in liquid CH_2Cl_2 yielded a polaron resonance but no triplet patterns.[4,41,104] These previous results were to be expected, since fast dynamical quenching of the triplets in liquids also quenches the resonance. However, frozen solutions lock the molecules into a rigid host and therefore the foregoing mechanism should not apply. Therefore, the weakness of the triplet resonance in the frozen saturated m-LPPP solutions (Chapter 3) and its behavior vs. concentration in the PPE solutions demands a different explanation. The results clearly suggest a model requiring an interchain site such as a small trapped triplet exciton state that is spatially localized on a phenylene ring and stabilized by a unit of an adjacent chain. The possibility that this state might actually be a triplet charge transfer exciton is discussed below.

As Figures 4.6 and 4.10 indicate clearly, a remnant polaron and triplet pattern with a concentration-independent value of $\Delta I/I$ persist in the dilute limit of frozen DBO-PPE solutions. The response of both the polaron and triplet pattern to concentration are almost identical.

The polaron pattern is reduced in solution, but both the broad and narrow components persist. The lineshape of the spin-½ resonance is identical to that of even the most dilute solution. Therefore, it is likely that DBO-PPE is not fully dissolving in solution, allowing both interchain and intersegment polarons to view approximately the same environment they see in the powder. The lifetimes indicate that the processes affected by resonance are slower in solution (Figure 4.7 and 4.8), presumably due to the larger polaron separation. The intersegment lifetimes should not increase; the same effect was observed in m-LPPP.

The possibility that the triplet pattern is due to triplet states stabilized by solvent-polymer coupling is improbable since any such coupling should yield a stronger signal and the shape of the pattern would be concentration dependent, in contrast to its invariance. In addition, we note that the behavior of the pattern in tetrahydrofuran (THF) solutions, in which the solvent lacks π bonds, was identical to its behavior in the toluene. We consequently consider alternative possibilities: The remnant pattern is due to (i) some type of intrachain sites which stabilize the low-lying triplet state and (ii) interchain sites in aggregates, i.e. colloids or small bundles of molecules, that are present in the dilute limit. Yet if the invariance of the shape of the triplet powder pattern rules out solvent-polymer coupling, it should also rule out intrachain sites. We also note that UV irradiation of PPE powders, which should induce crosslinking by elimination of π bonds and formation of σ bonds between adjacent units of neighboring chains, did not affect $\Delta I/I$ appreciably. We therefore suggest that the remnant triplet resonance signal is due to remnant aggregates or colloids which are present even in the dilute limit.

The picture of triplets stabilized by adjacent polymer units provides additional insight into previous studies. The early PLDMR studies of P3AT[41] and PPV[103] films suggested that the degree of axial symmetry of the triplet states varied widely among the films and

decreased rapidly with increasing temperature. At the same time, while the full- and half-field triplet patterns become increasingly structureless with increasing temperature, the overall width is temperature invariant. In addition, in the ordered state of PPV, the phenylene units from one chain are apparently stacked adjacent to the vinylene units on the neighboring chains.[105] This behavior indicates strongly that the distribution of D values is essentially temperature independent, but that of E increases with T. Thus, while isolated phenylene rings provide a symmetric (E = 0) environment for triplets, coupling with an adjacent vinylene, ethynylene, phenylene, or another bridging unit, and static and dynamical disorder lead to deviations from such symmetry (E > 0).

We note that the foregoing model is also consistent with the behavior of C_{60} and C_{70}. In matrix-isolated fullerene molecules, only the triplet state which is delocalized over the entire molecule is observable by light-induced ESR or PLDMR.[75,77] In fullerene films, however, the PLDMR includes an additional broad triplet pattern similar to that described in this chapter and consequently believed to be localized on a face adjacent to a neighboring molecule.[75,77] It therefore appears that this long-lived triplet is an intrinsic trapped state of π-conjugated rings stabilized by coupling to a unit of an adjacent molecule.

The identification of the foregoing intrinsically trapped triplet state with the source of the triplet PA band and the states resulting from the fusion of spin-parallel carriers in polymer LEDs[32,48,98] is not firmly established. We note, however, that the temperature dependence of the triplet PA band in CN-PPV is similar to that of the triplet PLDMR, and both are observable at higher temperatures than in typical PPVs.[32] Furthermore, there are no indications of additional triplet states in either the PLDMR or PA spectra. We therefore believe that the intrinsically trapped triplet states observed by PLDMR, those observed in polymer LEDs, and those responsible for the triplet-triplet PA band are essentially identical states.

Finally, we note that the mechanism yielding the triplet PLDMR had previously been assigned to spin-dependent triplet-triplet fusion to singlets.[41,103] This mechanism, however, is problematic since it should result in delayed fluorescence in the 10-100 ms time range. Such delayed fluorescence, however, is unobservable, and the resonance is suggested to result

from the role of triplets as nonradiative singlet quenching centers[32] and/or ground-state repopulation.[8]

4.5 Conclusions

In conclusion, the photoluminescence detected magnetic resonance spectra of frozen toluene solutions of derivatives of poly(*p*-phenylene ethynylene) suggests that the triplet state is an intrinsic long-lived (~30 μs in PPEs) trapped state localized on a phenylene ring and stabilized by coupling to a unit of an adjacent chain. The polaron resonance results from interchain and intersegment pairs which are only barely modified in solution due to remaining aggregates.

CHAPTER 5. PLDMR MEASUREMENTS ON C_{70}, POLYTHIOPHENE, POLY(*P*-PHENYLENE VINYLENE), AND DAN-40

Compiled herein are a number of results which do not warrent a chapter all to themselves, but are important nevertheless. Some of the results, specifically on C_{70}, provide minor corrections to previous work. The results on polythiophene, poly(*p*-phenylene -vinylene) (PPV), and C_{70} are addenda to comprehensive work done by previous students. The work on Dan-40 is in preliminary stages, but is very interesting.

5.1 C_{70}

C_{70} (Figure 2.8(b)) was heavily investigated by P.A. Lane[77,81] for his thesis at Iowa State University. The major discoveries of his comprehensive work are reproduced in Section 2.4. One important measurement, however, was erroneous. The incorrect Phosphorescence Detected Magnetic Resonance (PhDMR) (at 80K) is shown in Figure 2.10(c) while the correct resonance (at 20K) is shown below (Figure 5.1).

The problem occurred because the lock-in amplifier was maximized at the peak of the resonance. The actual resonance was quenching, not enhancing, so the lock-in chose a phase that was 180° away from the microwave chopping frequency. All of the previous results can be corrected simply by reflecting the resonances across the X axis. Therefore, the PhDMR of a C70:T/PS glass ($T < 40K$) consists of two PL-quenching resonances split by ~95G with a more intense low-field resonance. This resonance is assigned to a triplet exciton with zfs parameters $|D|=0.0089cm^{-1}$ and $|E|=0$. The resonance is believed to be due to magnetic resonance conditions interfering with the direct radiative recombination of the triplet.[81] An additional study of the lifetime of the low-field quenching resonance at 10, 15, 20, 30, 40 and 60K was undertaken. Unfortunately, the detector has a lifetime of 30μs, so only lifetimes longer than this could be measured. Fortunately, we were able to extract the lifetime of the C_{70} low-field resonance up to 40K. The resonances at 10, 15 and 20K (Figure 5.2, 5.3 and 5.4, respectively) could be fit using a single time constant (Equation 1.43). The

resonances at 30 and 40K (Figure 5.5 and 5.6) were fit using two time constants (Equation 3.1) with the second time constant set at 30μs, the speed of the detector. The amplitude of the detector contribution to the resonance was left as a variable of the fit. The lifetimes are seen to decrease as the temperature increases (Figure 5.7 and Table 5.1).

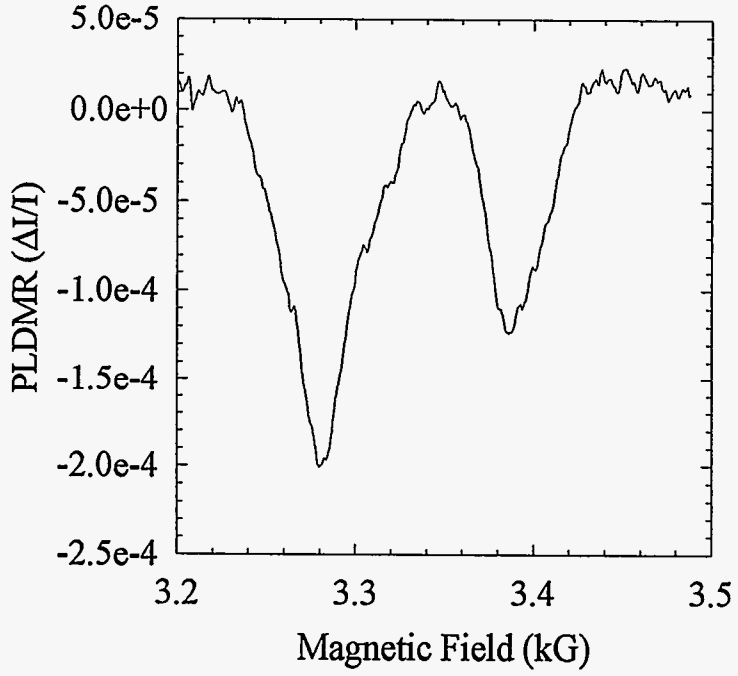

Figure 5.1 PLDMR spectra of the phosphorescence of C_{70} T/PS at 20K.

The resonance in C_{70} results from direct decay of the triplets to the ground state. The fitting procedure was derived assuming an indirect decay. The modulation frequency dependence should look like Figures 1.15 (b) or (d). We see a hint of a peak in Figure 5.5 and 5.6, but only extremely careful measurements between 20K and 40K could resolve this issue. Below 20K, the peak occurs at a modulation frequency below 10Hz. Since the resonances are fit to indirect process equations, the calculated lifetimes will be shorter than those of a direct process.

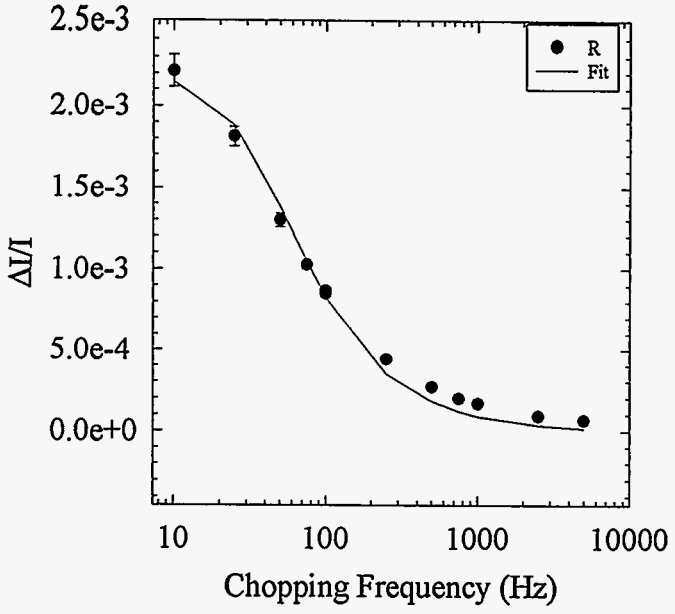

Figure 5.2 Modulus of the low-field phosphorescence-detected magnetic resonance (PhDMR) of C_{70} T/PS at 10K.

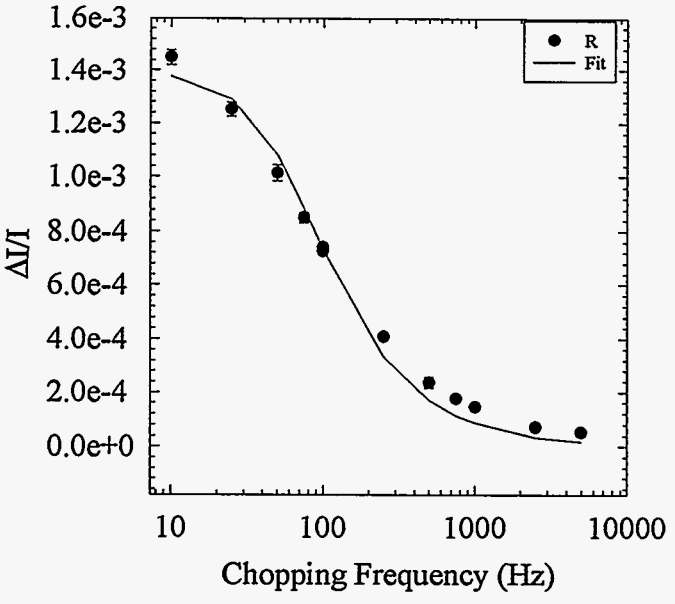

Figure 5.3 Modulus of the low-field PhDMR of C_{70} T/PS at 15K.

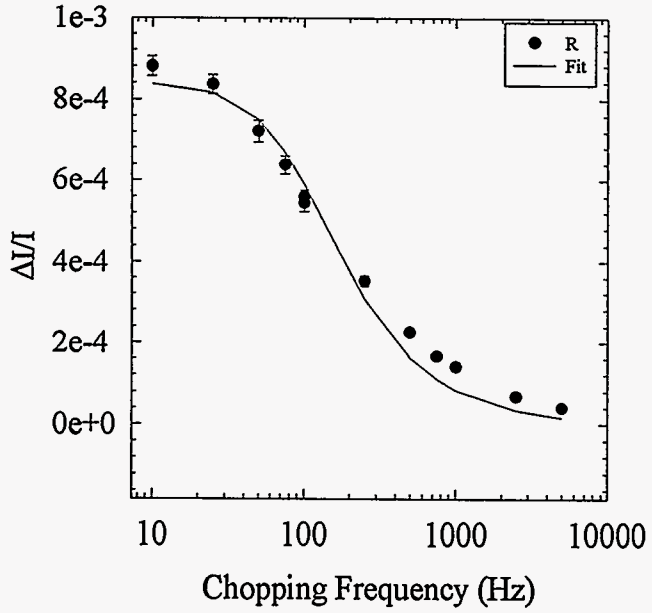

Figure 5.4 Modulus of the low-field PhDMR of C_{70} T/PS at 20K.

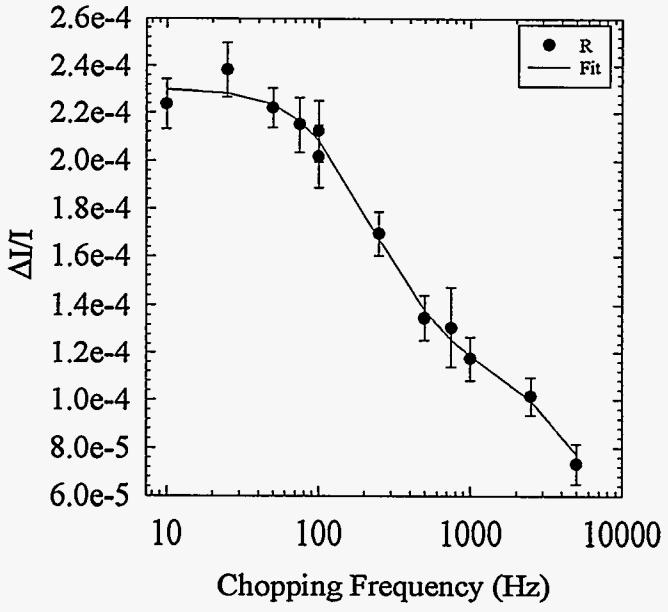

Figure 5.5 Modulus of the low-field PhDMR of C_{70} T/PS at 30K.

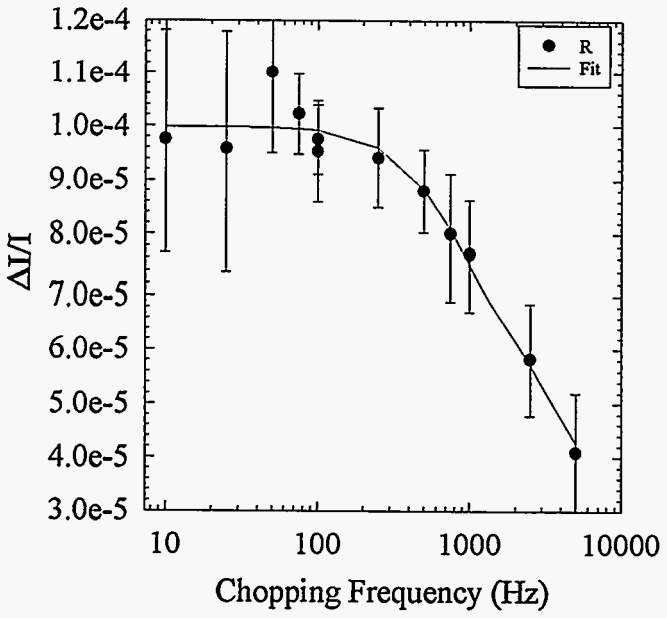

Figure 5.6 Modulus of the low-field PhDMR of C_{70} T/PS at 40K.

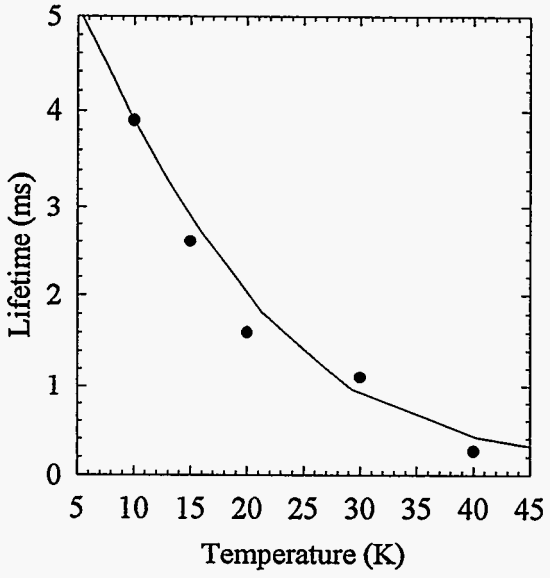

Figure 5.7 C_{70} Lifetime vs. Temperature for the low-field PhDMR of C_{70}:T/PS.

Table 5.1 Lifetime of low-field C_{70} resonance.

Temperature (K)	Lifetime (ms)
10.0	3.9
15.0	2.6
20.0	1.6
30.0	1.1
40.0	0.3

5.2 Lifetime Measurements on π-conjugated Polymers

The lifetime measurements on π-conjugated systems have provided new insights and new questions about the behavior of the species affected by resonance conditions. All of the measurements in this chapter are taken at the peak of the spin-½ resonance.

Figure 5.8 plots the modulation frequency dependence the resonance of poly(3-hexylthiophene) film (similar to P3AT in Figure 2.6). Figure 5.9 contains the same information for DBO-PPV powder prepared by F. Wudl and co-workers.[106] Figure 5.10 gives the modulation frequency measurements for a well-ordered PPV film provided by Cambridge.[107]

Table 5.2 contains the lifetimes (τ_1 and τ_2) and the amplitudes (c_1 and c_2) of the polymer systems investigated in this study. Note that all of the polymer lifetimes were taken at 811mW except for the PPE film and solution. Although the vagaries of a fitting procedure utilizing four independent variables can often lead to questionable values, the relative agreement among all of the polymers may indicate believable fits. The values for m-LPPP and PPE from Chapters 3 and 4 respectively, are reproduced in Table 5.2.

Table 5.2 provides several noteworthy observations. DBO-PPE, DHO-PPV and Cambridge-PPV (Camb.-PPV) and m-LPPP solids have slow or fast lifetimes which are all within the same order of magnitude.

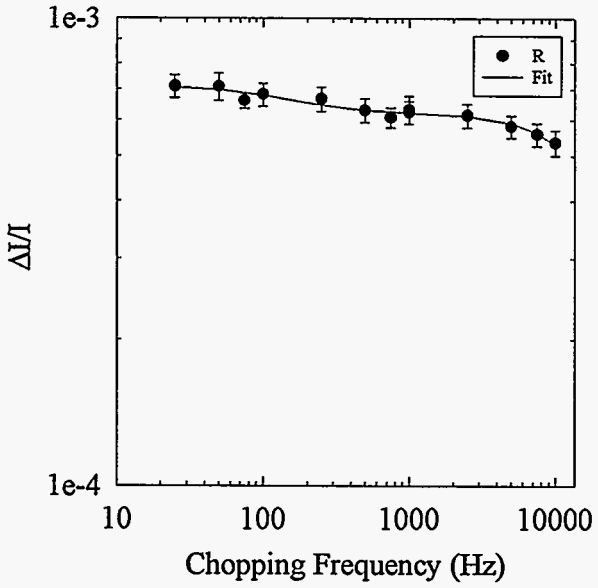

Figure 5.8 Modulus of the g=2 PLDMR signal of P3HT powder at 20K.

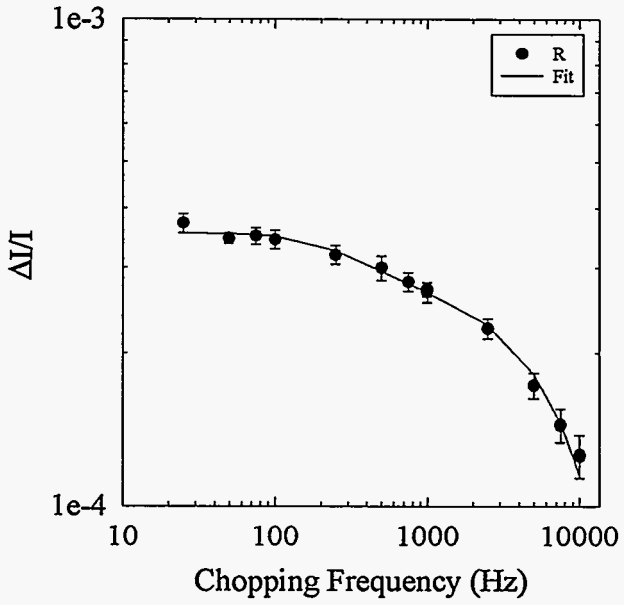

Figure 5.9 Modulus of the g=2 PLDMR signal (T=20K) of DBO-PPV powder prepared by F.Wudl and coworkers.[106]

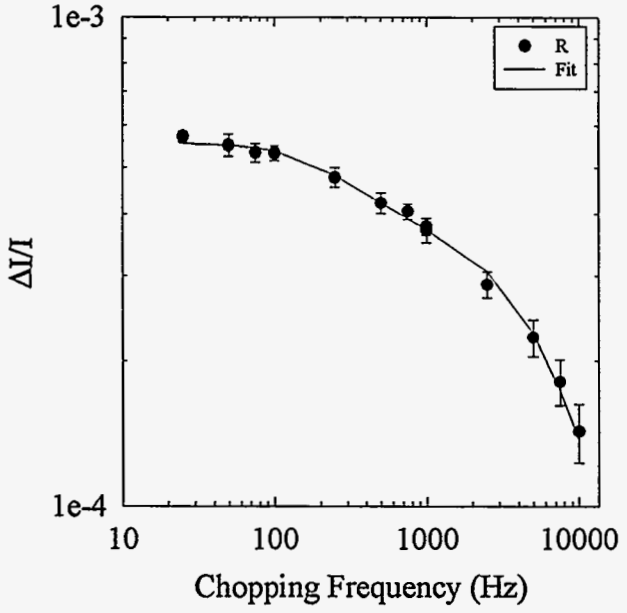

Figure 5.10 Modulus of the g=2 PLDMR of Cambridge PPV film at 20K.[107]

Table 5.2 Summary of time constants for π-conjugated polymers.

Sample	Power (mW)	τ_1(μs)	τ_2(μs)	c_1/c_2
P3HT	811.0	9.0	1,868.0	6.4
DBO-PPV	811.0	30.0	575.0	2.1
Camb. - PPV	811.0	36.0	677.0	1.4
PPE Film	400.0	12.0	238.0	2.0
PPE Sol'n	400.0	152.0	2,145.0	2.5
LPPP Film	811.0	39.0	666.0	1.4
LPPP Sol'n	811.0	365.0	3,280.0	2.1

The similarity between the well-ordered Camb.-PPV and m-LPPP film is striking. The amplitude of the lifetimes (c_1/c_2) are identical and the slow and fast lifetimes are within ~2% and ~8%, respectively. Camb.-PPV and m-LPPP slow and fast lifetimes are both slower than those in DHO-PPV by a factor of ~1.3 and than those in DBO-PPE by a factor

of ~3. The DHO-PPV and DBO-PPE have lifetime amplitudes (c_1/c_2) of 2 and 2.1 respectively.

In looking at these results, we know that m-LPPP and Camb.-PPV are the most well-ordered and therefore we suspect that the longer lifetimes are a result of greater polaron separation due to fewer conjugation defects and larger interchain separation. The PPE is probably the most disordered, allowing intersegment polarons to easily recombine utilizing the cylindrical π-cloud around the triple bonds. This leads to the fastest τ_2 observed in any of these π-conjugated polymers. The disorder of DHO-PPV and DBO-PPE leads to a situation where the interchain polarons are recombining at a rate of approximately 2:1 over intersegment pairs.

The behavior of P3HT mimics none of the behaviors of the phenylene-based polymers. Whereas in the phenylene-base polymers $\tau_2 \sim 20\tau_1$ and $1.4 < c_1/c_2 < 2.1$, P3HT has $\tau_2 \sim 200\tau_1$ and $c_1/c_2 \sim 6.4$. The qualitative differences are obvious by comparing Figures 5.8 and 5.9. The very small interchain lifetime may be due to closer packing, although this lifetime in P3HT is not much faster than that in DBO-PPE. However, the intersegment lifetime is an order of magnitude larger, possibly due to the reduced torsional stability of the rings with respect to each other.

5.3 Dan-40

This subchapter describes the preliminary results of the spin-1 resonance in the copolymer Dan-40 (Figure 5.11) provided by Ohio State University.[108]

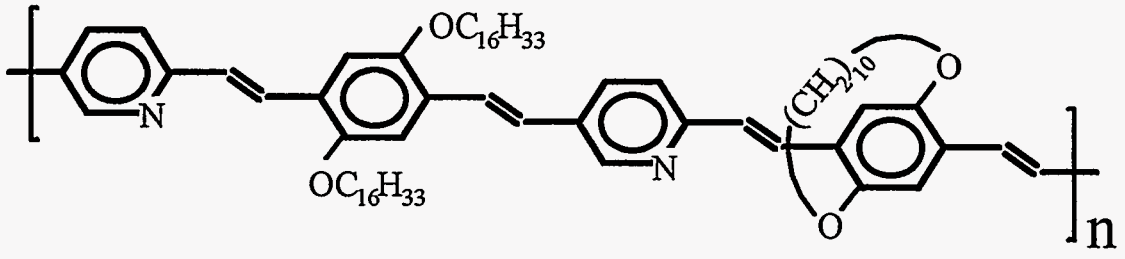

Figure 5.11 Chemical structure of Dan-40. n is not known.

This polymer structure is especially interesting because of the $(CH_2)_{10}$ bridge across the some of the phenyl rings. We might expect that the bridge would have some effect on the triplet state which is presumed to be located on the phenyl ring. The unbridged units are PPV, so a triplet resonance similar to that observed in pure PPV, should also be observed.

The preliminary PLDMR measurements on the triplet turned up some very interesting results. Normally, both the X and Y channels from the lock-in are recorded. The X spectra and the Y spectra are typically identical except for the amplitude. However, in the case of the full-field triplet of Dan-40, the in-phase (X) and out-of-phase (Y) components showed different triplet signatures (Figure 5.12).

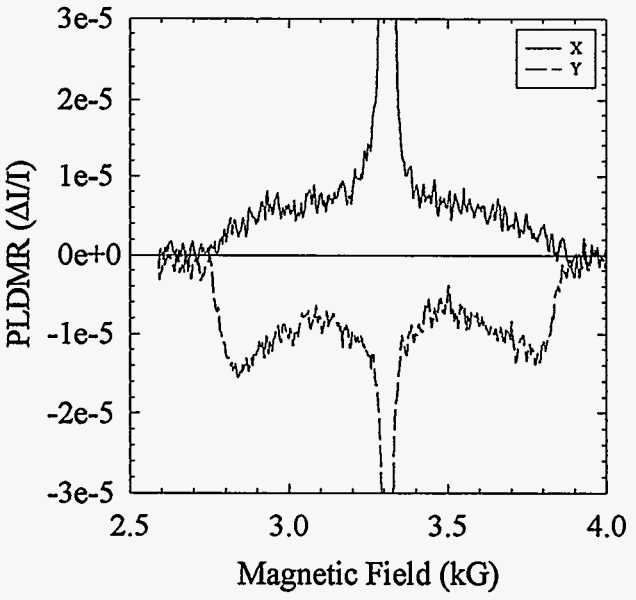

Figure 5.12 The in-phase (X) and out-of-phase (Y) full-field PLDMR of Dan-40 film at 20K.

The faster X component has broad shoulders like PPE, perhaps reflecting a distribution of D and E values. The slower Y component looks like PPV indicating E~D/3. The triplet stabilized by the bridging unit is probably in the most disordered environment, so we assign the in-phase component to this location.

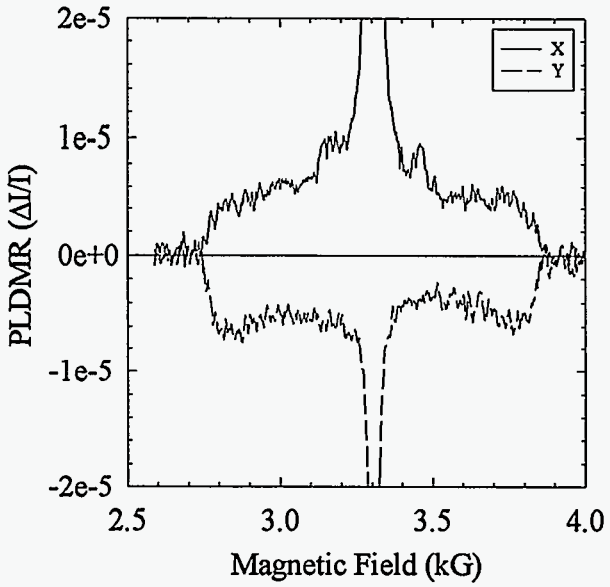

Figure 5.13 The in-phase (X) and out-of-phase (Y) full-field PLDMR of Dan-40 solution at 20K.

The triplet which looks like PPV is assigned to the PPV units. Dan-40 solution (Figure 5.13) shows only a slightly different X and Y spectra, indicating that either (i) the solvent is modifying the triplet distribution or (ii) the Y triplet is stabilized by neighboring chains. Since the Y triplet is the triplet like PPV, it would be expected to decrease with decreasing concentration whereas the triplet stabilized by the bridging unit should remain essentially constant.

The same measurements were taken on the half-field of Dan-40 (Figure 5.14). We would have expected, from the results shown in Figure 5.12, the half-field X and Y spectra to differ. Instead, the X and Y half-field spectra were absolutely identical. This fact alone is strange, for the only place where X=Y is at $\omega\tau=1$ (Figure 1.14(d) and Equation 1.36). This may just indicate that the chopping frequency of 1kHz was a serendipitous choice and the lifetime of the triplet is 16μs. However, we believe that more interesting processes are occurring here. Obviously more measurements must be taken to resolve this paradox.

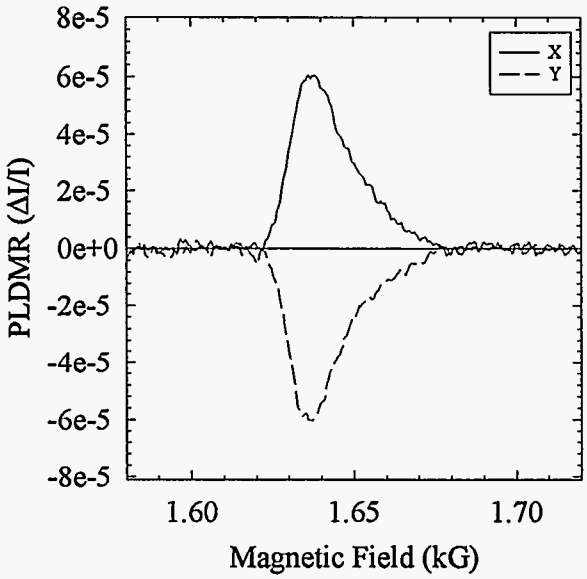

Figure 5.14 The in-phase (X) and out-of-phase (Y) half-field PLDMR of Dan-40 film at 20K.

APPENDIX A
OPERATION OF ODMR SPECTROMETER

There are 6 major systems which make up the ODMR Spectrometer. Those systems are: excitation source, cryogenics, microwave, magnetic field, detection/amplification and data acquisition. For a general explanation, refer to Section 1.4. A schematic of the system, Figure A.1 is included below. There are 4 main equipment racks. Equipment rack 1 (ER1) contains the magnet power supply. Equipment rack 2 (ER2) contains, among other things, the lock-in amplifiers. Equipment rack 3 (ER3) contains the Varian fluxmeter. Equipment rack 4 (ER4) contains the UV Lamp. The large optical bench (OB) contains the monochromator, silicon detectors and photomultiplier tubes (PMT). The microwave gear support table (MGST) is above the magnet.

Excitation Source

Laser turn on procedure:

1) Turn on main power supply (large red knife switch near A301 entrance).
2) Turn on cooling water to laser (two marked yellow water switches near floor on south wall under the east-most window).
3) Turn on water pump to reduce laser cooling water back pressure (Breaker #28 on south wall).
4) Warm up laser by turning key switch on the black laser control box, located on the optical table. Wait until red light under 'reset' comes on. Warning: Do NOT turn on key switch before turning on main power supply (step #1). Push 'reset' button. After about 10 seconds, the needle in the gauge on the laser control box should move to about 8A.
5) Once the laser is on, adjust to the desired current with the light and current control knobs. (A current of ~10A is usually sufficient at 488nm). Try to avoid any rapid, large changes in the current.

Laser Stabilizer:

1) The Laser intensity stabilizer, located on top of the meter monochromator, should always have its Power and Temperature Control buttons turned on.

2) Once the laser is on, turn the high voltage button on. This high voltage button should not be operated when the laser is off. Turn the laser power knob until the desired power is reached and the overload light is off. If the stabilizer is properly adjusted, this occurs around 2 milliamps.

Laser Interlock:

1) Make sure the door to the lab is closed.

2) The blue laser interlock control box is located on the optical table. Turn the shutter enable key to the right and press the 'open shutter' button. The red light indicates an open interlock.

Laser shut down procedure:

1) Turn laser current down by turning current control and light control knobs all the way to the left.

2) Then reverse the abovementioned steps 4, 3 and 1, but allow 20 minutes of cold water circulation (step 2) to continue to cool down the laser and power supply.

UV Lamp turn on procedure:

1) Turn on the power switch on the LPS225HR power supply in ER4.

2) Press the 'start lamp' button until the lamp lights or until 5 spark attempts are made. If, after 5 spark attempts are made and the lamp still does not light, pause briefly before trying again.

UV Lamp shut down procedure:

1) Turn off power switch on LPS225HR power supply.

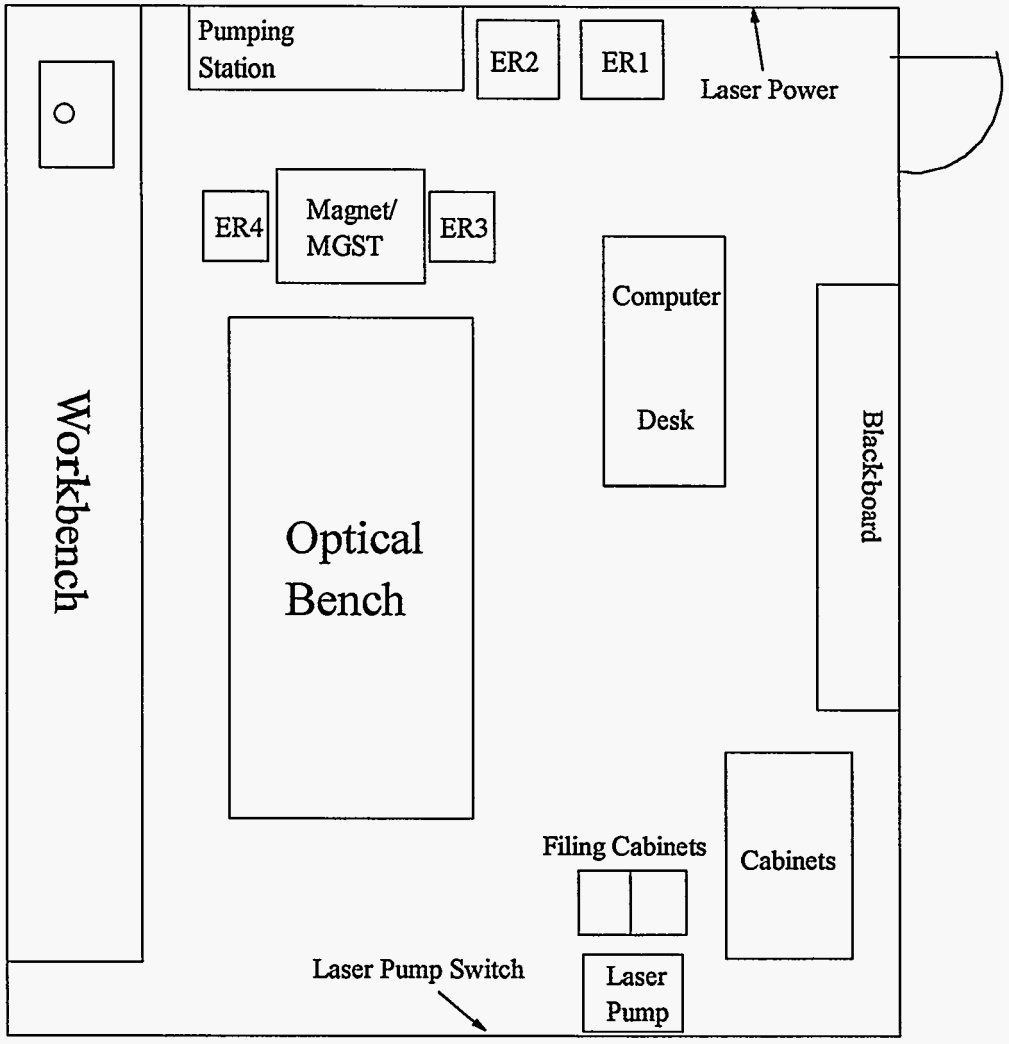

Figure A.1 Schematic of physics A301.

Cryogenics

Cryogenics start up procedure:

1) Fill dewar behind magnet with liquid nitrogen and insert the probe (blue wire) into the liquid. Cover dewar with styrofoam cap.

2) Turn on OXFORD ITC4 temperature controller above ER3.

3) Open the adjustment knob on the top of the transfer tube (right hand rule) one or two turns to allow free flow of helium.

4) Open the silver helium flow knob on the pump controller. The pump controller is the box sitting on top of the temperature controller.

5) Turn the helium pump which is located on the floor to the left of ER2.

6) Turn on nitrogen flow around sample. The nitrogen cylinder is located to the right of the blackboard. A small flow is sufficient.

7) When the desired temperature is reached, the flow can be adjusted with the silver knob on the pump controller (vacuum at .2bar is usually very stable) and the black knob on the transfer tube.

Cryogenics shut down procedure:

1) Reverse steps 5 and 4 above.

2) After the temperature has gone above the freezing point of water, turn off the nitrogen (step 6 above) and the temperature controller (step 2).

Microwaves

Microwave start up procedure:

1) The Gunn Diode Power Supply (GPS) on top of ER3 should always be left on. If it is off, turn it on.

2) The 8010H Traveling Wave Tube Amplifier is on the northwest corner of the microwave gear support table takes 10 minutes to warm up. Check that operate/standby switch is on 'standby' and turn on the power switch.

3) The 110dB and 11dB attenuators located above the GPS on the MGST should be turned down to approximately 80dB and 10dB respectively.

4) Turn on the large, old RM561A oscilloscope in ER2.

5) Turn on the 6530 frequency counter and switch the selector switch to 500MHz-18GHz.

6) Check to see that the analog frequency meter reads roughly the same frequency as the digital counter.

7) Turn the Traveling Wave Tube Amplifier (TWTA) on.

8) Slowly turn up the 110dB attenuator until square wave forms are observed on the oscilloscope.

9) Minimize the distance between the trough and the peak of the wave displayed in the lower two traces. This will maximize the top trace. This is a skill that takes a lot of practice, but here are a few hints:

a) The middle trace can be minimized with the analog frequency meter.

b) The lower trace can be minimized with appropriate turns of the voltage knob on GPS.

c) Once the lower trace is as low as it can go, it is sometimes necessary to use the joystick on top of the GPS to make the trough and the peak lie in the same line.

When you are finished, the oscilloscope should look like the traces in figure A.2.

10) Slowly continue to turn up the attenuators until the desired attenuation in reached. Remember that there is 20dB of attenuation at the input of the TWTA. The microwave power at any given attenuation is given in Appendix B.

Microwave shut down procedure:

1) Turn the 110dB and 11dB attenuators to approximately 80dB and 10dB respectively.
2) Turn TWTA to standby and then turn the power off.
3) Turn off the oscilloscope and the microwave frequency counter.

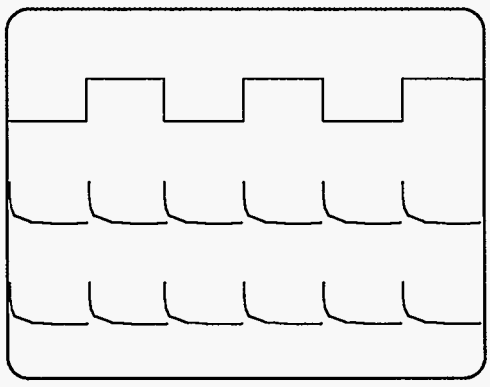

Figure A.2 Oscilloscope trace for coupled microwaves.

Magnetic Field

Magnetic Field turn on procedure:

1) Turn on the magnet power supply water lines located to the right of the pumping station.

2) Make sure the coarse current adjustment on the face of the HS-1050 Precision Magnet Power Supply (located in ER1) is turned down.

3) Unplug the control input from the magnet power supply.

4) Turn on magnet power supply.

5) Turn on the magnet voltage monitor (HP 3455A Digital Voltmeter) located in ER3.

6) Turn on the fluxmeter (Varian Model F-8 Fluxmeter) also located in ER3.

7) Set the voltage divider (on the top of ER1) to reflect the desired sweep. The voltage divider settings are reproduced in Appendix B.

8) Switch the frequency counter (above ER3) to the 10Hz-500MHz range. Rotate the tuning knob until the NMR frequency (given by the frequency counter) is the same as the frequency required for the desired sweep. (See Appendix B)

9) Make sure the amplitude knob on the fluxmeter is turned all the way to the right.

10) Turn up the current to the magnet until the NMR resonance is seen on the small oscilloscope screen in the fluxmeter (Figure A.3).

11) Center the "valley" above the line on the tape pasted to the screen.

12) Slowly turn the amplitude knob to the left, using the tuning knob to keep the valley above the line on the tape.

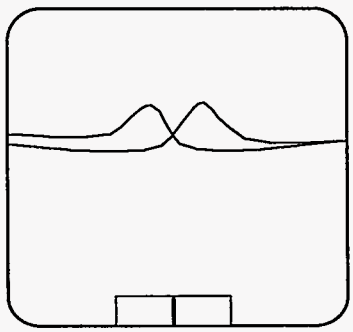

Figure A.3 Properly adjusted fluxmeter.

13) Once the amplitude knob is turned all the way to the left the magnet is ready to go. The control input can be plugged in once the data acquisition board has been initialized (see below).

Magnetic Field shut down procedure:

1) Unplug the control input and slowly turn the course current control on the power supply down to zero. Press the red button to turn off the power supply.
2) Turn off the voltmeter and frequency counter (ER3).
3) Turn the amplitude knob on the fluxmeter (ER3) all the way to the right and turn off the power.

Detection/Amplification

Silicon Detector:

1) Adjust the mirrors so that the photoluminescence strikes the active element.
2) Make sure that the signal cable is connected to the silicon detector.
3) Turn on power. Observe a voltage on the voltmeter either in ER2 or on top of the helium pump controller (MGST).

Photomultiplier Tube turn on procedure:

1) Adjust the mirrors so that the photoluminescence strikes the monochromator slits. If an integrated intensity is desired, set the monochromator on zero.
2) Make sure that the signal cable is connected to the amplifier (brown box) on the photomultiplier tube (PMT) and turn the amplifier on.
3) Check that the PMT power supply (Fluke High voltage power supply located in ER3) is on standby. With the room lights out, turn on the power. Once the power supply is ready, turn it from standby to on. Slowly increase the voltage, observing the voltage on the voltmeter either in ER2 or on top of the helium pump controller (MGST). Do not allow the

voltage to increase beyond the safe limit (which varies depending on which PMT is being used).

Photomultiplier Tube turn off procedure:

1) Turn down voltage on Fluke power supply and switch to standby. Turn power off.
2) Turn off PMT amplifier

Lock-in Amplifier:

1) Turn on the power to the lock-in amplifier located in ER2.

Data Acquisition

The data acquisition system is undergoing an upgrade to GPIB.

APPENDIX B

ODMR SYSTEM PARAMETERS

Important ODMR System Parameters are reproduced here:

Resistor Box Settings:

Sweep Width (Gauss)	Number of Steps	Resistor Setting
40	400	0.0420
50	400	0.0512
80	400	0.0819
120	400	0.1229
180	400	0.1843
300	600	0.2362
500	400	0.6000
900	600	0.6960
1000	600	0.7720
1500	600	0.9999

NMR Frequency Settings:

Sweep Width (Gauss)	Field (kG)	NMR Frequency
g=2	3.3408	14.2237
40	3.3208	14.1385
50	3.3158	14.1172
80	3.3008	14.0534
120	3.2808	13.9682
180	3.2508	13.8405
300		
500	3.0908	13.1593
900	2.8908	12.3077
1000		
1500	2.5908	11.0305
2000	2.3408	9.9661
g=4	1.6467	7.0108
40	1.6267	6.9256
50	1.6217	6.9043
80	1.6067	6.8405
120	1.5867	6.7553
180	1.5567	6.6276

Calibration for A301 Microwave Attenuator

Attenuation (dB)†	Power
31	1.74 W
32	1.48 W
33	1.22 W
34*	969 mW
35*	811 mW
36	644 mW
37*	511 mW
38*	405 mW
39	322 mW
40*	256 mW
41*	203 mW
42*	161 mW
43*	128 mW
44*	102 mW
45*	80.5 mW
46*	64.0 mW
47*	51.0 mW
48*	40.0 mW
49*	32.0 mW
50*	25.5 mW
51*	20.1 mW
52*	16.0 mW
53*	12.8 mW
54*	10.1 mW
55*	8.0 mW
56*	6.4 mW

†includes a 20dB attenuator at the input of the traveling wave tube amplifier
*calculated from data points

APPENDIX C
SPECIAL PURPOSE CIRCUITRY

The MetraByte DAS-20 has a couple of major shortcomings. The main shortcoming is the inability to read voltages in the range of -10V to +10V. The DAS-20 can only read 0-10V. Conversion to a ±10V system will allow use of the lock-in amplifier without having manually input an offset into the lock-in.

The second major shortcoming of the DAS-20 is that in some instances it will not trigger on the rising edge of a square wave. Instead, the DAS-20 will start if the voltage is +5V. Therefore, it might trigger at the start of the square wave, in the center, or near the end. The following circuitry solves that problem by generating a short 5V pulse at the rising edge of the square wave and remains at 0V the rest of the time.

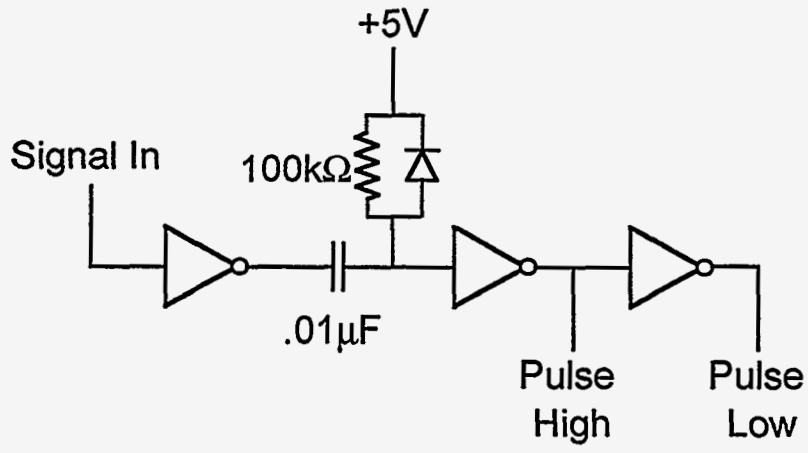

Figure C.1 Pulse generating circuitry.

When taking CDMR measurements using the current input of the lock-in amplifier, it is important to get rid of the large offset current. This is accomplished by the following simple high-pass filter.

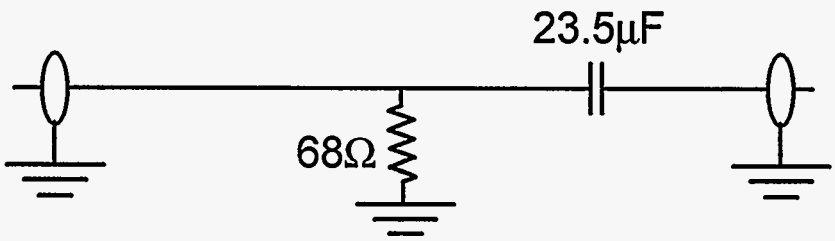

Figure C.2 Low pass circuitry.

REFERENCES

1. C. Poole, *Electron Spin Resonance* Wiley, New York (1983).

2. M. Sharnoff, *J. Chem. Phys.* **46**, 3263 (1967).

3. C. Kittel, *Introduction to Solid State Physics* (Wiley, New York, 1986).

4. J. Shinar in *Handbook of Organic Conductive Molecules and Polymers Vol. 3* edited by H.S. Nalwa, (John Wiley & Sons, NY 1997) Ch. 7.

5. N. Atherton, *Electron Spin Resonance Theory and Applications* (Halsted, New York, 1973).

6. L.S. Swanson et al., in *Advanced Organic Solid State Materials*, edited by L.Y. Chiang et al., (Mat. Res. Soc. Symp. Proc. **173**, Pittsburgh, PA, 1990), p.385.

7. L. S. Swanson, et al., *Phys. Rev. B* **44**, 10617 (1991).

8. R. Clark, ed., *Triplet State ODMR Spectroscopy* (Wiley, New York, 1982).

9. P.C. Taylor, J.F. Baugher, and H.M. Kriz, *Chemical Rev.* **75**, 203 (1975).

10. H.M. McConnell in *Molecular Biophysics*, eds. B. Pullman and M. Weissbluth, (Academic Press, New York, 1965), p.311

11. H.A. Kramers, *Quantum Mechanics* (North-Holland, Amsterdam, 1977), Sec. 74

12. A. Nishimura and J. Vincent, *Mol. Cryst. and Liquid. Cryst.* **17**, 197 (1972).

13. G.E. Pake, *J. Chem. Phys.* **16**, 327 (1948).

14. D.R. Torgeson et al., *J. Magn. Reson.* **64**, 85 (1986).

15. J.F. Baugher et al., *J. Chem. Phys.* **50**, 4914 (1969).

16. L.S. Swanson, Ph.D. Dissertation, Iowa State University, Ames, IA (1992).

17. J.J. Davies, *Contemp. Phys.* **17**, 275 (1976).

18. F. Boulitrop, *Phys. Rev. B* **28**, 6128 (1983).

19. S. P. Depinna and D. J. Dunstan, *Phil. Mag.* **50**, 579 (1984).

20. D. M. Hofmann, B. K. Meyer, W. Stadler, A. Kux, V. Petrova-Koch and F. Koch, *ICDS* **17** (1993).

21. C. Botta, S. Luzzati, R. Tubino, D. D. C. Bradley and R. H. Friend, *Phys. Rev. B* **48**, 14809 (1993).

22. P.A. Lane, Ph.D. Dissertation, Iowa State University, Ames, IA (1994).

23. D. J. Dunstan and J. J. Davies, *J. Phys. C* **12**, 2927.

24. S. Depinna et. al., *Phil. Mag. B.* **46**, 473 (1982).

25. S. Depinna, B. C. Cavenett, T. M. Searle and I.G. Austin, *Phil. Mag. B.* **46**, 501 (1982).

26. Kim, Ph.D. Thesis, Ohio State University, Columbus, OH (1995).

27. C. Tsang and R.A. Street, *Phys. Rev. B* 19, 3027 (1979).

28. D. Engemann and R. Fischer, *Structure and Excitation of Amorphous Solids* edited by G. Lucousecy and F. L. Galeener, A.I.P. Conf. Proc. **31**, 37 (New York: American Institute of Physics).

29. D.J. Dunstan, *Phil. Mag. B.* **46**, 579 (1982).

30. C.K. Chiang, C.R. Fincher et al., *Phys. Rev. Lett.* **39**, 1098 (1977).

31. D.D.C. Bradley, *Conjugated Polymer Light Emitting Diodes*, presentation notes.

32. N.C. Greenham, J. Shinar, J. Partee, P.A. Lane, O. Amir, F. Lu, R.H. Friend, *Phys. Rev. B* **53**, 13528 (1996).

33. E. Toon and G. Ellis, *Foundations of Chemistry*, (Holt, Rinehart and Winston, 1973).

34. W.-P. Su, J.R. Schrieffer, and A.J. Heeger, *Phys. Rev. Lett.* **42**, 1698 (1978).

35. W.-P. Su, J.R. Schrieffer, and A.J. Heeger, *Phys. Rev. B* **22**, 2099 (1980).

36. C.E. Swenberg and N.E. Geacintov, *Organic Molecular Photophysics* (J. Wiley, NY 1973) Ch. 10.

37. A.J. Heeger, S. Kivelson, J.P. Schriffer, W.-P. Su, *Rev. Mod. Phys.* **60**, 781 (1988).

38. T.W. Hagler, K. Pakbaz, K. Voss, and A.J. Heeger, *Phys. Rev. B* **44**, 8652 (1991).

39. S. Hayashi, K. Kaneto, and K. Yoshino, *Sol. St. Comm.* **61**, 249 (1987).

40. N.F. Colineri, D.D.C. Bradley, R.H. Friend, P.L. Burn, A.B. Holmes and C.W. Spangler *Phys. Rev. B* **42**, 11670 (1990).

41. L.S. Swanson, J. Shinar and K. Yoshino, *Phys. Rev. Lett.* **65**, 1140 (1990).

42. See references contained in Reference 7.

43. G.S. Kanner, X. Wei, B.C. Hess, L.R. Chen and Z.V. Vardeny, *Phys. Rev. Lett.* **69**, 538 (1992).

44. B. Xu and S. Holdcroft, *J.A. Chem. Soc.* **115**, 8447 (1993).

45. J. Orenstein in *Handbook of Conducting Polymers*, ed. T.A. Skotheim (Marcel Dekker, NY, 1986).

46. L.S. Swanson, J. Shinar, A.R. Brown, D.D.C. Bradley, R.H. Friend, P.L. Burn, A. Kraft, A.B. Holmes, *Phys. Rev. B.* **46**, 15072 (1992).

47. N.S. Sariciftci, L. Smilowitz, A.J. Heeger and F. Wudl, *Science* **174**, (1992).

48. Q.-X. Ni, L. S. Swanson, P. A. Lane, J. Shinar, Y. W. Ding, S. Ijadi-Maghsoodi, and T. J. Barton, *Syn. Met.* **49-50**, 447 (1992).

49. J. Shinar, et al., *Mol. Cryst. Liq. Cryst.* **256**, 691 (1994).

50. J. Shinar, et al., in *Optical and Photonic Applications of Electroactive and Conducting Polymers*, edited by S. C. Yang and P. Chandrasekhar, SPIE Conf. Proc. **2528**, 32 (SPIE, Bellingham, WA, 1995).

51. J. Shinar, *Syn. Met.* **78**, 277 (1996).

52. W. Graupner, J. Partee, J. Shinar, G. Leising, and U. Scherf, *Phys. Rev. Lett.* **77**, 2033 (1996); J. Partee, W. Graupner, J. Shinar, G. Leising, and U. Scherf, *Syn. Met.* (in press).

53. P. A. Lane, J. Shinar, and K. Yoshino, *Phys. Rev. B* **54**, 3602 (1996).

54. M. Yan et al., *Phys. Rev. Lett.* **72**, 1104 (1994).

55. E. L. Frankevich et al, *Phys. Rev. B* **46**, 9320 (1992).

56. S. Hayashi, K. Kaneto, and K. Yoshino, *Sol. St. Comm.* **61**, 249 (1987).

57. D. D. C. Bradley and R. H. Friend, *J. Phys. Cond. Matt.* **1**, 3671 (1989).

58. K. E. Ziemelis et al., *Phys. Rev. Lett.* **66**, 2231 (1991).

59. Z. V. Vardeny and X. Wei, *Mol. Cryst. Liq. Cryst.* **256**, 465 (1994).

60. L. J. Rothberg, private communication with Joseph Shinar.

61. U. Lemmer et al., *Chem. Phys. Lett.* **240**, 373 (1995).

62. D. G. Thomas, J. J. Hopfield, and W. M. Augustiniak, *Phys. Rev. A* **140**, 202 (1965).

63. P. Gomes da Costa and E. M. Conwell, *Phys. Rev. B* **48**, 1993 (1993);
H. A. Mizes and E. M. Conwell, *ibid.* **50**, 11243 (1994);
E. M. Conwell and H. A. Mizes, *ibid.* **51**, 6953 (1995).

64. E. M. Conwell, J. Perlstein, and S. Shaik, *Phys. Rev. B* **54**, R2308 (1996).

65. D. Kaplan, private communication; F. Garnier, G. Horowitz, A. Yassar, D. Fichou, P. Valat, and V. Wintgens, *Syn. Met.* (in press 1996).

66. C. H. Lee, G. Yu, and A. J. Heeger, *Phys. Rev. B* 47, 15543 (1993); K. Pakbaz, C. H. Lee, A. J. Heeger, T. W. Hagler, and D. McBranch, *Syn. Met.* **64**, 295 (1994).

67. J. Shinar, J. Partee, A. V. Smith, P. A. Lane, X. Wei, Z. V. Vardeny, and K. Yoshino, unpublished results.

68. B. C. Cavenett, *Adv. Phys.* **30**, 475 (1981).

69. M. Yan, et al., *Phys. Rev. Lett.* **73**, 744 (1994).

70. E. L. Frankevich, private communication with Joseph Shinar.

71. X. Wei, B. C. Hess, Z. V. Vardeny, and F. Wudl, *Phys. Rev. Lett.* **68**, 666 (1992).

72. J. Shinar, private communication with E.M. Conwell.

73. P. A. Lane, X. Wei, and Z. V. Vardeny, *Phys. Rev. Lett.* **77**, 1544 (1996).

74. E.J.J. Groenen, O.G. Poluektov, M. Matsushita, J. Schmidt, J.H. van der Waals and G. Meijer, *Chem Phys. Letters* **197**, 314 (1992).

75. P.A. Lane, L.S. Swanson, Q.-X. Ni, J. Shinar, J.P. Engel, T.J. Barton and L. Jones, *Phys. Rev. Lett.* **68**, 887 (1992).

76. X. Wei et al., *Solid State Commun.* **85**, 455 (1993); *Synth. Met.* **54**, 273 (1993).

77. P.A. Lane and J. Shinar, *Phys. Rev. B* **51**, 10028 (1995).

78. Carlos A. Steren, Hans van Willigen, and Marco Fanciulli, *Chem. Phys. Lett.* **245**, 244 (1995).

79. X. Wei, unpublished results (1994).

80. J. Partee, J. Shinar, S. Jessen, A. Epstein, W. Graupner, and G. Leising unpublished results (1996).

81. P.A. Lane, X. Wei, Z.V. Vardeny, J. Partee, J. Shinar, *Phys. Rev. B* **53**, R7580 (1996).

82. R.A. Street, *Phys. Rev. B* **26**, 501 (1982).

83. J. Stampf, S. Tasch, G. Leising, U. Scherf, *Synth. Met.* **71**, 2125 (1995).

84. W. Graupner, S. Eder, M. Mauri, G. Leising, U. Scherf, *Synth. Met.* **69**, 419 (1995).

85. W. Graupner, G. Leising, G. Lanzani, M. Nisoli, S. DeSilvestri, U. Scherf, *Phys. Rev. Lett.* **76**, 847 (1996).

86. U. Scherf, K. Müllen, Makromol. Chem., *Rapid Commun.* **12**, 489 (1991).

87. J. Grüner, H.F. Whittmann, P.J. Hamer, R.H. Friend, J. Huber, U. Scherf, K. Müllen, S.C. Moratti, A.B. Holmes, *Synth. Met.* **67**, 181 (1994).

88. W. Graupner, J. Partee, J. Shinar and G. Leising, unpublished results.

89. W. Graupner et al., *Mol. Cryst. Liq. Cryst.* **252**, 431 (1994).

90. T. Pauck et al. *Chem. Phys. Lett.* **244**, 171 (1995).

91. K. Petritsch, Diploma Thesis, Graz University of Technology, Graz, Austria (1996).

92. V. Dyakonov, G. Rösler, M. Schwoerer, S. Blumstengel, K. Lüders, *J. Appl. Phys.* **79**, 1556 (1996).

93. U. Rauscher, L. Schütz, A. Greiner, H. Bässler, *J. Phys. Cond. Matter* **1**, 9751 (1996).

94. R. Kersting, U. Lemmer, R.F. Mahrt, K. Leo, H. Kurz, H. Bässler, E.O. Göbel, *Phys. Rev. Lett.* **70**, 3820 (1996).

95. G. Kranzelbinder, Diploma Thesis, Graz University of Technology, Graz, Austria (1996).

96. Y.W. Ding, Ph.D. Thesis, Iowa State University, Ames, IA (1994).

97. R.H. Friend et al. *J. Phys. D.* **20**, 1367 (1987).

98. L.S. Swanson, J. Shinar, Y.W. Ding and T.J. Barton, *Synth. Met.* **55-57**, 1 (1993).

99. A.V. Smith, Ph.D. Thesis, Iowa State University, Ames, IA (1994).

100. J. H. Burroughes, D. D. C. Bradley, A. R. Brown, R. N. Marks, K. MacKay, R. H. Friend, P. L. Burn, and A. B. Holmes, *Nature* **347**, 539 (1990).

101. C. Weder and M. S. Wrighton, *Macromolecules* **29**, 5157 (1996).

102. L. S. Swanson, F. Lu, J. Shinar, Y. W. Ding, and T. J. Barton, in *Electroluminescence: New Materials for Devices and Displays*, edited by E. M. Conwell, M. Stolka, and M. R. Miller, SPIE Conf. Proc., **1910**, 101 (1993).

103. L. S. Swanson, P. A. Lane, J. Shinar, and F. Wudl, *Phys. Rev. B* **44**, 10617 (1991).

104. J. Shinar, L. S. Swanson, and K. Yoshino, *Syn. Met.* **41-43**, 555 (1991).

105. E. M. Conwell, J. Perlstein, and S. Shaik, *Phys. Rev. B* **54**, R2308 (1996).

106. The PPV was provided by Fred Wudl (1990).

107. The Cambridge-PPV was provided by Neil Greenham, Cambridge University (1993).

108. D.-K. Fu, B. Xu, M. J. Marsella, and T. M. Swager, *Polym. Prepr.* **36**, 585 (1995).